University of Plymouth

PEARL **https://pearl.plymouth.ac.uk**

04 University of Plymouth Research Theses 01 Research Theses Main Collection

2011

Pyramidal Cell Diversity in the Rat Prefrontal Cortex: Electrophysiology, Dopamine Modulation and Morphology

Bartsch, Ullrich

http://hdl.handle.net/10026.1/555

http://dx.doi.org/10.24382/4291
University of Plymouth

All content in PEARL is protected by copyright law. Author manuscripts are made available in accordance with publisher policies. Please cite only the published version using the details provided on the item record or document. In the absence of an open licence (e.g. Creative Commons), permissions for further reuse of content should be sought from the publisher or author.

Pyramidal Cell Diversity in the Rat Prefrontal Cortex: Electrophysiology, Dopamine Modulation and Morphology

Barisch, U.

PhD

2011

This copy of the thesis has been supplied on condition that anyone who consults it is understood to recognize that its copyright rests with its author and that no quotation from the thesis and no information derived from it may be published without the author's prior consent.

Pyramidal Cell Diversity in the Rat Prefrontal Cortex: Electrophysiology, Dopamine Modulation and Morphology

Ullrich Bartsch

Centre for Theoretical and Computational Neuroscience

University of Plymouth

A thesis submitted to the University of Plymouth in partial fulfilment of the requirements for the degree of

Doctor of Philosophy

February 2010

Pyramidal Cell Diversity in the Rat Prefrontal Cortex: Electrophysiology, Dopamine Modulation and Morphology

by

Ullrich Bartsch

Abstract

The prefrontal cortex (PFC) is critically involved in many higher cognitive functions such as goal-directed behaviour, affective behaviour and especially working memory. *In vivo* extracellular recordings of PFC neural activity during working memory tasks show high variety in observed spiking patterns. These complex dynamics are critically shaped by intrinsic, synaptic and structural parameters of respective prefrontal networks. Moreover, dopamine (DA) is crucial for correct functioning of the PFC during working memory tasks. DA modulates a number of synaptic and intrinsic biophysical properties of single neurons, in particular deep layer pyramidal cells, which represent the major output neurons of the PFC. Despite a high variability of cortical pyramidal cell firing patterns, and somatodendritic morphology, no study has yet systematically examined correlations between intrinsic properties, morphological features and dopaminergic modulation of intrinsic properties.

This study investigated properties of deep layer pyramidal cells through whole cell patch clamp in acute brain slices of the adult rat PFC. Cells were characterised physiologically through a variety of stimulation protocols surveying different time scales and wide intensity ranges, while all fast synaptic transmission was blocked. Furthermore the same catalogue of stimuli was recorded whilst applying specific DA receptor agonists to elucidate effects of DA receptor activation on intrinsic properties. All recorded cells were injected with biocytin and dendritic morphology was reconstructed from confocal image stacks of fluorescently labelled neurons. From the resulting data a set of characteristic variables were defined and a combination of principal components analysis and hierarchical cluster analysis was used to identify similarity between recorded cells in different parameter spaces spanned by intrinsic properties, intrinsic properties under dopaminergic modulation and morphology, respectively. The analysis presents evidence for distinct subpopulations within prefrontal deep layer pyramidal cells, as seen by clustering of recorded cells in these high dimensional parameter spaces. These subpopulations also show distinct input-output relationships, bearing implications for computational functions of these subpopulations. Furthermore, this study presents for the first time evidence of subpopulation specific DA effects in deep layer pyramidal cells. The quantitative analysis of somatodendritic morphology confirms physiological subpopulations and identifies characteristic morphological features of deep layer pyramidal cells. Moreover, cluster observed in different parameter spaces overlap, leading to a definition of subpopulations that concurs with previously described prefrontal pyramidal cell types. In conclusion, the results presented provide some deeper insight into fundamental principles of information processing in prefrontal pyramidal cells under the influence of dopamine.

Contents

1 INTRODUCTION 12

2 PREFRONTAL CORTEX 15

2.1 Human and Primate Prefrontal Cortex 15

2.2 The rat PFC as a model of the primate PFC 20

2.3 Neural correlates of prefrontal cortex function 23

2.4 Deep layer pyramidal cells the rat PFC 24

2.5 Dopamine actions in the PFC 28

2.6 Motivation and aims of this thesis 32

3 METHODS AND MATERIALS 34

3.1 The whole cell patch clamp method 34

3.2 Stimulation Protocols and Analysis of Electrophysiology Data 38

3.3 Biocytin tracing, confocal imaging and an reconstruction of neural morphologies 44

3.4 Morphometric Analysis 47

3.5 Statistical analysis methods 52

4 RESULTS 57

4.1 Classifying prefrontal pyramidal cells based on intrinsic properties 58

4.2 Dopaminergic modulation of biophysical properties of deep layer pyramidal cells 73

4.3 Morphometric Analysis 95

4.4 Pyramidal cells in a combined feature space 106

5 FINAL DISCUSSION AND OUTLOOK 111

List of Figures

Figure 2.1 | Digital reconstruction of Phineas Gage' lesion 16
Figure 2.2 | The human and primate PFC 18
Figure 2.3 | Prefrontal regions in the rat 21
Figure 2.4 | Prefrontal deep layer pyramidal cell 26
Figure 2.5 | Mesocortical DA projections in the rat brain 29
Figure 2.6 | Time dependent and reversible DA receptor specific effects on GABA IPSP's. 31
Figure 2.7 | Summary of DA effects 31
Figure 3.1 | Patch clamp of prefrontal pyramidal cells 37
Figure 3.2 | Estimating the membrane time constant 40
Figure 3.3 | Estimating the input resistance 40
Figure 3.4 | Voltage clamp step stimulation 41
Figure 3.5 | Current clamp ramp stimulation 41
Figure 3.6 | Long current step stimulation 42
Figure 3.7 | Light pathways in a confocal microscope 45
Figure 3.8 | Maximum intensity projection of an example confocal image stack. 46
Figure 3.9 | Dendritic tree analysis 49
Figure 3.10 | Manual hull analysis of somatodendritic morphology 49
Figure 3.11 | Comparison of data preparation for cluster analysis 55
Figure 4.1 | Cluster analysis of electrophysiology variables from control condition 59
Figure 4.2 | Firing patterns grouped into cluster 60
Figure 4.3 | Summary of PCA results 61
Figure 4.4 | Leave-one-out analysis 63
Figure 4.5 | Raw membrane voltage traces for an example RS cell (ID#1). 64
Figure 4.6 | Raw membrane voltage traces for an example IB cell (ID#15). 65
Figure 4.7 | Raw membrane voltage traces for an example IM cell (ID#21). 66
Figure 4.8 | Average input-output functions for each cluster 67
Figure 4.9 | Average square root fit for each cluster 68
Figure 4.10 | Summary of overall DA agonist effects 75
Figure 4.11 | Inhomogeneous effects of dopamine receptor stimulation 76
Figure 4.12 | Summary of cluster analysis including dopaminergic conditions 79
Figure 4.13 | Cluster overlap of control and DA cluster 80
Figure 4.14 | PCA results by DA cluster solution 81
Figure 4.15 | Summary of main significant DA agonist effects. 82
Figure 4.16 | Influence of dopaminergic agonist on voltage clamp I-V curves 85

Figure 4.17 | Influence of dopaminergic agonists on ramp evoked f-I curves. 85
Figure 4.18 | Influence of dopaminergic agonists on transient and steady state f-I curve..... 86
Figure.19 | Influence of dopamine agonists of averaged square root 1/ISI functions. 87
Figure 4.20 | DA influence on ISI histograms 88
Figure 4.21 | D1 agonist application in bursting pyramidal cells 93
Figure 4.22 | Cluster analysis of morphometric variables 96
Figure 4.23 | Summary of pre-cluster PCA 97
Figure 4.24 | Morphologies of recorded neurons grouped by clustering results. 99
Figure 4.25 | Example morphologies from the established morphological cluster..... 100
Figure 4.26 | HCA of principal components from physiology and morphology 106
Figure 4.27 | Comparison of all cluster solutions 107

Permission to republish copyrighted material has been obtained for all reprinted figures.

List of Tables

Table 3.1 | Stimulation protocols 39
Table 3.2 | Characteristic physiological variables 43
Table 3.3 | Morphometric variables 51
Table 4.1 | Mean cluster properties 62
Table 4.2 | Mean effects of dopamine receptor agonists. 74
Table 4.3 | DA effects in control cluster 77
Table 4.4 | Mean values of DA cluster. 84
Table 4.5 | Mean values of morphology cluster 102
Table 4.6 | Selected ANOVAs of EM cluster 108

Acknowledgements

I would like to thank all people that provided help in one form or another to guide me along the lengthy and certainly not straightforward path that led to this thesis.

I would like to thank Thomas Gabriel for introducing me to the art of whole cell patch clamp recording, providing some preliminary recordings mentioned in this thesis, and many hours of wonderful Skype conversations about dopamine and other things.

Many thanks also to my supervisor Daniel Durstewitz, who sparked the fascination for Dopamine and working memory, a long time ago when I was still an undergraduate in biochemistry. Thanks to him, I have dealt with a variety of fascinating topics ranging from non-linear dynamics in intracellular signalling to *in vitro* electrophysiology. Not all efforts were blessed with success, but they have provided me with a tool set that most certainly will help me to succeed in a career in academia.

I am also most grateful to Thomas Wennekers, my second supervisor, who never forgot about me, and kept on reminding me to fulfil my duties.

Furthermore, I would like to thank Roddy Williamson for agreeing on a Faculty of Science studentship when funding was scarce, Colin Brownlee for letting me use the excellent confocal microscope at the MBA, and also Debbie Petherick for helping through administrative problems.

Also, I would like to thank my current employer Matt Jones at the University of Bristol for allowing me to spend many possible working hours on completing this thesis.

This thesis is dedicated to my mother Ursula, my father Karl-Heinz, my sister Karola and my brother Michael.

Author's declaration

At no time during the registration for the degree of Doctor of Philosophy has the author been registered for any other University award.

This study was financed with the aid of a studentship from EPSRC, a studentship from the Faculty of Science and full time employment as research assistant in the Centre for Theoretical and Computational Neuroscience.

Scientific seminars and journal clubs were regularly attended at which work was often presented. Some preliminary work on network simulation was presented at a conference, but is not reported in this thesis, since no conclusive results have been obtained.

Posters and conference presentations:

Bartsch U, Durstewitz D (2006) Dopamine modulates slow frequency oscillations and coherence in a prefrontal cortex network model. FENS Abstracts p. A116.

Kyle R, Bartsch U, Willshaw D, Durstewitz D (2009) Dopamine D1/D2 modulation of synaptic plasticity in the prefrontal cortex. BMC Neuroscience p. P193.

Word count for the main body of this thesis: ~42.000

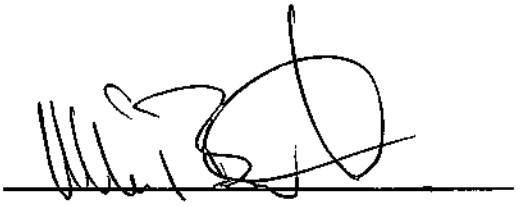

23/08/11

dimidium facti qui coepit habet: sapere aude

("He who has begun is half done: dare to know!")

Horace

1 Introduction

The prefrontal cortex (PFC) is crucially involved in many higher cognitive functions such as planning, goal-directed behaviour, and working memory (Goldman-Rakic, 1995; Miller et al., 2002; Fuster, 2008). Goal-directed behaviour and working memory involves integrating multimodal perceptual information, short term memorizing and evaluation of integrated information for initiating appropriate behaviour. The PFC has to process several streams of complex information on different time scales, in a parallel, flexible and reversible manner. In contrast, to simple short term storage, information has to be evaluated and manipulated according to the current behavioural situation; hence it has been described as "working with memory" (Winocur, 1992; Seamans and Yang, 2004).

Critically involved in optimal function of prefrontal networks during working memory tasks is the neurotransmitter dopamine (DA), (Goldman-Rakic et al., 2000; Durstewitz et al., 2000b). Despite a long interest in DA and its effect on working memory processes, the actions of DA in the PFC are not fully understood. DA has been shown to have complex time and activity dependent effects, varying for cell type or even specific synapses (Seamans and Yang, 2004).

Recent studies highlight substantial heterogeneity amongst cortical neurons (Markram et al., 2004; Bernard et al., 2009). This has been extensively studied in the case of cortical inhibitory interneurons (Ascoli et al., 2008), but the existence of functionally distinct subpopulations within excitatory pyramidal cells has only recently begun to be addressed. In fact, much debate has been dedicated to whether pyramidal cells can be divided into subpopulations at all (Steriade, 2004). From a theoretical point of view, different cell types would arise from individual cells that are clustered in a multidimensional parameter space spanned by intrinsic, synaptic and morphological properties. As opposed to a clear separation of cluster, one could also envisage a continuous sampling of the parameter space by individual cells. Cells would not form distinct clusters and individual cell parameter would vary randomly.

This thesis will shed some light on the intricate biophysical mechanisms that lay foundation for neural correlates of prefrontal function. This will be achieved through careful quantification of intrinsic properties (with particular emphasis on the impact of DA modulation), and morphological properties of prefrontal pyramidal cells. Intrinsic biophysical properties of pyramidal cells will be characterised through stimuli on multiple time scales and wide intensity ranges. The impact of DA will be examined through the same catalogue of stimuli while applying selective DA receptor agonists. Morphology of pyramidal cells will be assessed

through confocal imaging and 3-dimensional reconstruction of the dendritic tree and subsequent quantitative morphometric analysis of somato-dendritic properties.

In each resulting dataset similarity between individual cells will be identified through a combination of two multivariate analysis techniques, principal component analysis (PCA) and hierarchical cluster analysis (HCA). This will allow an unbiased view on how pyramidal cells populate the multidimensional parameter space spanned by either intrinsic properties, intrinsic properties under dopaminergic modulation or somatodendritic morphology.

It will be demonstrated that pyramidal cells do form distinct, sometimes overlapping groups in all of these parameter spaces. I will argue that at least two distinct groups of pyramidal cells exist, which differ in basic intrinsic properties, dopaminergic modulation of these intrinsic properties and in quantitative measures of somatodendritic morphology, although heterogeneity within groups exists.

To this end the thesis presents a systematic and quantitative approach to classifying pyramidal cells based upon biophysical and morphological criteria and is structured as follows.

Chapter 2 gives a brief review of the PFC. I will describe the anatomy in primates and rats and will particularly address the issue of homologous regions between primates and rodents. Then I will describe its role in cognition and behaviour and present some evidence for neural correlates of behaviour shown to be dependent on the PFC. Then I will review cytoarchitectural features that differentiate the PFC from sensory cortices. I will arrive at the single cell level where I will focus on biophysical properties of deep layer pyramidal cells which are the major projection neurons of the PFC and constitute the main subject of this thesis. Moreover, I will present recent evidence for the crucial role of DA in optimal function of prefrontal cortices during working memory and goal-directed behaviour and will describe in more detail how DA affects biophysical properties of deep layer pyramidal cells. Eventually, I will formulate some key questions for this thesis, and describe how these questions are addressed in this thesis.

Chapter 3 introduces all experimental and analysis methods used in this thesis. I will briefly review the whole cell patch clamp method, which is used to obtain single cell recordings in acute slices from the prefrontal cortex of adult rats. Furthermore, I will describe the stimulation protocols designed to probe biophysical properties of pyramidal cells and in particular explain how key variables were extracted to capture responses of neurons to the diverse stimulation protocols. I will briefly introduce confocal imaging and how it can be applied to reconstructing neuronal morphologies. Then I will present how a reconstructed morphology is subjected to quantitative analysis of morphological features.

Chapter 4 describes the experimental results obtained. This chapter will be divided into four sections. In the first section I will present the results of PCA and HCA for biophysical properties measured while all fast synaptic transmission was blocked in the slice preparation. Established groups and their properties will be described and briefly discussed in the light of previous findings. In the second section, I will describe effects of applied dopamine receptor agonists on intrinsic properties. These effects will be described based on the groups established in the previous section. Based on observed heterogeneous DA effects in the previously established groups, an extended PCA/HCA analysis will be presented where dopamine agonist modulated variables are included. The results obtained indicate possible groups of cells that show distinct DA modulation. This will be comapred to previous studies on dopaminergic regulation of intrinsic properties. In the third section I present the PCA/HCA analysis for quantitative analysis of neuronal morphology, and briefly discuss the results. In the last section I will present a HCA analysis based on the principal components from both electrophysiology and morphology, and will compare these results to the cluster solutions obtained in the previous sections.

Chapter 5 will present a synopsis and wider discussion of the results obtained from the different analyses. I discuss methodological aspects and caveats of the presented analysis and compare it with other approaches and current research in the field. I will also describe the wider impact of the obtained results in reference to computational properties of single cells and networks in the PFC. Finally, I will give an outlook for future work based on the obtained results.

2 Prefrontal Cortex

2.1 Human and Primate Prefrontal Cortex

The term prefrontal cortex (PFC) was introduced at the turn of the 19th century by neuropathologists and anatomists to describe a collection of brain areas in the frontal lobe of humans and primates. One of the first documented case studies illustrating the essential function of the prefrontal areas in cognition and behaviour is the mid-nineteenth century case of Phineas Gage, a New England railroad construction worker who was accidentally struck by an iron bar whilst positioning explosive portions. The accidental explosion of one such portion propelled the iron bar through his face from below, traversing the base of his skull, and landed about 20-25 yards behind him, inflicting a massive damage on his left frontal lobe. Dr John Martyn Harlow, who arrived an hour later at the site, managed to ease the severe haemorrhage. This and his subsequent successful treatment of the infection saved Gage's life (Harlow, 1999). Gage was able to return to his parents' farm after only 3 months in hospital and had lived for over 11 years after the accident, but the damage to his frontal lobe had left him with severe psychological changes. In his description of the case Harlow explained why his company would not reemploy him (Harlow, 1999):

> *His contractors, who regarded him as the most efficient and capable foreman in their employ previous to his injury, considered the change in his mind so marked that they could not give him his place again. He is fitful, irreverent, indulging at times in the grossest profanity (which was not previously his custom), manifesting but little deference for his fellows, impatient of restraint or advice when it conflicts with his desires, at times pertinaciously obstinate, yet capricious and vacillating, devising many plans of future operation, which are no sooner arranged than they are abandoned in turn for others appearing more feasible. In this regard, his mind was radically changed, so decidedly that his friends and acquaintances said he was 'no longer Gage'.*

Although this report is merely anecdotal it illustrates a few of the most important functions that have been attributed to the prefrontal cortex since these early days of neuroscience. Later reconstruction of Gage's lesion (Damasio et al., 1994; Ratiu and Talos, 2004) revealed that mainly ventromedial areas in the PFC were affected by the iron bar passage. Figure 2.1 depicts a 3d rendering of Gage's skull including the possible trajectory of the iron bar. Based on the case

description Gage was unable to make rational decisions in the social realm and was emotionally depleted. Surprisingly abilities that seem to relate to rational thought alone, i.e. calculations, tackling abstract problems or recalling appropriate knowledge seem not to be affected (Damasio et al., 1994; Harlow, 1999).

The detailed neuropsychological characterisation of various frontal patients since then has led to distinction of frontal syndromes based on affected areas. Lesions confined to the three major prefrontal regions orbital, medial and lateral, result in different psycho-cognitive changes (Fuster, 2008): The orbital syndrome mainly includes changes in the control of affect, such as impulsivity, instinctual disinhibition, euphoria, and lack of moral restraint but also hypermotility, perseveration and distractibility (very much like the case of Phineas Gage). The medial/anterior cingulate syndrome is mainly distinguished by lack of initiative and spontaneity, hypokinesia or akinesia, and apathy. Also, commonly impaired is the monitoring and correction of errors. A lateral syndrome includes deficits in focusing and sustaining attention, a general lack of initiative and decision-making, inability to make plans and to execute them, poor performance in working memory tasks, and low verbal fluency. This is commonly accompanied by disorders of affect such as apathy and depression.

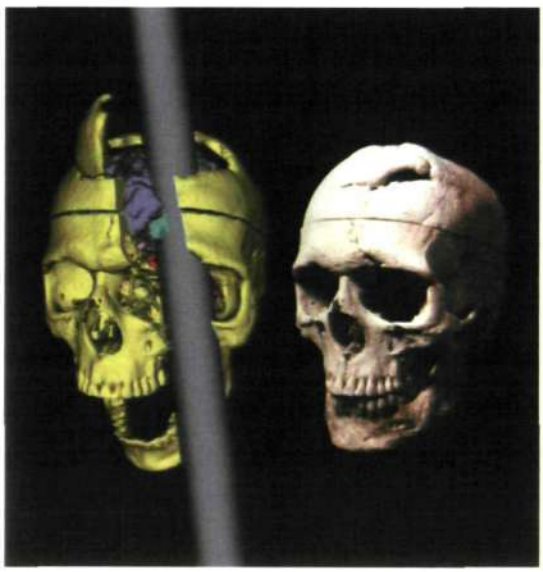

Figure 2.1 | Digital reconstruction of Phineas Gage' lesion
A three-dimensional computer reconstruction of Phineas Gage's skull generated from thin-slice computed tomographic images. A reconstruction of a normal human brain generated by magnetic resonance imaging was registered within the skull using a non-affine algorithm (Ratiu and Talos, 2004). This reconstruction shows that the iron bar most likely affected ventromedial areas of the PFC (Damasio et al., 1994).

Based on these results from human neuropsychology and primate electrophysiology different authors have conceptualised theories of prefrontal function, mainly differentiating between orbitofrontal (equivalent to ventromedial) (OF-PFC) and dorsolateral networks (DL-PFC). Many authors have emphasised the involvement of OF-PFC in integrating emotional and motivational state information with current cognitive task demands (Damasio, 1994; Damasio et al., 1996; Rolls, 2000, 2005; Wallis, 2007) which concurs with strong projections to the

amygdala and basal ganglia from OF-PFC (Cardinal et al., 2002). Thus orbitofrontal networks have been regarded as a rapidly flexible associative-learning area encoding associations between sensory cues and behavioural outcomes, in particular reward (Rolls 1996, 2008). More recent research indicates that OF-PFC might instead encode general outcome expectancies (Tremblay and Schultz, 1999; Wallis, 2007; Burke et al., 2008; Mainen and Kepecs, 2009).

The DL-PFC has been mainly associated with executive functions such as sensory working memory, attention, response selection and top down control of information in order to generate plans and strategies for goal-directed behaviour (Goldman-Rakic, 1995; Miller and Cohen, 2001; Fuster, 2001; Duncan, 2001). The DL-PFC has reciprocal connections with higher order sensory cortices (visual, auditory and somatosensory) and in turn sends strong projections to premotor and motor cortices (Bates and Goldman-Rakic, 1993; Lu et al., 1994). This enables the DL-PFC to bias sensory processing in favour of selected motor programs (Miller and Cohen, 2001). One key function of the DL-PFC is to initiate appropriate behaviour in a given context and the active maintenance of task relevant information, i.e. working memory (Fuster, 1973; Niki, 1974b; Goldman-Rakic, 1995).

These distinct functions of prefrontal areas are reflected in their anatomical connections to other cortices and subcortical regions. Anatomically the PFC of humans and primates has been defined as all cortical areas rostral to the premotor cortex up to the frontal pole, while its lateral boundary is marked by the inferior precentral fissure. Figure 2.2 shows a comparative labelling of human and macaque prefrontal areas from Petrides & Pandya (2002b). Within the frontal lobes of the human brain, the PFC itself can be divided into 3 parts using Brodmann's cytoarchitectonic areas. A medial or paralimbic part roughly consisting of areas 10-14, an orbital part comprising areas 11, 12, 47 and a lateral part which is further divided into dorsolateral and ventrolateral comprising areas 8-10 and 44-46, respectively. This partition into three subfields is also found in the brain of non-human primates where a dorsolateral area comprising Walker's areas 8-10, 45, 46 (Walker, 1940) and an orbitofrontal/ventromedial (Walker's areas 11-14) region are distinguished. Generally, there is now wide agreement on the homology between human and non-human primate frontal cortices (Uylings and van Eden, 1990; Barbas, 2000; Petrides and Pandya, 2002b).

In the past the PFC was defined as the principal projection area of the mediodorsal thalamic nucleus (MD) and forms strong reciprocal connections with it (Rose and Woolsey, 1948; Akert, 1964). Several other cortical areas receive fibres from this structure, but exclusively the prefrontal cortex sends afferents to it. The MD relays information from subcortical regions such as the mesencephalon, the amygdala, the substantia nigra, the prepiriform cortex, and the inferior temporal cortex to the prefrontal cortex via the pars magnocellularis of the MD (Ray and Price, 1993). The thalamic projections differ for the different prefrontal regions. The

magnocellular part of the MD projects mainly to the orbital and medial parts of the PFC and the parvocellular part projects mainly to the cortex of the lateral parts of the PFC (Akert, 1964; Goldman-Rakic and Porrino, 1985; Barbas et al., 1991).

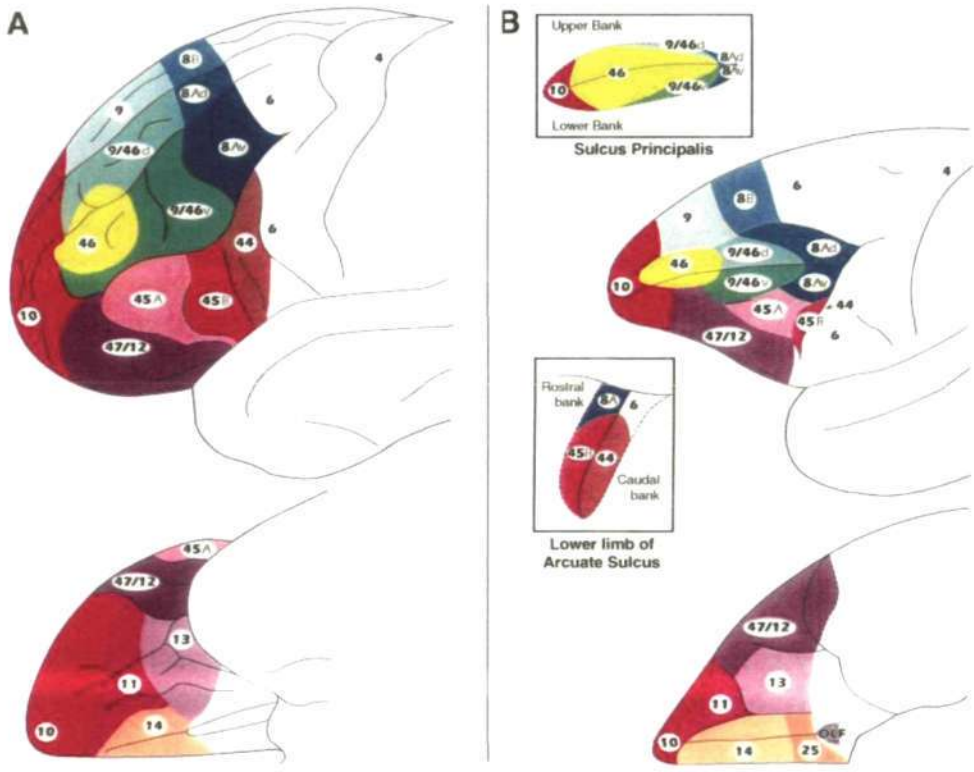

Figure 2.2 | The human and primate PFC
Comparative anatomical subdivisions of the PFC in human (A) and macaque (B) brain. The respective top image shows the lateral surface, whereas the respective bottom image shows the medial surface of the PFC. Homologous regions have similar the same colour shading. Brodman's (A) and Walker's areas (B) are labelled, respectively. Insets in B show magnification of the sulcus principalis and the lower limb of the arcuate sulcus.
From (Petrides and Pandya, 2002b).

Several other thalamic projections reach the prefrontal cortex, originating in the intralaminar and midline nuclei, the anterior medial nucleus and the rostral parts of the ventral complex (Groenewegen and Berendse, 1994; Barbas and Ghashghaei, 2002; Groenewegen and Witter, 2004). Furthermore, direct afferents ascending from the ventral tegmental area, tegmentum, hypothalamus and amygdala exist (Krettek and Price, 1974; Kievit and Kuypers, 1975; Divac et al., 1978).

The different prefrontal regions (dorsolateral, medial, and orbital) also receive diverse, sometimes overlapping, projections from all higher sensory cortices. An early account for systematic discussion of prefrontal cortico-cortico networks comes from Jones and Powell (1970). They observed a general pattern in how sensory input is relayed to the PFC. For example the primary visual cortex (V1) not only sends afferents to V2 and other higher visual areas, but also to prefrontal area 8A, which itself sends recurrent projections back to V1. This

pattern of recurrent connections can be observed at each step within the hierarchical processing of visual information, (i.e. V1 has recurrent connections with 8A, area 20 with 8A+, and temporal cortices with 46). This pattern of recurrent connectivity of sensory cortices with the PFC at every processing step also applies to auditory and somatosensory cortices (Jones and Powell, 1970; Fuster, 2008). Later studies have examined projections of sensory association areas to prefrontal areas in more detail (Petrides and Pandya, 2002b). There are 4 major cortical areas projecting to the PFC: the posterior parietal cortex projects to all areas of the PFC via the superior longitudinal fasciculus and the occipitofrontal fasciculus. The inferotemporal cortex sends projections mainly to orbital areas via the uncinate fasciculus, whereas the superior temporal cortex sends 3 different fibre bundles (arcuate fasciculus, extreme capsula uncinate fasciculus) originating from different subdivisions of the superior temporal cortex (Petrides and Pandya, 2002a; Fuster, 2008). Within a given fascicule one can observe a remarkable topological organisation of higher sensory inputs to the PFC. For example the higher visual area 7 sensory fields seem to be preserved in their projections to the respective frontal areas (Cavada and Goldman-Rakic, 1989). Despite this independence of incoming projections of higher sensory areas, many bimodal or trimodal association areas have been identified, for example in the sulcus principalis, but also in ventral and medial areas of the PFC (Jones and Powell, 1970; Chavis and Pandya, 1976; Fuster, 2008).

On the whole, two major functional prefrontal networks can be distinguished based on incoming afferents (Fuster, 2008). The lateral PFC receives mainly visual, auditory and somatic inputs, whereas the orbital PFC predominantly processes olfactory, gustatory and some auditory inputs. Fuster (2008) assumes a functional segregation of these networks, relating the lateral PFC to the organisation of sequential motor planning and the orbital PFC (which also receives major efferents from amygdala and basal ganglia) to the integration of sensory and motivational aspects of behaviour.

Most of the structures that send efferents to prefrontal areas do receive reciprocal efferents from their prefrontal target areas. The main projection area of the PFC is the mediodorsal nucleus of the thalamus (Akert, 1964; Groenewegen and Witter, 2004). The PFC also sends strong projections to the hypothalamus, the ventromedial caudate nucleus, and the amygdala via its orbital portions. The dorsolateral PFC projects to the lateral thalamus, the dorsal caudate nucleus, and to other cortical areas (Goldman-Rakic, 1988; Fuster, 2008). The mesencephalon, pons, subthalamus, hypothalamus, and septum are further subcortical structures innervated by prefrontal fibres (Smith and DeVito, 1984; Goldman-Rakic, 1988).

One notable exception to the theme of reciprocal connections between the PFC and target structures is the basal ganglia. For example, both in rats and humans the prefrontal cortex sends efferents to the caudate nucleus and the anterior putamen (Ongur and Price, 2000; Uylings et al.,

2003) without receiving direct afferents. Feedback from these target structures could reach the PFC through the substantia nigra, which receives projections from caudate and putamen, or via the ventral anterior and the mediodorsal thalamic nuclei (Middleton and Strick, 2000; Ongur and Price, 2000).

2.2 The rat PFC as a model of the primate PFC

According to a current standard rat brain atlas (Paxinos and Watson, 2007) prefrontal cortices in the rat can be divided into four areas (Figure 2.3 A): infralimbic (IL), prelimbic (PL), dorsal and ventral anterior cingulate (ACd, ACv) and medial precentral areas (PrCm or Fr2). Other authors have used different labels (Zilles, 1985), but agree on the general map of prefrontal subdivisions (Ongur and Price, 2000). Figure 2.3 depicts a medial view on the left rat PFC (Uylings et al., 2003) and a sagittal view at about +3.6 mm AP (Paxinos and Watson, 2007), where different regions and labels currently used are compared.

One major difference to frontal areas in monkeys and humans, where layer IV mostly contains stellate cells and is clearly distinguishable from other layers (sometimes referred to as frontal granular cortex), is that the rat prefrontal areas lacks a distinct layer IV (i.e. it is agranular). Although Brodmann did not map the rat cortex in his original studies (Brodmann, 1909), he did map some related species (ground squirrel and rabbit), and concluded that rodents indeed lack a comparable frontal cortex because of the missing layer IV. Later Rose and Woolsey (1948) suggested identifying homologous brain regions based on connectivity to other brain regions, and proposed a prefrontal cortex in rats based on homologous strong reciprocal connection with the mediodorsal thalamic nucleus (MD). Although most researchers agree on the boundaries of the prefrontal cortex itself in rats, it is still debated if and which areas in the rat are homologous to dorsolateral and orbitofrontal areas in monkeys and humans. In partuclar, Preuss (1995) questioned whether rats would have an equivalent prefrontal cortex at all. He concluded that Fr2 and the ACd are more similar to primate premotor areas and thus should not be included in the rat prefrontal cortex (Condé et al., 1990, 1995; Preuss, 1995). In an attempt to reconcile conflicting reports, Uylings et al. (2003) suggested a range of criteria to identify homologous brain structures between species: the pattern of specific connections and their relative strength, functional properties as estimated by electrophysiological or behavioural studies, the presence of specific neurotransmitters or modulators, embryological development, and only when closely related species are compared local cytoarchitecture should be taken into account.

With respect to prefrontal connections to other brain areas, Rose and Wolsley (1948) initially regarded the MD as the defining projection for prefrontal areas. But with the advance of tracing methods, recent and more detailed studies have shown that in primates various other thalamic

nuclei (i.e. the intralaminar and midline nuclei and the anterior medial nucleus) project to prefrontal areas (Uylings et al., 2003; Groenewegen and Berendse, 1994; Barbas and Ghashghaei, 2002). Moreover, there is evidence from monkeys and other species that the MD does not exclusively project to the PFC but also sends efferents to other cortical areas such as premotor, motor, temporal and parietal cortices (Paxinos and Watson, 2007).

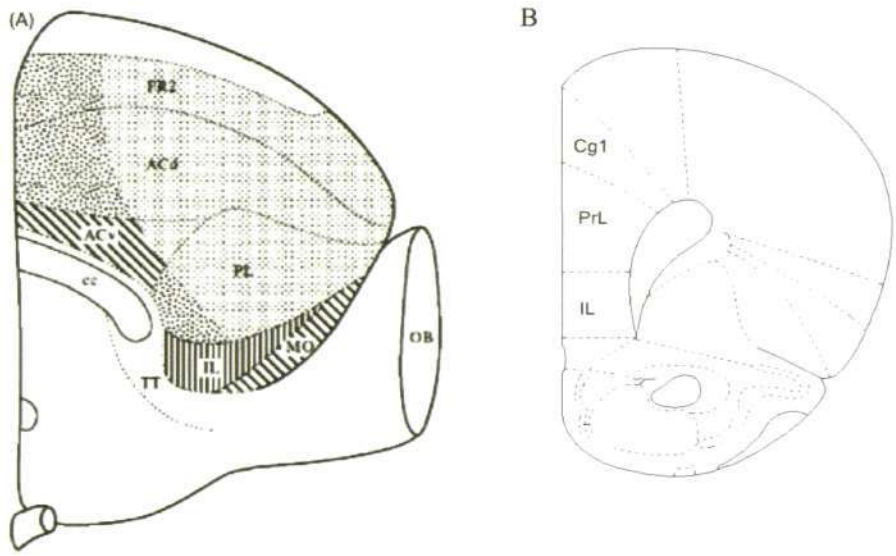

Figure 2.3 | Prefrontal regions in the rat
A) Medial view: Frontal region 2 (FR2), ventral and dorsal anterior cingulate (ACv, ACd), prelimbic (PL) and infralimbic region are the main prefrontal areas (cc: corpus callosum, MO, medial orbital, VO ventral orbital, from Uylings et al., 2003.
B) Corresponding saggital view from Paxinos and Watson, 2007: Cingulate 1 (Cg1) is identical with ACd, prelimbic (PrL) and infralimbic (IL) are identical with regions in A.

Uylings and van Eden (1990) suggested "strong reciprocity" (i.e. the number and density of projections of projections from the MD to the PFC) as improved criterion for defining homologous PFC regions. They suggested including the AC of rats and primates into the prefrontal cortex. Supporting this notion, but opposing results by Preuss et al. (Condé et al., 1990, 1995; Preuss, 1995), other groups have found extensive reciprocal connections of ACd and Fr2 to the MD (Ray and Price, 1992; Reep and Corwin, 1999; Vertes, 2002). This argues in favour of a homologous "dorsolateral" region in the rat located in the medial sections of the rat PFC (mPFC). Also, this is supported by connectivity of the rat mPFC to other cortical areas. In particular one can define three distinct cortico-prefrontal loops (Uylings et al., 2003). The prelimbic/infralimbic cortices (cytoarchitectionally less differentiated) receive projections from perirhinal and entorhinal cortex and directly from the hippocampus. A dorsal shoulder region is mainly connected to visual and retrosplenial cortices indicating some homology to the frontal eye field in monkey. And a rostral area interconnected with motor, somatosensory-motor, and somatosensory-association cortices indicating role in motor planning and execution, maybe

even colocalisation of premotor and prefrontal functions (Uylings and van Eden, 1990; Uylings et al., 2003).

There is also a strong homology of projections from subcortical and limbic areas such as the amygdala, entorhinal and perirhinal cortex and a number of cortico–basal ganglia–thalamic networks that have strong homology with monkeys (Ongur and Price, 2000; Uylings et al., 2003). Uylings et al. (2003) have described four of these 'indirect' frontal-basal ganglia-thalamic loops in rats which always involve different parts of the frontal cortex, the dorsal or ventral striatum, the pallidal and nigral complex and the ventral and medial thalamic nuclei. These loops can in some cases be modulated by inputs from amygdala or other thalamic nucleii.

Studies using *in vivo* electrophysiology show a variety of dynamic firing rate changes that can be observed in the prefrontal cortex of rats during behavioural tasks that depend on the prefrontal cortex (Jung et al., 1998; Chang et al., 2002; Baeg et al., 2003), some of which are similar to response patterns found in monkeys (Fuster, 1973; Quintana and Fuster, 1999). Seamans and colleagues have recently reviewed electrophysiological and behavioural evidence for homology between rat and primate prefrontal areas, where they concluded that the mPFC of rats is somewhat a rudimentary predecessor of the dlPFC in monkeys merging functions of anterior cingulate, dlPFC and premotor cortices in monkeys (Seamans et al., 2008).

Support for this notion also comes from a number of lesion studies (Kolb, 1984). Lesions to the medial prefrontal areas in the rat produce strikingly similar behavioural deficits to those observed in monkeys after lesion of dorsolateral and orbitofrontal regions. For example medial prefrontal lesions in rats evoke deficits in different aspects of various working memory tasks such as delayed response, delayed alternation and non-matching to sample tasks (Kolb et al., 1974; Kolb, 1984; Otto and Eichenbaum, 1992; Uylings et al., 2003).

Finally, there is a strong homology of cholinergic and monoaminergic innervation between rat PFC and primate PFC, i.e. direct projections from the PFC to cholinergic nucleii in the basal forebrain (Gaykema et al., 1991; Ghashghaei and Barbas, 2001), to serotonergic neurons in the locus coeruleus (Arnsten, 1997; Jodoj et al., 1998), and to dopaminergic neurons in the ventral tegmental area (VTA) and substantia nigra (SNr) in both rats and primates (Williams and Goldman-Rakic, 1998; Carr and Sesack, 2000).

In summary, a wide range of studies support the idea of a moderate degree of homology between rat mPFC and monkey dlPFC, and the overall usefulness of the rat PFC as a model for prefrontal function in humans (Kolb, 1984; Uylings and van Eden, 1990; Ongur and Price, 2000; Brown and Bowman, 2002; Uylings et al., 2003; Seamans et al., 2008).

2.3 Neural correlates of prefrontal cortex function

A first insight into the neural basis of working memory came from *in vivo* recordings in monkeys (Fuster, 1973, 2008; Niki, 1974a; Funahashi et al., 1989). Neurons in the prefrontal cortex can enter a persistent high activity state correlated with active working memory. In their studies monkeys were trained to perform a delayed matching to sample task and single cell activity in the PFC was recorded at the same time. During the task monkeys were shown two dots, red and green, where they had to remember the location of the red dot for a period of a few seconds until they received a go signal to indicate position of the red dot with a saccade. Correct choices were rewarded with juice or water. During the waiting time or delay time the dots were not shown so that the monkey had to keep an active memory of the location of the red dot over time. It was shown that some stimulus-property selective cells in the PFC showed a constant elevation in firing rate only during delay period - that is while the stimuli are not visible to the monkey. This persistent activity is believed to be a neuronal correlate of working memory (Goldman-Rakic, 1995), an active short term encoding of stimulus properties needed for obtaining future reward.

Attempts to understand the underlying mechanisms of persistent activity have been made mainly through models based on an attractor framework rooted in dynamical systems theory (Strogatz, 2001). Attractor network models show one, two or many stable activity states (fixed points), where firing rate is relatively insensitive to perturbations. The achieved fixed point depends on immediate input history, thereby forming memory of previous inputs (Hopfield, 1995). Persistent activity has been found in different preparations and brain areas (Major and Tank, 2004), suggesting it is a universal mechanism for short term storage and manipulation of information. Different models of how attractor states could arise especially in prefrontal networks have been developed (Amit and Brunel, 1995; Wang, 1999; Compte et al., 2000; Brunel and Wang, 2001; Durstewitz and Seamans, 2002, 2006; Compte, 2006). But discrete attractor dynamics for working memory have been challenged by recent experimental data (Komura et al., 2001; Brody et al., 2003; Ikegaya et al., 2004; Jones and Wilson, 2005) which indicates that distinct temporal dynamics might be important for working memory function (Durstewitz and Seamans, 2006).

Although mean firing rates can be stable across delay periods, PFC neurons show highly irregular firing patterns within persistent activity states (Compte et al., 2003). Different models suggest this irregularity might arise either from stochastic (Shadlen and Newsome, 1994, 1998) or deterministic mechanisms (Softky and Koch, 1993; vanVreeswijk and Sompolinsky, 1996; Durstewitz and Gabriel, 2007). A deterministic (near chaotic) mechanism might facilitate processing of temporal information (Bertschinger and Natschläger, 2004; Durstewitz and

Gabriel, 2007) but further experiments are needed to pinpoint biophysical mechanisms of temporally irregular activity.

Apart from high variability of firing rate patterns during delay period activity, temporal variations in overall delay period activity have been observed. For instance in single neurons a slowly rising firing rate, also known as climbing activity, has been observed during working memory tasks (Komura et al., 2001; Brody et al., 2003; Reutimann et al., 2004). Climbing activity slowly rises during delay period to reach its maximum firing rate at the end of the delay period where it abruptly ends. Interestingly this climbing activity can be adjusted to varying delay period lengths quickly and is therefore suggested to be a neural correlate for internal timing of behaviour (Leon and Shadlen, 2003; Durstewitz, 2003).

Furthermore, average population activity (local field potential) displays oscillations in theta and gamma frequency range during working memory (Pesaran et al., 2002; Lee et al., 2005; Raghavachari et al., 2005; Jones and Wilson, 2005) and phase locking of individual prefrontal units to theta rhythm in the hippocampus (Siapas et al., 2005; Jones and Wilson, 2005) advocating that temporal structure on the network level might be equally important for working memory processes. A wide range of experimental and theoretical studies suggest that temporal relations between spikes and/or population activity may be used to encode information (von der Malsburg, 1981; Abeles, 1991; Mainen and Sejnowski, 1995; Hopfield, 1995; Riehle et al., 1997; Ikegaya et al., 2004; Dragoi and Buzsaki, 2006). Therefore, it seems plausible to assume that these different aspects of temporal structure in prefrontal neural activity may be functional correlates of working memory.

In summary, there is a rich repertoire of neural activity patterns related to working memory and other prefrontal functions. This emphasises the need for a detailed analysis of underlying structural and electrophysiological properties of neurons in the prefrontal cortex. In the following section, I will briefly introduce general cortical network topologies (cortical column) and point out some differences of frontal areas compared to other cortices. Finally, I will describe the principal cell types that these networks are composed of, with a focus on deep layer pyramidal cells, which were examined in this study.

2.4 Deep layer pyramidal cells the rat PFC

The basic microcytoarchitecture of the rat PFC is that of the canonical cortical column (Douglas and Martin, 2004; Thomson, 2007). Inputs from sensory cortices or associative cortices primarily arrive in the superficial layer 2/3, which in turn send local recurrent projections to neighbouring cells in layer 2/3 and to pyramidal cells deep layers 5 and 6, where they meet

arriving projections from subcortical thalamic structures (Levitt et al., 1993; Kuroda et al., 1995).

One can identify 4 major excitatory cell types: pyramidal cells in layer 6, layer 5 and layer 2/3, plus aspiny stellate cells in layer 4 of sensory cortices (the majority rat prefrontal cortex is agranular), and a large variety of inhibitory interneurons (Markram et al., 2004; Thomson, 2007). Layer 5 pyramidal cells are the major output neurons of the cortex and receive dense inputs from layer 2/3 (Thomson and Bannister, 1998; Reyes and Sakmann, 1999). They project to a variety of subcortical targets including the thalamus, the superior colliculus, pons and spinal cord, as well as to other cortical regions and to the contralateral cortex (Thomson 2007). L5 pyramidal cells have been divided into two subclasses, regular spiking (RS) and intrinsically bursting (IB) cells (Connors 1982, McCormick 1985). These different physiological cell types have also been linked to differences in morphological properties of these cells in rodent cortices, i.e. RS cells have been observed to have generally more slender non-tufted apical dendrites, whereas IB cells had thick tufted apical dendrites (Larkman and Mason, 1990; Mason and Larkman, 1990; Kasper et al., 1994). These firing patterns can be explained by a different composition of intrinsic biophysical properties, in particular the occurrence of dendritic calcium spikes has been linked with burst generation (Rhodes and Gray, 1994).

It is important to point out though that differences in microcircuitry and cellular complexity between prefrontal and other cortices are increasingly recognised (Elston, 2003a). For example, there are strongly clustered lateral projection of pyramidal cells in layer 2/3 in prefrontal areas of the monkey and the rat (Isseroff et al., 1984; Kritzer and Goldman-Rakic, 1995; Pucak et al., 1996). These connections show as characteristic stripes after injection of retrograde tracer into superficial layers (Levitt et al., 1993; Pucak et al., 1996). This stripe-like organisation is distinctly different to patchy lateral connections found in visual cortex (Gilbert and Wiesel, 1989; Kritzer and Goldman-Rakic, 1995), and might add to the increased robustness of persistent activity in prefrontal areas as opposed to other in cortices (Goldman-Rakic, 1995; Lewis et al., 2002).

Differences in deep layer pyramidal cell properties in the PFC have also been reported. In a slice preparation of the rat prefrontal cortex Yang et al. (1996) distinguished 4 different deep layer pyramidal cell types the classic RS and IB types plus an intermediate type (IM) and a rhythmic oscillatory bursting cell type (ROB), based on firing patters and other intrinsic properties. They stated that IB cells are the major cell type of the PFC (65%), as opposed to sensory areas where bursting cells constitute only a small fraction of overall pyramidal cells. In a later study Degenetais et al. (2002) recorded prefrontal pyramidal cells *in vivo* in anaesthetised rats and found similar cell types, but adopted a slightly different terminology.

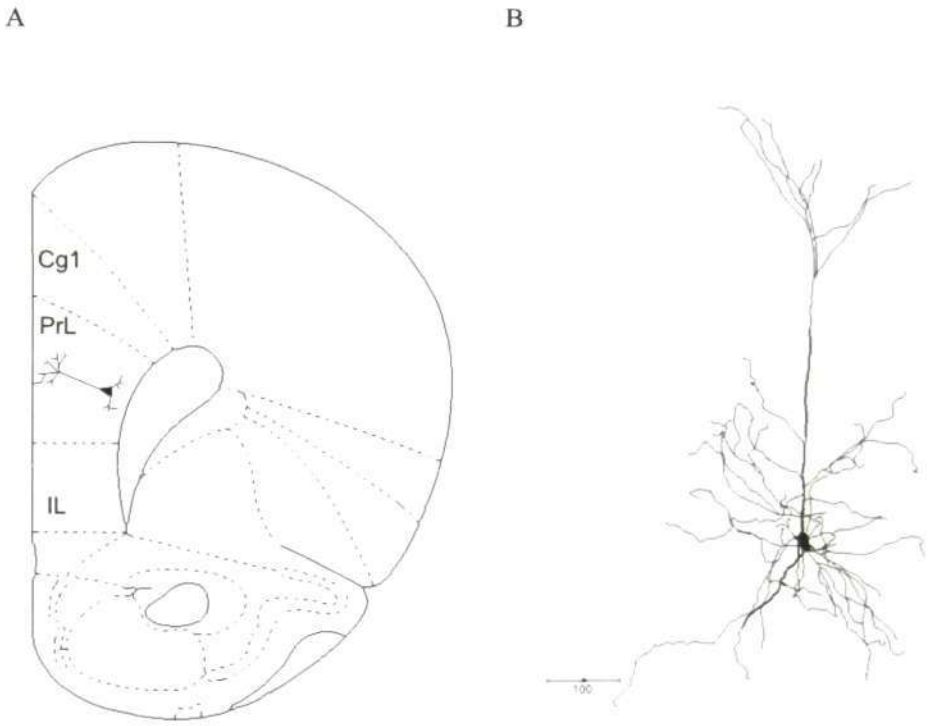

Figure 2.4 | Prefrontal deep layer pyramidal cell
A) Schematic view of a saggital slice of rat prefrontal cortex including an illustration for the approximate position of the cell depicted in B.
B) Example of a typical prefrontal pyramidal cell. Digitally reconstructed after staining with a fluorescent marker (see Methods section). Scale bar equals 100 μm.

An intriguing study on prefrontal pyramidal cells in ferrets found a distinct correlation between dendritic morphology of deep layer pyramidal cells and synaptic coupling and plasticity (Wang et al., 2006). They described a morphological phenotype with an early diverging apical dendrite (complex pyramidal cells), that is connected to other complex pyramidal cells through mainly facilitating synapses; thus gives rise to a hyper-reciprocal network of pyramidal cells in the PFC.

The apparent use of different 'cell type' definitions highlights the quintessential problem of cell classification within the neocortex. Previous studies have established various electrophysiological classes of neurons in the neocortex (Llinas, 1988; Connors and Gutnick, 1990; Häusser et al., 2000; Nowak et al., 2003; Steriade, 2004), but unambiguous classification of cells is required to ease comparison of results from different laboratories. A common framework for classification of pyramidal cells has not been established yet. In the case of GABAergic interneurons, which seem much more diverse than pyramidal cells (Markram et al., 2004), a recent initiative proposed the Petilla framework in an attempt to unify classification

schemes for neocortical interneurons (Ascoli et al., 2008). This approach attempts to establish distinct parameter from physiology, morphology, connectivity and molecular properties to unequivocally determine cell classes. Only through the rigorous analysis of correlations between these different aspects of neuronal function, can one establish meaningful neuronal classes and thus, disentangle the role of single neuron properties in neuronal network dynamics.

Recent efforts increasingly focus on correlating neuron classes established in different parameter spaces (e.g. physiology v morphology). For example Dumitriu et al. (2007) recently revealed correlation between dendritic morphology and synaptic plasticity in interneurons. In a similar fashion recent research on pyramidal cells identified functional networks of distinct cell types (Markram et al., 1997; Yoshimura et al., 2005; Song et al., 2005) which can be correlated with synaptic plasticity parameters, (Hefti and Smith, 2000; Wang et al., 2006), projection targets and/or expression of molecular markers (Molnár and Cheung, 2006; Molyneaux et al., 2007; Brown and Hestrin, 2009b; Groh et al., 2009)

These recent studies were the main inspiration for the current study and the attempt to correlate intrinsic biophysical properties of deep layer pyramidal cells with morphological parameters. The current approach differed in that I also probed biophysical properties under the influence of dopaminergic agonists, which has, to my knowledge, not been attempted in this way. The following section will describe the importance of dopamine for proper function of prefrontal networks.

2.5 Dopamine actions in the PFC

Optimal performance in working memory tasks depends critically on dopaminergic modulation of the PFC (Goldman-Rakic et al., 2000; Durstewitz and Seamans, 2002). The PFC of monkeys and rats receives major dopaminergic afferents from the ventral tegmental area (VTA, Figure 2.5) (Séguéla et al., 1988; Goldman-Rakic et al., 1989; Verney et al., 1990) and in primates DA concentration in the PFC rises at the beginning of a working memory task and stays elevated throughout many trials (Watanabe et al., 1997).

DA exerts its actions via G-protein coupled receptors that can be divided in two main receptor types: D1 type receptors (including the genotypes D_1 and D_5) coupled to G-proteins that stimulate intracellular cyclic adenosine-monophosphate (cAMP), namely G_s, G_{olf}, or G_q; and the D2 type receprotrs (including the genotypes D_2, D_3, D_4) coupled to G proteins that inhibit cAMP via $G_{i/o}$ (Neve et al., 2004). Prefrontal regions show DA-receptor immunoreactivity on both pyramidal and non-pyramidal cells (Goldman-Rakic et al., 1989; Vincent et al., 1993; Sesack et al., 1995; Santana et al., 2009). Activation of the respective receptor types may be controlled by the extracellular concentration of DA, where low concentrations primarily activate D1 receptors and high concentrations primarily activate D2 type receptors in the PFC (Trantham-Davidson et al., 2004).

The importance of intact DA signalling in the PFC for working memory has been demonstrated by *in vivo* application of dopaminergic agonists and antagonists in monkeys while they are performing working memory tasks. Effects of local injection of DAR-ligands on working memory are complex and depend on the magnitude of stimulation and timing of application relative to the ongoing task. Sawaguchi and colleagues demonstrated that DA injection enhanced delay period activity substantially (Sawaguchi et al., 1990a), which was D1 receptor dependent (Sawaguchi et al., 1990b; Sawaguchi and Goldman-Rakic, 1991). D1 receptor stimulation can improve delay period activity and behavioural performance in low concentrations, but impairs activity and performance in high concentrations (Williams and Goldman-Rakic, 1995; Arnsten, 1997; Zahrt et al., 1997; Granon et al., 2000). In conclusion the influence of D1 receptor activation on delay period activity has been described as an inverted U-shape function, where D1 receptor activation has an optimal range, but hyper or hypo-stimulation of D1 receptors both disrupt delay period activity and behavioural performance (Goldman-Rakic et al., 2000). Furthermore, it has been shown that D1 receptor type activation can have exactly opposite effects depending on the actual task phase during a working memory experiment (Floresco and Phillips, 2001).

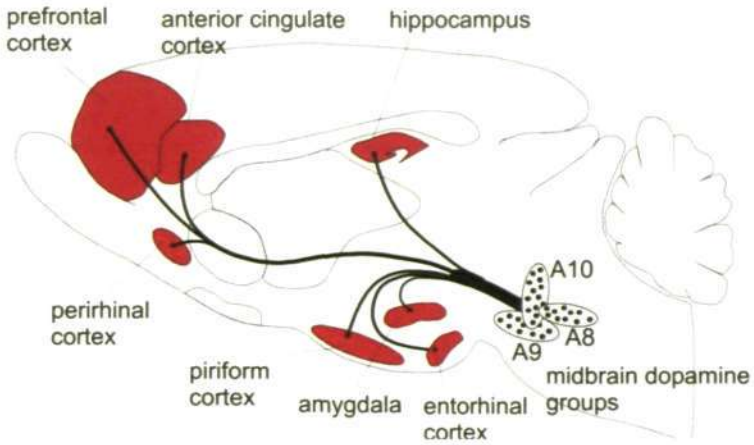

Figure 2.5 | Mesocortical DA projections in the rat brain
The mesocortical DA system originates from DA positive neurons in the VTA (A8-10) and projects mainly to prefrontal areas, the hippocampus, the perirhinal and entorhinal cortex and the amygdala.

In order to fully understand the complex effects DA imposes on working memory one has to take a close look at the changes DA introduces to single cells in the PFC. DA effects can differ between brain regions, for example DA stimulation has opposite effects on NMDA currents in the hippocampus (Hsu, 1996; Otmakhova and Lisman, 1999) compared to the PFC and striatum (Cepeda and Levine, 1998; Seamans et al., 2001a). I will focus on DA effects described in the rat PFC (see Seamans and Yang, 2004 for a comprehemsive review). There has been a long controversy about whether DA effects in the PFC are excitatory of inhibitory. Initially DA was characterised as an inhibitory neurotransmitter, based on suppressive effects of exogenous DA on firing rate (Herrling and Hull, 1980; Bernardi et al., 1982; Thierry et al., 1998). Later studies have also found excitatory effects of DA (Penit-Soria et al., 1987; Yang and Seamans, 1996). Somewhat reconciling these conflicting results, Gulledge and Jaffe (1998, 2001) illustrated that timing of DA application can be decisive for the course of DA action on excitability. DA application initially suppressed firing, but was followed by a rebound of excitability, resulting in a net increase in excitability compared to baseline about 15 minutes after the initial DA application. Such biphasic effects of DA have observed in other studies (Seamans et al., 2001b; Gorelova et al., 2002) and illustrate the necessity for time resolved measurement of DA effects.

Since then, a large number of studies have contributed to elucidating the effects of DA on biophysical properties of deep layer pyramidal cells. DA has been shown to modulate all major synaptic conductances and various voltage regulated conductances in pyramidal cells and inhibitory interneurons (Seamans and Yang, 2004).

DA (via D1 receptors) has been shown to modulate the persistent sodium current (I_{Nap}) by shifting the voltage dependent activation towards more negative voltage values, hence lowering the threshold for the occurrence of Na^+ spikes, effectively increasing excitability (Gorelova and Yang, 2000) but other studies failed to show effects of DA on I_{NaP} (Maurice et al., 2001). Furthermore, D1 receptor activation reduces a 4-aminopyridine sensitive slowly inactivating K^+

conductance (Yang and Seamans, 1996; Dong and White, 2003), which normally opposes I_{NaP}. This reduction effectively adds to the increase in excitability caused by I_{NaP} facilitation. DA also influences various voltage gated calcium channels in prefrontal neurons. D1 receptor activation reduces the half-width and amplitude of dendritic Ca^{2+} potentials (Yang and Seamans, 1996) mainly thought to be carried by L-type calcium currents. Later Young and Yang (2004) demonstrated that DA (via D1 receptors) can both transiently augment (via protein kinase A) and time-dependently suppress (via protein kinase C) L-type calcium channels. In summary, DA increases intrinsic excitability through modulation of Na^+, K^+ and Ca^{2+} currents.

In addition to intrinsic currents DA has also been shown to modulate all major synaptic currents. DA enhances NMDA receptor currents in pyramidal neurons via D1 receptor activation, but decreases NMDA receptor currents through D2 receptor activation (Zheng et al., 1999; Seamans et al., 2001a; Chen et al., 2004). DA receptor activation also slightly reduces AMPA receptor currents through D1 receptor dependent pathways (Seamans et al., 2001a; Gao et al., 2001) but see Wang and Goldman-Rakic (2004) for an account of D2 receptors enhancing AMPA current. DA modulates GABA currents in pyramidal cells in a receptor and time-dependent manner. DA itself shows a biphasic modulation of GABA currents, with an initial depression followed by a later augmentation (Seamans et al., 2001b). The initial decrease has been attributed to D1 receptor activation, and the augmentation to D2 receptor activation. Interestingly D1 receptor dependent depression of GABA currents can readily be reversed by D2 receptor activation and vice versa. Figure 2.6. shows the D1 and D2 receptor specific effects on spontaneous GABA evoked post synaptic potentials (PSP) in deep layer pyramidal cells. Here the receptor specific and time dependent effects of DA are demonstrated. In addition to modulating synaptic inputs and excitability of pyramidal cells, DA alters various biophysical properties of GABAergic interneurons in the PFC (Zhou and Hablitz, 1999; Gorelova et al., 2002; Gao and Goldman-Rakic, 2003; Trantham-Davidson et al., 2004; Kroner et al., 2007).

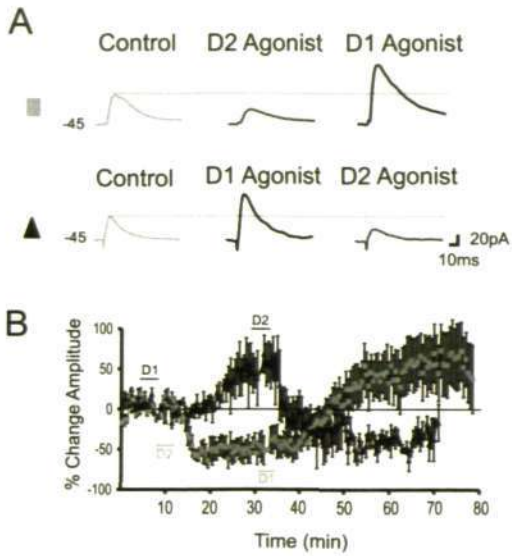

Figure 2.6 | Time dependent and reversible DA receptor specific effects on GABA IPSP's.

A) Selective DA receptor agonists have time dependent and reversible effects on post synaptic GABA PSP's. D1 receptor increases PSP amplitude, but D2 receptor stimulation decreases PSP amplitude.
B) These effects are time dependent and can be fully reversed by applying agonists for the previously not stimulated receptor type.

From Seamans et al., 2001b.

In summary, these examples illustrate the complex influence DA bears on single cell biophysics in the PFC. In an attempt to understand how these changes might explain *in vivo* effects on working memory, a range of theoretical modelling studies investigated the impact of DA on prefrontal network dynamics (Durstewitz et al., 2000a; Compte et al., 2000; Brunel and Wang, 2001; Dreher et al., 2002; Durstewitz and Seamans, 2002). In particular Durstewitz and colleagues (Durstewitz et al., 2000b; Durstewitz and Seamans, 2002) implemented a detailed biophysical network model, and showed that D1 activation stabilises persistent activity states evoked by external input fed into the model. This stabilisation can be explained by the simultaneous increase in NMDA and GABA currents, where in particular NMDA activation has been regarded as an essential prerequisite for persistent activity in recurrent networks (Wang, 1999; Durstewitz and Seamans, 2002; Shu et al., 2003; Seamans et al., 2003).

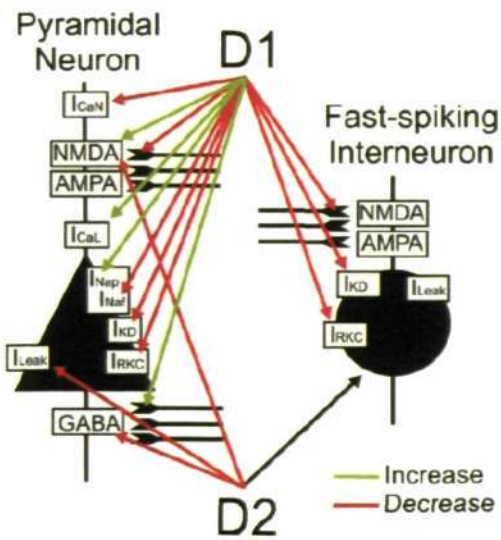

Figure 2.7 | Summary of DA effects
Dopamine modulates various intrinsic and synaptic properties in pyramidal cells and fast spiking interneurons, differentially through D1 and D2 type receptors. See text for details.
From Lapish et al., 2007.

Despite this large body of experimental and theoretical modelling work, questions still remain, especially on how modulation of intrinsic properties might influence computational properties in PFC cells and networks. In particular since intrinsic properties of neurons have recently received increased attention, e.g. as an alternative plasticity mechanism in cortical circuits (Zhang and Linden, 2003; Xu and Kang, 2005; Janowitz and van Rossum, 2006). In the following section I will outline the motivation for focussing on examining intrinsic properties of pyramidal cells, formulate some specific questions and describe the major tasks outlined in this thesis to address these questions.

2.6 Motivation and aims of this thesis

To sum up, the prefrontal cortex is an anatomically well defined region in humans, monkeys and rats that is involved in various higher cognitive functions, especially working memory. Within the PFC, specific circuits and cell types have been correlated with PFC function. DA modulation is crucially involved in working memory and has been shown to modulate a large number of biophysical parameters in neurons of the PFC. Different classes of deep layer pyramidal cells have been reported, but a systematic examination of cell type specific effects of DA has not been reported. Furthermore, morphological correlates of prefrontal function have been described (Lewis et al., 2002; Wang et al., 2006), but if or how these correlate to dopaminergic modulation is unknown.

Thus I would like to raise a few key questions that this thesis aimed to address:

- How do intrinsic single cell properties give rise to computational functions of pyramidal cell types?
- Does dopaminergic modulation of intrinsic properties differ between cell types and does that relate to distinct dynamical regimes?
- How does dopaminergic modulation of intrinsic properties affect single cell computational properties?
- How do morphological properties of pyramidal cells correlate with intrinsic properties, and more interestingly with dopaminergic modulation?

Single cell recordings in acute slices from rat PFC have been used to examine dopaminergic effects on biophysical parameters. Acute brain slices provide an instant snapshot of prefrontal networks, where reduced connectivity is outweighed by easy application of pharmacological agents both intra- and extracellularly.

To answer the questions raised above the following major tasks for this thesis are the following:

- Probe intrinsic properties of deep player pyramidal cells through a variety of protocols to characterise cell behaviour on multiple time scales.
- Examine receptor specific dopaminergic modulation of intrinsic properties of deep layer pyramidal cells through application of dopaminergic agonists (D1 and D2 agonists)
- Reconstruct digitally the morphology of recorded cells and quantitatively analyse morphological features.
- Analyse correlations between different aspects of cell function through multivariate statistical analysis, i.e. principal component analysis, hierarchical cluster analysis and analysis of variance.

3 Methods and Materials

This Chapter will describe the technical background of the experimental and analysis methods used in this study. I will briefly describe the principle of the whole cell patch clamp method and the stimulation protocols used to characterise pyramidal cells physiologically. Furthermore, I will describe principles of confocal microscopy and its use for reconstruction of neuronal morphology using biocytin tracing. In the final section, I will describe all statistical analysis methods used.

All experiments involving animals were reviewed by the University of Plymouth Ethics Committee and followed the guidelines for minimisation of animal use for research issued by the Home Office, as summarised by reduction, refinement and replacement (3 R's).

3.1 The whole cell patch clamp method

By the early 1970's, it became clear that discrete molecular entities, integral membrane proteins, were responsible for conducting electrical signals in nerve and muscle tissue. Experiments with a variety of toxins indicated that potassium and sodium channels were separate macromolecules (Hille, 1976; Armstrong et al., 1973). Inspired by discrete current changes seen in artificial membrane preparations (Bean et al., 1969), the neurophysiologists Erwin Neher and Bert Sakmann were determined to measure similar signals in a biological preparation. To reduce background noise in voltage clamp recordings Neher and Sakmann attempted to isolate a piece of membrane ("patch") from the surrounding by pressing a glass pipette to the surface of the membrane. In initial experiments, they achieved a seal resistance of around 50-100 MΩ that allowed them to resolve picoampere sized currents from acetylcholine activated currents in frog muscles (Neher and Sakmann, 1976).

The method made a breakthrough, when it was found that using clean micropipettes and slight suction increased the seal resistance to an order of magnitude ("gigaseal") (Hamill et al., 1981). This method, since then coined patch clamp, allowed the high resolution recording of currents in excised cell membrane patches and those that remain cell attached. Moreover, it allowed the application of the classic voltage clamp method in cells that are too small for intracellular recordings by high resistance ("sharp") microelectrodes. The breaking of the membrane patch gives rise to the patch clamp configuration used in this thesis, tight seal whole cell recording. After establishing the gigaseal one can deliberately break the membrane patch by applying brief

strong suction or a voltage pulse. This "break-in" results in electrical and diffusional access of the pipette internal to the cytoplasm of the cell, without altering the seal resistance between glass and membrane. If the access resistance between pipette electrode and cytoplasm is lower than the cell membrane resistance, a small cell is effectively voltage clamped to the pipette potential and the overall activity of ion channels can be measured. Similarly the change in voltage difference across the membrane can be measured in the current clamp mode where the current flow through the membrane is held constant, which allows observation of voltage changes, i.e. the natural physiological excitation patterns. This configuration is called tight whole cell recording (Marty and Neher, 1995), which is now the most common used configuration. This technique has later been adapted to record neurons in acute slices of brain tissue (Yamamoto and McIlwain, 1966; Lynch and Schubert, 1980; Sakmann and Stuart, 1995). While recording from neurons with complex dendrites the voltage clamp assumption only holds true for the soma, and care has to be taken when interpreting signals from remote synapses or intrinsic currents (Spruston et al., 1993; White et al., 1995). In the last 15 years the patch clamp technique has contributed a wealth of data on neuronal properties and is therefore the method of choice for analysing single cell electrophysiology.

Whole cell patch clamp in acute slices of the rat PFC:

Whole cell patch clamp recordings and deep layer pyramidal cells were performed in acute slices from adult rat PFC as described previously (Moyer and Brown, 1998; Durstewitz and Gabriel, 2007).

Sprague Dawley rats (55-80 d, Charles River, UK) were killed according to Home Office guide lines (Schedule 1) and then decapitated. The rapidly dissected brain is immersed for 1 min in cold (4°C), oxygenated (5% CO_2, 95% O_2) artificial cerebro-spinal fluid (ACSF) (in mM): NaCl (125), $NaHCO_3$ (25), glucose (10), KCl (3.5), NaH_2PO_4 (1.25), $CaCl_2$ (0.5), $MgCl_2$ (3); pH 7.45, osmolarity 300 ±5 mOsm.

Coronal slices (300-350 µm) containing the prelimbic-infralimbic region of the PFC were cut on a Vibroslice MA752 (Campden Instruments, Loughborough, UK) and transferred into heated (37 °C) ACSF solution with $CaCl_2$ changed to 2 mM and $MgCl_2$ changed to 1 mM. After 20 min, ACSF was allowed to cool down to room temperature for at least 40 min before recording. All solutions were constantly oxygenated with 95% O_2/5% CO_2 throughout the experiments.

Slices were placed in a Warner Instruments recording chamber and perfused with recording solution through a gravity fed system at a rate of 2-3 ml/min. The solution was preheated up to about 26° C through a regulated power supply and heated up to 33-35°C by a Warner

Instruments bath chamber heating system (Harvard Apparatus Ltd, Edenbridge, UK) regulated by a TC-10 temperature control system (NPI Electronics, Tamm, Germany).

Slices were viewed on a Zeiss Axioskop FS Microscope using a 40x 0.9 NA water immersion objective plus additional ocular tube magnification (2x) using differential interference contrast (DIC) optics (Luigs und Neumann, Ratingen, Germany) and imaged by a Hamamatsu analogue video camera (Hamamatsu Photonics Deutschland GmbH, Herrsching am Ammersee, Germany).

Recording pipettes were pulled from thick walled borosilicate glass on a Sutter P-97 pipette puller to a resistance of 3-8 MΩ (~ 20 μm tip) and filled with freshly prepared internal solution containing (in mM): K-gluconate (115), 4-(2-hydroxyethyl)-1-piperazineethanesulfonicacid (10), $MgCl_2$ (2), KCl (20), MgATP (2), Na_2-ATP (2), and Guanosine-5'-triphosphate (0.3) (pH = 7.3, 285 ±5 mOsm). The internal solution also contained biocytin (15 mM) for later morphological identification of recorded cells.

All recordings were either made with Axoclamp 2B (Molecular Devices Ltd, Wokingham, UK) or NPI SEC05LX amplifier (NPI Electronics, Tamm, Germany) using a 0.1x headstage. Data was acquired at sampling rates of 5-30 kHz by a PC16E A/D (National Instruments Germany GmbH, München, Germany) card mounted to a Dell Precision 5510 (Dell Products, Berks, UK) which ran a custom made Labview-based recording software, written by Lee Campbell (Salk Institute, La Jolla, CA).

All pharmacological experiments included bath applied specific antagonists to all major synaptic amino acid receptors, i.e. NMDA blocker AP-5 (10 μM, Sigma, UK), AMPA blocker DNQX (10 μM, Sigma, UK), GABAa blocker Picrotoxin (50 μM Tocris, Bristol, UK) and GABAb blocker Phaclofen (100 μM, Tocris, Bristol, UK).

All experiments included the D1-receptor agonist SKF-38983 or SKF 81297 (50 μM), the D2-receptor agonist quinpirole (10 μM), added to the ACSF, where the range of concentrations were chosen based on previous studies (Seamans et al., 2001b, 2001a; Trantham-Davidson et al., 2004) A typical recording lasted around 50 minutes.

Although this is a standard procedure for conducting whole cell patch clamp recordings in brain slices, this slicing procedure will most likely introduce a bias in the sample of selected cells for patching under visual control. Only robust cells will survive the grave procedure, so that cells with large cells bodies (supposedly more robust) might be overrepresented in the sample as opposed to the *in vivo* situation. In the current study I have selectively patched cells from the posterior side of every slice since cells in the PFC are slightly angled in relation to the sagittal cutting plane, which increased the likelihood of recording from cells with preserved apical dendrites.

Yet, since the method is literally identical to hundreds of other *in vitro* slice studies on prefrontal cortical pyramidal cells, this bias would have been present in all studies. Thus the results are comparable to other *in vitro* slice studies, but caution has to be used when relating the current results to *in vivo* studies.

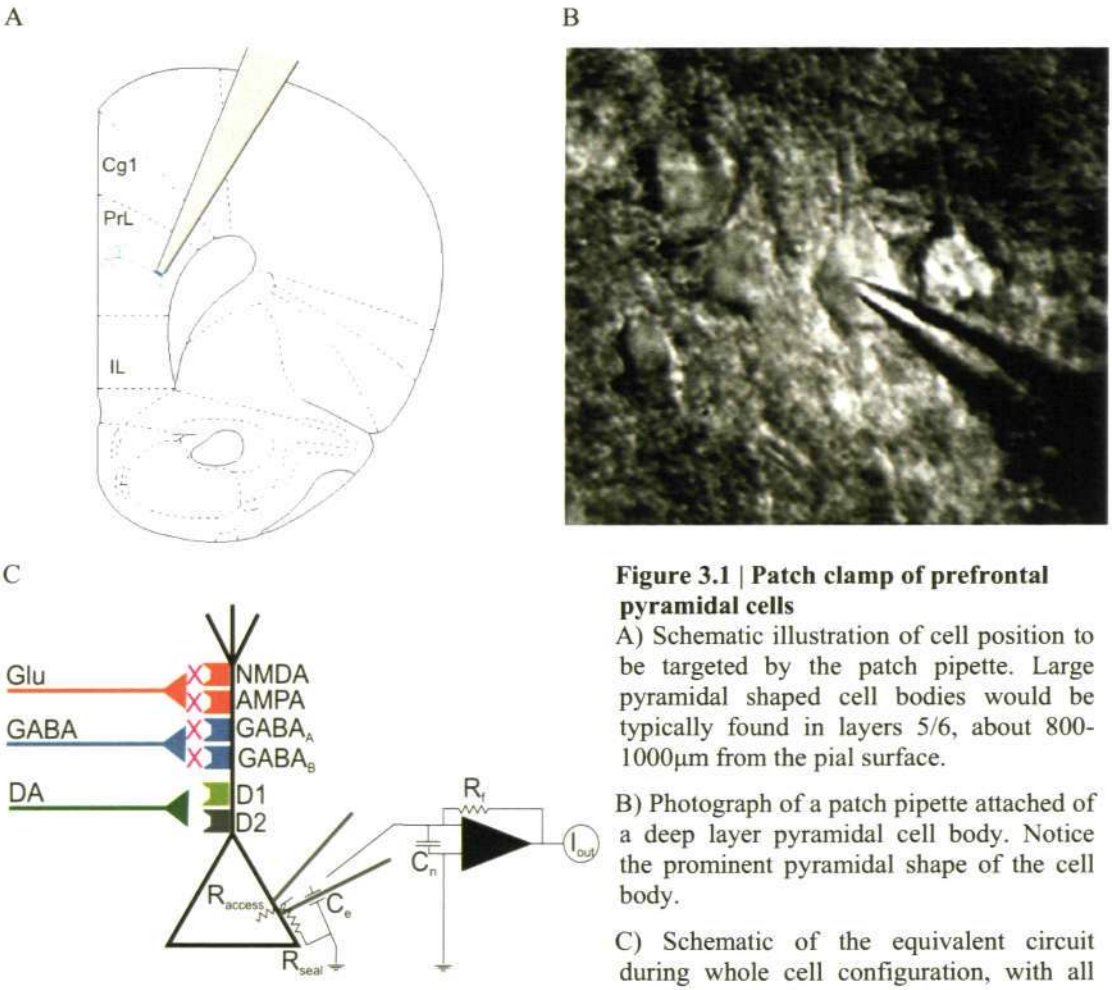

Figure 3.1 | Patch clamp of prefrontal pyramidal cells

A) Schematic illustration of cell position to be targeted by the patch pipette. Large pyramidal shaped cell bodies would be typically found in layers 5/6, about 800-1000μm from the pial surface.

B) Photograph of a patch pipette attached of a deep layer pyramidal cell body. Notice the prominent pyramidal shape of the cell body.

C) Schematic of the equivalent circuit during whole cell configuration, with all synaptic inputs blocked by selective antagonists, and activation of either D1 or D2 receptors through specific agonists.

3.2 Stimulation Protocols and Analysis of Electrophysiology Data

I have applied 5 different protocols to probe passive and active properties of recorded cells. Table 3.1 shows a summary of all stimulation protocols used.

To obtain an estimate for the passive properties of a recorded cell I applied 200 millisecond steps of -25 pA, repeated between 50-100 times. The responses were inspected by eye for obvious artefacts (e.g. 50 Hz noise), noisy traces were removed, and responses were averaged and then fitted to a single exponential function. Figure 3.2 shows an example trace (A), the average of 83 injections and exponential fit to the average voltage trace (B). The input Resistance was estimated by a linear fit on the steady state voltage response to a series of brief hyperpolarising and depolarising current steps (Figure 3.3).

The excitability of deep layer pyramidal cells was probed by 3 different protocols: in voltage clamp mode through injection of a series of voltage steps; in current clamp mode through increasing and decreasing current ramps and through 25 s long current steps.

In voltage clamp I used a series of voltage steps, ranging from -80 to 0 mV, to record current responses. From the current responses I calculated the steady state current as the mean of the last 200 ms of the voltage step. Figure 3.4 shows an example series of voltage steps and measured current responses (A) and the resulting voltage-current curve (B). From this curve the reversal potential was estimated by detecting the zero crossing of a linear fit between the two current values just below and above 0 mV. To further characterise the V-I curve, I extracted the minimum slope of the curve, which effectively returns the inflection point (◊), the current value of the inflection point and the difference between inflection point and the local minimum of the curve ("bump deepness").

To assess the excitability of recorded cells further, I injected slowly increasing and decreasing current ramps spanning a range of current from 0-300 pA over a time of 9 seconds. Figure 3.5 shows example traces of ramp currents and respective voltage traces in the control condition. In this example the rheobase current for the increasing ramp is lower than for the decreasing ramp, which was the case for most recorded cells. From this I also extracted the maximum firing rate observed during each ramp (red circles).

To quantify excitability during an extended period of time I injected series of 25 second long current steps. Figure shows 3 out of 10 pulses (bottom) and respective voltage traces (top) from a typical example of a 25 s current pulse injection. Figure 3.6 B shows the respective current v firing rate curve (f/I) based on the steady state firing rate (i.e. the last 5 seconds of the pulse). Figure 3.6 C shows a square root fit ($a\sqrt{x} + b$) to zero ISI (spike latency) and last ISI (steady state FR) at different current steps. As input for resulting cluster analysis I extracted the maximum slope and the onset of the f/I curve, coefficient (a) and y-intercept (b) of the square

root fits for zero and last ISI. Furthermore the coefficient of variation was measured on a spike train of at least 100 spikes.

The coefficient of variation (C_v) describes the dispersion of a probability function and is commonly used to assess irregularity in time series (especially spike trains). The C_v is given by

$$C_v = \frac{\sigma_{ISI}}{\mu_{ISI}},$$

where σ and μ are the standard deviation and the mean of the ISI of a given spike train.

Table 3.1 Stimulation protocols

Protocol	**Passive**	**Short V-I**	**Ramps**	**Long V-I**	**I-V**
Recording mode	CC	CC	CC	CC	VC
Type	Single Step	Steps	Ramp	Steps	Steps
Stimulus length	200 ms	500 ms	9 s	30 s	500 ms
Amplitude range	--50 pA	-150-150 pA	0 - 300 pA	-100 – 300 pA	-80-0 mV
n times applied	50 100	1	1	1	1

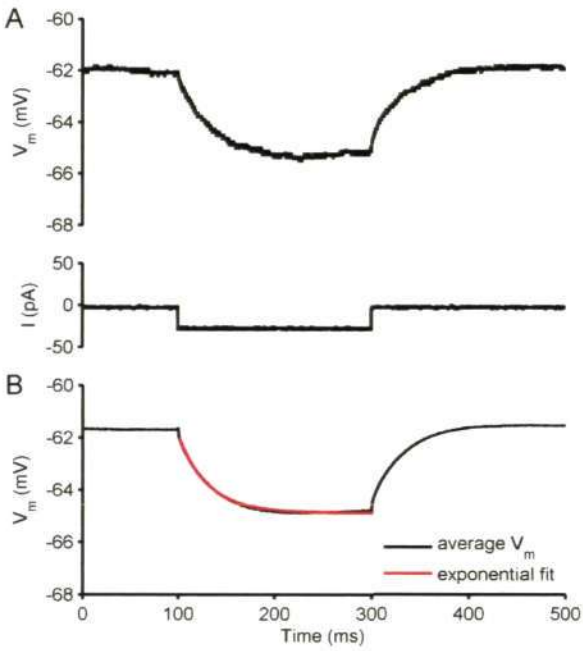

Figure 3.2 | Estimating the membrane time constant
A) Typical single trace showing voltage response (top) and injected current (bottom).
B) Average of all included voltage responses and single exponential fit in red.

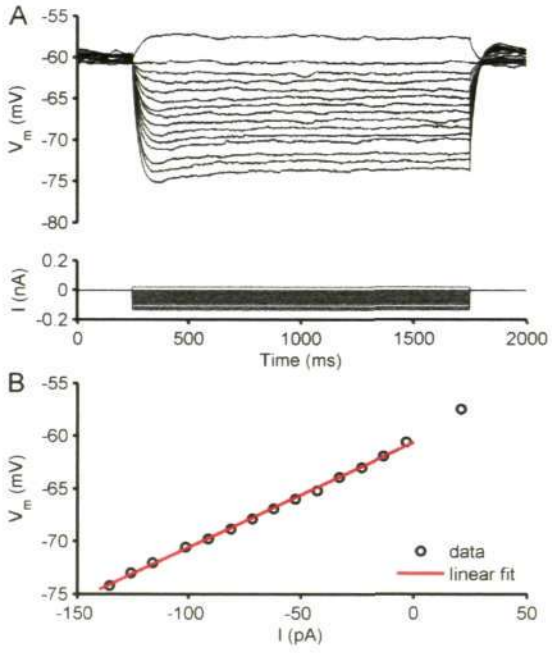

Figure 3.3 | Estimating the input resistance
A) Example trace showing a voltage response (top) to a series of hyperpolarising current steps (bottom).
B) Linear fit to current-voltage plot

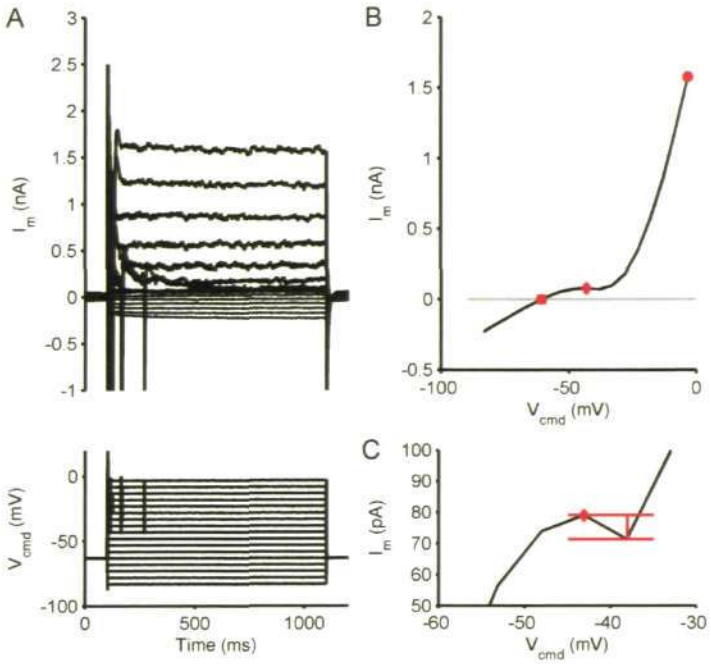

Figure 3.4 | Voltage clamp step stimulation
A) Example of voltage clamp step stimulation. Series of voltage steps (-80-0 mV) were injected and the total steady state (>500 ms) membrane current is measured.
B) Resulting I-V curve with the resting potential (■, E(rev)), maximum slope (♦, dV/dI) and the maximum current (●) annotated.
C) Magnified view of B. The bump height is the difference between the local maximum and minimum of the I-V curve.

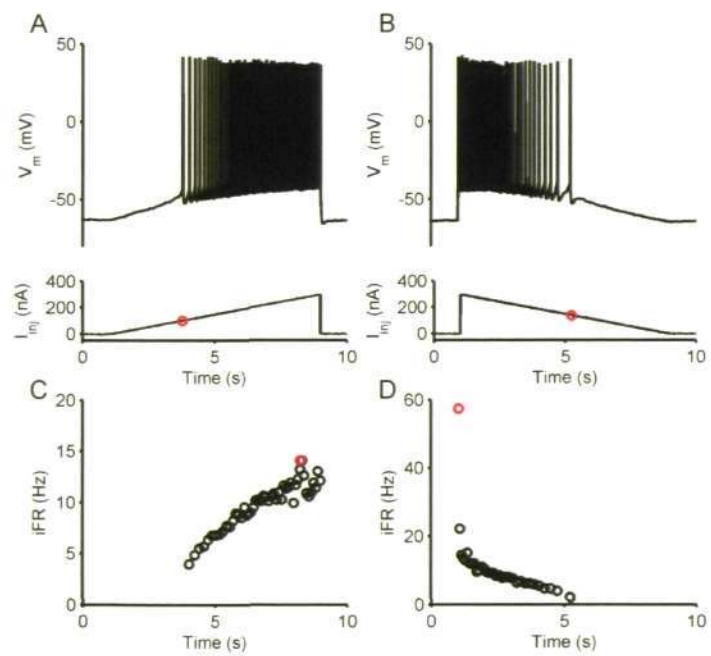

Figure 3.5 | Current clamp ramp stimulation
A) Example traces (top) from upward ramp injection (bottom).
B) Example traces (top) current ramp injection (bottom). Red circles indicate rheobase current.
C) Instantaneous firing rate (iFR) from spike train in A. Red circle indicates maximum iFR.
C) iFR from spike train in B. Red circle indicates maximum iFR.

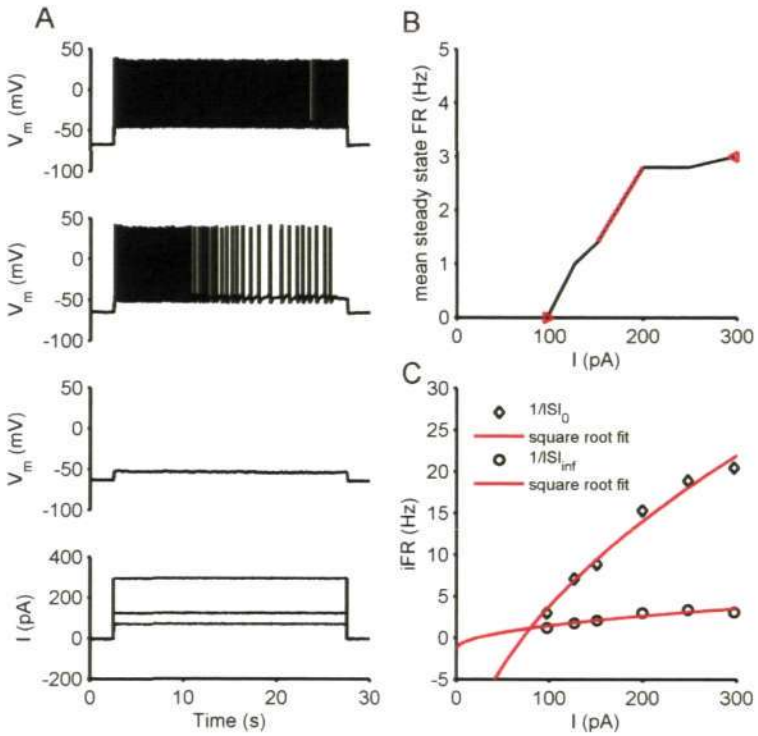

Figure 3.6 | Long current step stimulation
A) Example of long (25 s) current step injection, for clarity only 3 out of 8 steps are shown.
B) Steady state f-I curve, with onset, maximum slope and max firing rate annotated.
C) Resulting square root fit for the average instantaneous firing rate (iFR) for the spike latency ($1/ISI_0$) and average iFR during the last 5 seconds of the step ($1/ISI_\infty$).

Table 3.2 Characteristic physiological variables

Protocol	#	Variable	unit	Description	Method
Passive	1	*Tau*	ms	Passive membrane time constant estimate	Exponential fit to 200 ms, -0.1 pA current step
	2	*Sag*	mV	I_h estimate	Difference between exponential fit and average Vm trace at the end of step.
Short VI	3	*R(in)*	MΩ	Input resistance	Linear fit of current clamp steps against subthreshold voltage responses
Ramps	4	*Rmp (u): rheobase*	pA	Minimum current for eliciting an AP during upward ramp	Time of first AP from upward ramp injection
	5	*Rmp(d): rheobase*	pA	Minimum current for eliciting an AP during downward ramp	Time of last AP from downward ramp (down) injection
	6	*Rmp(u): max (f)*	Hz	Maximum instantaneous frequency during upward ramp	Max of 1/ISI from upward ramp
	7	*Rmp(d): max (f)*	Hz	Maximum instantaneous frequency during downward ramp	Max of 1/ISI from downward ramp
Long VI	8	*V-I: onset*	pA	Onset of f/I curve	current step (i-1), whit step(i) being the first step to evoke AP's
	9	*V-I: max(dV/dI)*	Hz/pA	Maximum slope of f/I curve	max of diff(f)
	10 11	*V-I: a (ISI_0)* *V-I: b(ISI_0)*	-	Square root fit to latency to first spike for all steps	fit a*sqrt(I)+b to I vs ($1/ISI_0$)
	12 13	*V-I: a(ISI∞)* *V-I: b(ISI∞)*	-	Square root fit to last ISI for all steps	fit a*sqrt(I)+b to I vs (1/ISI∞)
	14	*V-I: CV*	-	CV all spikes from step that elicited more than 100 spikes	std(ISI) / mean(ISI)
VC steps	15	*E(rev)*	mV	Reversal potential	Zero crossing of I-V curve voltage clamp steps
	16	*I-V: max(I)*	pA	Maximum current	max (I)
	17	*I-V: max (dV/dI)*	mV/pA	Maximum slope of steady state V-I curve	max(diff(V)/diff(I))
	18	*I-V: max (I (dV/dI))*	pA	Current at maximum slope of V-I	I(max(diff(V)/diff(I)))
	19	*I-V: bump*	pA	Differences between max slope and local minimum of V-I	I (max(diff(V)/diff(I))) - $\min(I)_{loc}$

3.3 Biocytin tracing, confocal imaging and an reconstruction of neural morphologies

Since the first descriptions of neuronal morphologies by Ramon y Cajal and Golgi (Cajal, 1899) in the late 19th century various methods have been developed to visualise cellular morphology of neurons in brain tissue. In particular, intracellular labelling methods were developed to stain individual neurons (Snow et al., 1976; Cullheim and Kellerth, 1978). One widely used approach in combination with whole cell patch clamp recordings is to add biocytin (a weight analogue of biotin) to the intracellular solution of the patch pipette (King et al., 1989). Biocytin is a small molecule (MW = 244) and will easily diffuse into the cell inside and into distant dendrites within 20-30 minutes if added to the inside of a patch pipette. Biocytin has a very high affinity to streptavidin ($K_d = 10^{-15}$), a tetrameric protein that binds up to 4 molecules of biocytin. This highly specific, but non-covalent, binding can be used to selectively visualise the morphology of recorded neurons by using a streptavidin-fluorophore conjugate and confocal laser scanning microscopy (CLSM). CLSM was invented in the late 1950's (Halbhuber and König, 2003), but only the further development of crucial components, i.e. laser as a light source, computer for control and data storage, lead to the first instruments being commercially available in the late 1980's. In design CLSM is similar to conventional epi-fluorescence microscopy, only that the high energy UV light source (e.g. Hg arc lamp) is replaced by a laser. This provides a much more focussed and energy dense excitation of fluorescent reporter molecules (Hibbs, 2004).

The principle setup for a confocal microscope is shown in Figure 3.7. The laser light is reflected onto the specimen by means of a dichroic mirror which allows selective filtering of different wavelengths. In particular high intensity excitation light (green) reaches the specimen, but only the elicited fluorescence (red) passes the dichroic mirror to be detected by a photomultiplier tube (PMT). Two pinhole apertures are used, firstly for focussing the laser beam (precise spatial excitation) and secondly to reduce the amount of scattered, out of focus-light just before the fluorescence signal enters the PMT. An image is formed using scanning mirrors to deflect the laser beam in x and y direction, to serially scan points in a defined area within the focal plane. After digitising the analogue intensity signal of the PMT, the image is a grey scale bitmap with either 8-bit, 12-bit or 16-bit resolution, depending on the sensitivity range of the PMT and software settings. A full x-y scan represents an optical slice of the specimen ('optical sectioning'). The 'depth' of the optical slice within the specimen depends on the focus plane chosen with the objective. Since the excitation through the laser source is focussed through the pinhole, only a thin section of the specimen is imaged, and by taking a series of consecutive images at different focal planes, one can infer 3-dimensional information about the specimen (Carrington et al., 1999).

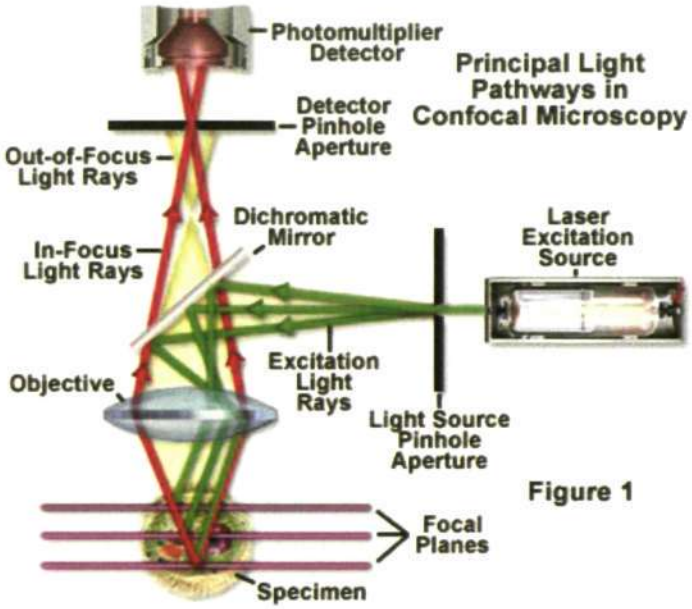

Figure 3.7 | Light pathways in a confocal microscope
Light from the laser excitation source passes the light source pinhole and is reflected by a dichroic mirror onto the specimen. Evoked fluorescent light passes the objective in opposite direction passes the detector pinhole and is detected by the photomultiplier. From www.olympusfluoview.com

Some of the earliest applications of confocal microscopy were in the field of neuroscience. For example Egger and Petran (1967) imaged unstained brain and ganglion cells. Later, lamprey spinal cord has been imaged using injected fluorescent dyes (Wallén et al., 1988) and images of individual neurons have been used to reconstruct complete cell morphologies (Carlsson et al., 1989). Since these early applications of confocal microscopy to neuroscience questions, a wealth of new techniques and applications has been developed (Wilt et al., 2009).

For the current analysis, fixed brain slices (350 µm) were sandwiched between two coverslips to enable imaging from both sides, since the maximal penetration depth of confocal lasers is about 150-200 µm. Image stacks were acquired with a 10x-Neofluar objective using small pinhole diameter and long pixel dwell times to enhance signal to noise ratio in the stacks. Image stacks were highly oversampled in the z-direction to obtain nearly cubic voxel dimensions. Indeed the greatest disadvantage of using confocal image stacks is the limited z resolution (as opposed to 2-photon LSM). Since the laser light passes all the tissue above the focal plane, all fluorescent markers above the focal plane will be excited by the laser. Out of focus light in the x-y direction can be efficently removed by the confocal apertures, as opposed to diffracted light in z-direction (Boutet de Monvel et al., 2001). Combined image stacks were imported into the Neurolucida software package and traced manually. Due to the use of a low magnification objective and occurence of significant z-blur, all diameter measurements were excluded from the analysis (see below). Figure 3.8 shows a maximum intensity projection from an example image stack. The advantage of using low magnification image stacks lies in being able to capture the whole neuron morhology at once, although two stacks had to be acquired from each side, to avoid resectioning of the slices.

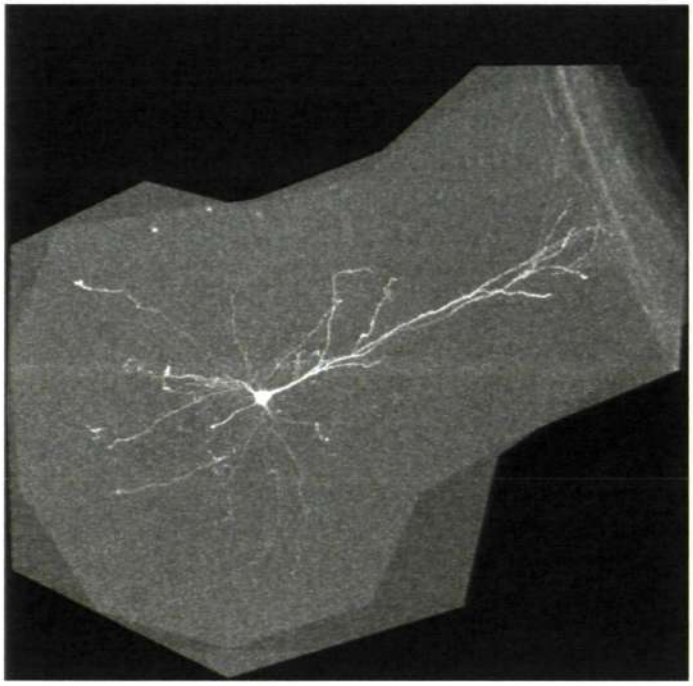

Figure 3.8 | Maximum intensity projection of an example confocal image stack.
The image is combined from two z-stacks, imaged with a 10x Neofluar objective, from both sides of the slice. Apical and basal dendrites are clearly visible.

Materials for histological procedures, confocal imaging and morphological reconstruction

After recording and filling cells with biocytin, brain slices were fixed in 100 mM phosphate buffered saline (PBS), adjusted to pH =7.4, containing 1% paraformaldehyde at 4 °C for at least 24 h. After extensive rinsing in PBS (2x5 mins + 3x30 mins) slices were incubated overnight with a streptavidin Alexa-488 conjugate (5 µM) in PBS plus 0.4 % Triton X.

After rinsing in PBS (2x5 mins + 3x30 mins) slices were sandwiched between two coverslips (No. 0) using SecureSeal imaging spacers (Grace Bio-Labs, from Stratech Scientific Ltd., Newmarket, UK) and Vectashield mounting medium (Vector Laboratories Ltd., Peterborough, UK).

Alexa-Strepatvidin labelled cells were visualised by confocal laser scanning microscopy using a Zeiss 510 LSM with Arg/He laser with a 10x Neofluar (NA 0.3). Z-stacks of Images were acquired every 1 µm with a high pixel sampling time (~25 µs) to increase the quality of acquired images. Slices were imaged from both sides as one photon excitation of fluorescent probes is limited by increasing scatter of light when imaging deeper in the tissue, which results in a penetration depth of max 150-200 µm (Rodriguez et al., 2003).

After inspection of max intensity projections of Z-stacks only cells with minor damage to basal and apical dendrites were used for further morphological analysis.

Z-stacks were sometimes post-processed with deconvolution algorithm in ImageJ (Collins, 2007) and reoriented using ImageJ and the stack alignment plug-in (JA Parker, Harvard Medical School, Boston, MA). Then stacks were imported to the VIAS software package (Wearne et al., 2005) for alignment and volume integration into one Z-stack volume. These combined Z-stacks were imported to the Neurolucida software package (Microbrightfield Europe, Magdeburg, Germany) and the cell morphology was digitally reconstructed in 3 dimensions.

3.4 Morphometric Analysis

The morphology of reconstructed neurons was analysed within the software tool NeuroExplorer, which is part of the Neurolucida package and includes a variety of measures that quantify properties of somatodendritic morphology. The analysis results were copied to spreadsheets (OpenOffice) and exported to Matlab through custom OOBasic scripts.

The neuronal dendrite can be described through several quantitative measures. Each dendritic main branch starts at the root segment (usually the soma) and branches out into smaller dendrites. Simple measures (Figure 3.9 A) include the number of branchings (node), or segments, and the number of endings. These numbers can be calculated either per main branch or for the whole neuron. Furthermore segments can be labelled by segment order, which counts the number of previous branchings that occurred before accessing a segment by starting from the root segment. For each node one can also calculate the distance from the current node to the root segment, either along the dendrite or in a straight connecting line (Figure 3.9 B). The ratio of the two is called the node's tortuosity and gives an indication of how "twisted" the path up to that particular node is.

Branch angle analysis (Figure 3.9 C, D) is concerned with characterizing the direction branches take after a branching. A number of different measurements are possible when considering the change in direction between a branch and the sub-branches that meet at a node. Angles can measured locally (planar angle) or with respect to the coordinate system formed at the root segment. For this study only the planar angle was considered as it represents the local structure of the neuron. The planar angle is the angular value describing the change in direction from one branch to the next branch.

The NeuroExplorer analysis software offers fractal dimension as a global measure of neuronal complexity. In detail, the fractal dimension, D, is a statistical quantity borrowed from fractal geometry, that gives an indication of how completely a geometric structure (or fractal) is filling space. This measure has been adopted to quantify dendritic morphology of cortical neurons.

There are various methods for obtaining D (Smith et al., 1996; Jelinek and Fernandez, 1998). The NeuroExplorer software has a box counting method implemented that has been used:

$$k - D(x) = \lim_{q \to 0} \frac{log_2\left(Q_q(x)\right)}{-log_2(q)}, \quad Q(x) = N_{Boxes}$$

which can be approximated by:

$$k - D(x) = \frac{n\sum_{i=1}^{n} x_i y_i - \sum_{i=1}^{n} x_i \sum_{i=1}^{n} y_i}{[\sum_{i=1}^{n} x_i]^2 - n\sum_{i=1}^{n} x_i^2}$$

One other popular analysis method of dendritic morphology is Sholl analysis, which places concentric cycles in a fixed interval (Δr) around a neuron using the soma as origin and counts relevant structures, such as number of dendrites, branchings (nodes) and endings that fall in every cycle (Sholl, 1953). In the current analysis apical and basal dendrites were subjected to separate Sholl analyses and the resulting histogram was fitted either with a bimodal (apical dendrite) or a unimodal (basal dendrite) Gaussian. From the Gaussian the medium, the standard deviation and the scaling (amplitude) for each peak were used for further analysis.

Dendritic Hull Analysis

In a study on axonal morphology Dumitru et al. (2007) introduced a manual hull analysis, where separate polygons (tiles) were drawn that enclosed soma, dendrites and axon. This gives a measure of how much space is covered by the respective part of the cell morphology and various variables can be calculated based on the coordinates of the polygon. For this study tiles were drawn around soma, basal and apical dendrite to quantify gross morphological differences dendrite structure. Figure 3.10 shows an example reconstruction of a single neuron. The red box indicates the limits of the image stack, whereas the manual hulls applied to soma, basal and apical dendrite are indicated as grey shadows at the bottom of the image stack volume. NeuroExplorer also features an automatic hull analysis that calculates an area and perimeter of a 2D hull, and volume and perimeter of a 3D hull applied to the neuron morphology.

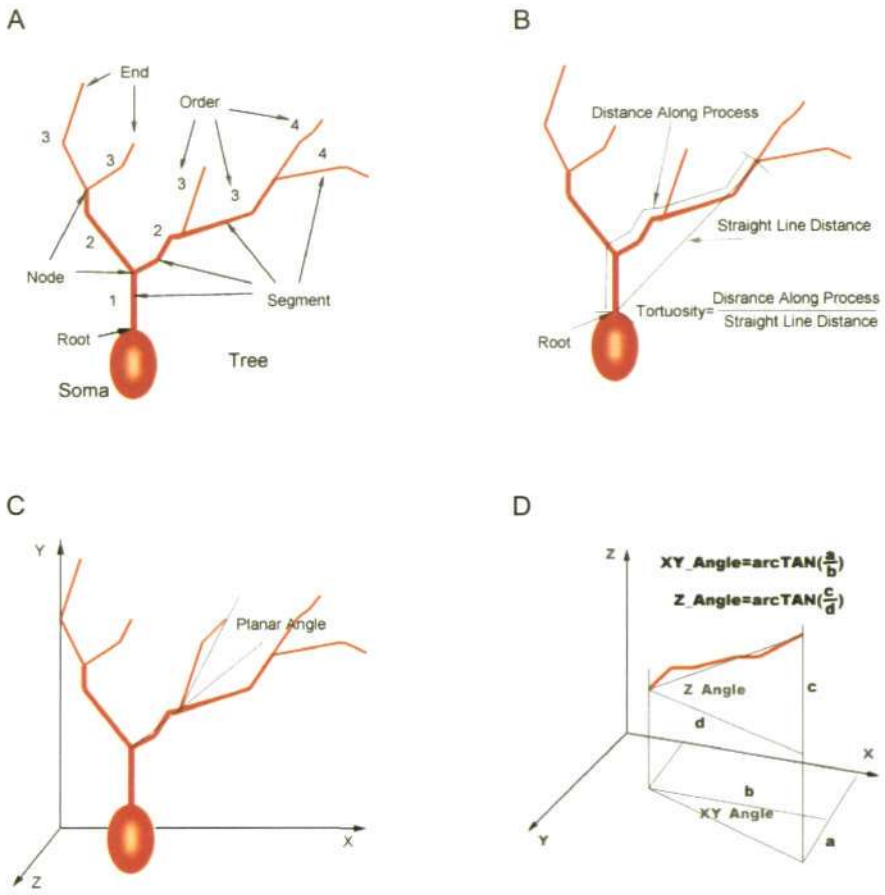

Figure 3.9 | Dendritic tree analysis
Quantification of dendritic structure through segment properties, see text for details. Illustrations from http://microcircuit.epfl.ch/

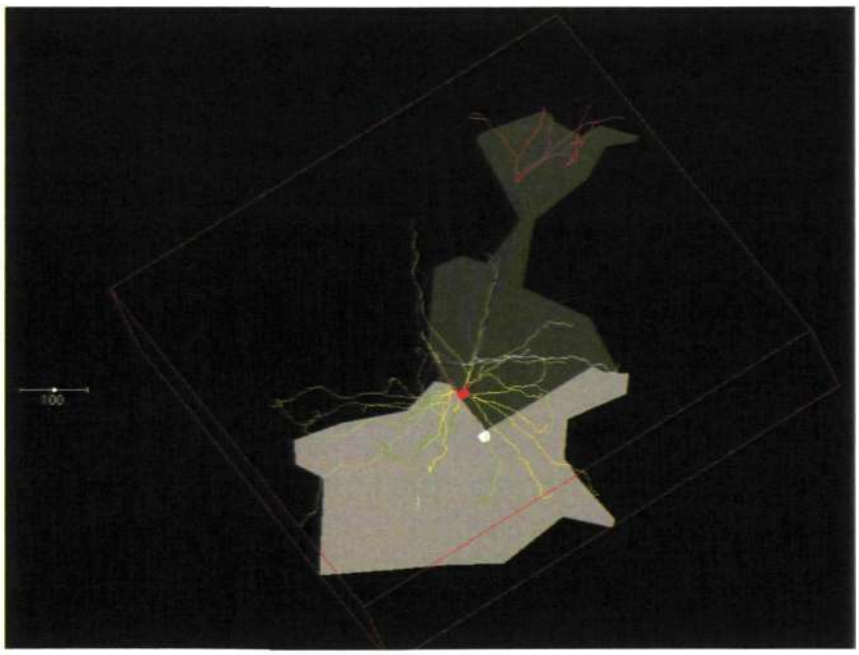

Figure 3.10 | Manual hull analysis of somatodendritic morphology
Hulls are placed around the neuron morphology, by manually connecting dendrite end points. This is done for the apical and basal dendrite, and for the soma (white and grey shapes).

For all hulls, manual and automatic, and the soma shape NeuroExplorer features a series of unit free measures that quantify form factors of these polygons:

Aspect ratio,

$$Apect\ ratio = \frac{MaxDiameter}{MinDiamter}$$

Compactness,

$$Compactness = \frac{\sqrt{\frac{4}{\pi}\ Area}}{MaxDiameter}$$

Form Factor,

$$Form\ Factor = \frac{4\ \pi\ Area}{Perimeter^2}$$

Solidity,

$$Solidtity = \frac{Area}{ConvexArea}$$

Roundness,

$$Roundness = \frac{4\ Area}{\pi\ MaxDiameter^2}$$

Convexity,

$$Convexity = \frac{ConvexPerimeter}{Perimeter}$$

All of these measures were calculated for each manual and automatic hull and included for further analysis. In total 62 morphometric variables were calculated which are shown in Table 3.3.

Table 3.3 Morphometric variables

#	whole neuron/soma (units)	#	Basal (units)	#	Apical (units)
1	*all hull auto 2d area (μm^2)*	15	*basal tile perimeter (μm)*	38	*apical tile perimeter (μm)*
2	*all hull auto 2d perimeter (μm)*	16	*basal tile area (μm^2)*	39	*apical tile area (μm^2)*
3	*all hull auto 3d volume (μm^3)*	17	*basal tile feret max (μm)*	40	*apical tile feret max (μm)*
4	*all .hull auto 3d surface (μm^2)*	18	*basal tile feret min (μm)*	41	*apical tile feret min (μm)*
5	*all fractal (#)*	19	*basal tile aspect ratio (#)*	42	*apical tile aspect ratio (#)*
6	*soma perimeter (μm)*	20	*basal tile compactness (#)*	43	*apical tile compactness (#)*
7	*soma area (μm^2)*	21	*basal tile convexity (#)*	45	*apical tile convexity (#)*
8	*soma feret max (μm)*	22	*basal tile form factor (#)*	46	*apical tile form factor (#)*
9	*soma feret min (μm)*	23	*basal tile roundness (#)*	47	*apical tile roundness (#)*
10	*soma aspect ratio(#)*	24	*basal tile solidity (#)*	48	*apical tile solidity (#)*
11	*soma compactness (#)*	25	*basal tile dsoma (μm)*	49	*apical tile dsoma (μm)*
12	*soma form factor (#)*	26	*basal n dendrites (#)*	50	*apical n nodes (#)*
13	*soma roundness (#)*	27	*basal n nodes (#)*	51	*apical n ends (#)*
14	*soma solidity (#)*	28	*basal n ends (#)*	52	*apical total length (μm)*
		29	*basal total length (μm)*	53	*apical mean length (μm)*
		30	*basal mean length (μm)*	54	*apical cv length (#)*
		31	*basal cv length(#)*	55	*apical mean turtoisity (#)*
		32	*basal mean turtoisity (#)*	56	*apical cv turtoisity (#)*
		33	*basal cv turtoisity (#)*	57	*apical sholl ratio (#)*
		34	*basal sholl ratio (#)*	58	*apical sholl mean 1 (μm)*
		35	*basal sholl mean 1 (μm)*	59	*apical sholl std 1 (μm)*
		36	*basal sholl std 1 (μm)*	60	*apical sholl mean 2 (μm)*
		37	*basal sholl scale (#)*	61	*apical sholl std 2 (μm)*
				62	*apical sholl scale (#)*

3.5 Statistical analysis methods

The analysis of the obtained datasets was carried out with the aim of characterising and classifying cells in the high dimensional parameter space spanned by all variables describing electrophysiology and morphology of the recorded cells. Since the number of cells was small compared to the variables, it seemed appropriate to first reduce the complexity of the dataset, before establishing similarity between cells. This problem is known as p<<N, with p being the number of documents (here: cells) and N being the number of features (here: variables) (Hastie et al., 2009). Various methods have been proposed to solve the p<<N problem, but a series of recent studies from the Rafael Yuste's lab have successfully applied a combination of principal component analysis (to reduce complexity or dimensionality) and hierarchical cluster analysis (to assess similarity) to analyse large datasets of physiological and morphological variables (Kozloski et al., 2001; Tsiola et al., 2003; Dumitriu et al., 2007). The current analysis uses a similar but slightly modified approach.

Principal component analysis

Principal component analysis (PCA) is a dimensionality reduction technique that describes a high dimensional dataset through rotated subset of these variables (Jolliffe, 2004). PCA is an orthogonal linear transform that projects a given dataset into a new set of coordinates such that new coordinates are chosen to maximise variance within the dataset. The largest variance is projected to the 1st coordinate (1st principal component), the second greatest variance to the 2nd coordinate and so on. This can be easily achieved by calculating a singular value decomposition (SVD) of the covariance matrix. If X represents the original data matrix,

$$Y = (y_i, \cdots, y_n), \quad y_i = x_i - \bar{x}$$

represents the centred data matrix, where

$$\bar{x} = \sum_i \frac{x_i}{n}$$

The covariance matrix (ignoring the factor 1/n) is given by:

$$\sum_i (x_i - \bar{x})(x_i - \bar{x})^T = YY^T$$

Principal directions u_k and principal components v_k are eigenvectors satisfying:

$$YY^T u_k = \lambda_k u_k$$

$$Y^T Y\, v_k = \lambda_k v_k$$

$$v_k = Y^T \frac{u_k}{\lambda_k^{1/2}}$$

These are the defining equations for the SVD of Y:

$$Y = \sum_k \lambda_k u_k v_k^T$$

Elements of v_k are the projected values of data points on the principal component u_k. In effect PCA provides a method of eliminating correlations in a given dataset and lays emphasis on high variance variables. Presumably these variables are more useful at distinguishing differences between individual items in a dataset. Here the MATLAB statistics toolbox function `princomp` is used, which implements the steps described above.

Hierarchical Cluster Analysis

Cluster analysis is a method related to unsupervised learning that seeks to classify and group entities based on a multivariate dataset describing these entities (Jain and Dubes, 1988; Jain et al., 1999). Cluster analysis is an exploratory analysis method, i.e. there is no a priori statistical model formulated of how data is correlated. Instead one wishes to establish groups based on similarity between individual entities. An entity is defined by a pattern e.g. a vector of continuous valued measurements. In the simplest case similarity can be defined as the inverse of the Euclidean distance, but various similarity measures are used. Quantitative similarity allows assignment to groups by an iterative algorithm (linkage method) and resulting groups (cluster) can then be used to establish statistical properties.

There are different approaches to cluster analysis, the most prominent techniques being K-means clustering and hierarchical clustering. Hierarchical cluster analysis builds up a hierarchy of entities where algorithms can work either top-down or bottom-up. Bottom-up algorithms treat each entity as a singleton cluster at the outset and then successively merge (or agglomerate) pairs of clusters until all clusters have been merged into a single cluster that contains all entities. The decision of which pair of entities to merge next is taken based upon an updated distance

matrix of existing clusters/entities. Bottom-up hierarchical clustering is also called hierarchical agglomerative clustering and is the most common approach.

Results of an agglomerative clustering are typically represented by a dendrogram. Each merge is in the agglomeration procedure is represented by a horizontal line. The y-coordinate of the horizontal line is the similarity of the two clusters that were merged, where entities are viewed as singleton clusters. In effect a dendrogram provides a direct visual representation of the dataset at hand and allows identification of clusters readily by eye. Still, the results of cluster analysis have to be evaluated carefully since all cluster algorithms tend to cluster even data without any structure.

Hierarchical cluster analysis has a long history of application in biosciences (Kriventseva et al., 2001; Zhao and Karypis, 2005; Miller et al., 2008) and has been used to classify neurons based on electrophysiology and/or morphology (Cauli et al., 2000; Kozloski et al., 2001; Tsiola et al., 2003; Nowak et al., 2003; Krimer et al., 2005; Benavides-Piccione et al., 2006; Garrido-Sanabria et al., 2007; Chen et al., 2009; Helmstaedter et al., 2009a, 2009b, 2009c).

In particular the group of Yuste have used a combination of PCA and cluster analysis to classify neuron morphologies (Kozloski et al., 2001; Tsiola et al., 2003; Dumitriu et al., 2007). The current approach was inspired by these studies. In particular Dumitriu et al. (2007) performed a 3 step procedure. In order to remove redundant information they computed a correlation matrix on the original dataset and removed highly correlated ($r>0.8$, $p<0.05$) variables. Then PCA was used to identify relevant variables, performing PCA and extracting the factor loadings for each principal component. High load variables (>0.7) were then selected to perform cluster analysis in this reduced variable space. Starting with this procedure, I have compared different variations of the procedure and carefully evaluated the impact on cluster analysis results.

After transforming the database into z-scores, a correlation matrix was calculated and variables that correlated significantly ($r>0.8$, $p<0.05$) with one or more other variables were excluded. Secondly a principal component analysis was performed either on the previously reduced dataset or on the original dataset. Then cluster analysis was performed on the original (z-transformed) dataset, the manually de-correlated set, on the first 3 principal components from the original dataset and on the first 3 principal components of the de-correlated dataset. Clustering was performed by using Ward's method (Ward, 1963) using the Euclidean distances as similarity measure. At each stage of the agglomeration, the number of groups is reduced by one through merging two groups (or individuals) whose combination gives the least possible increase in the within-group sum of squared deviation. This is implemented through updating a temporary matrix of Euclidean distances between cluster centroids.

The cophenetic correlation coefficient was used to assess the quality of cluster analysis results (Rohlf and Fisher, 1968). The cophenetic correlation is computed as the correlation between the distances displayed in the dendrogram and the distances in the original dataset, thus quantifying how well a dendrogram represents the original data. With $x_{i,j} = |X_i - X_j|$, the Euclidean distance between the ith and jth observations (feature), and $t_{i,j}$ the dendrogrammatic distance between the points T_i and T_i, i.e. the height of the node at which these two points are first joined together, the cophenetic correlation coefficient c is given by:

$$c = \frac{\sum_{i<j}(x_{i,j} - \bar{x})(t_{i,j} - \bar{t})}{\sqrt{\left[\sum_{i<j}(x_{i,j} - \bar{x})^2\right]\left[\sum_{i<j}(t_{i,j} - \bar{t})^2\right]}}$$

Figure 3.11 shows the results of these 4 different approaches for the clustering of control condition electrophysiology variables (see Results). Each row in the figure depicts the result of one dataset, the first column showing the resulting dendrogram with the cophenetic correlation coefficient on the top left, the second column showing a scatter plot of the first two normalised principal components, and the third row depicting a bar plot showing explained variance of every component, including the cumulative sum (red line).

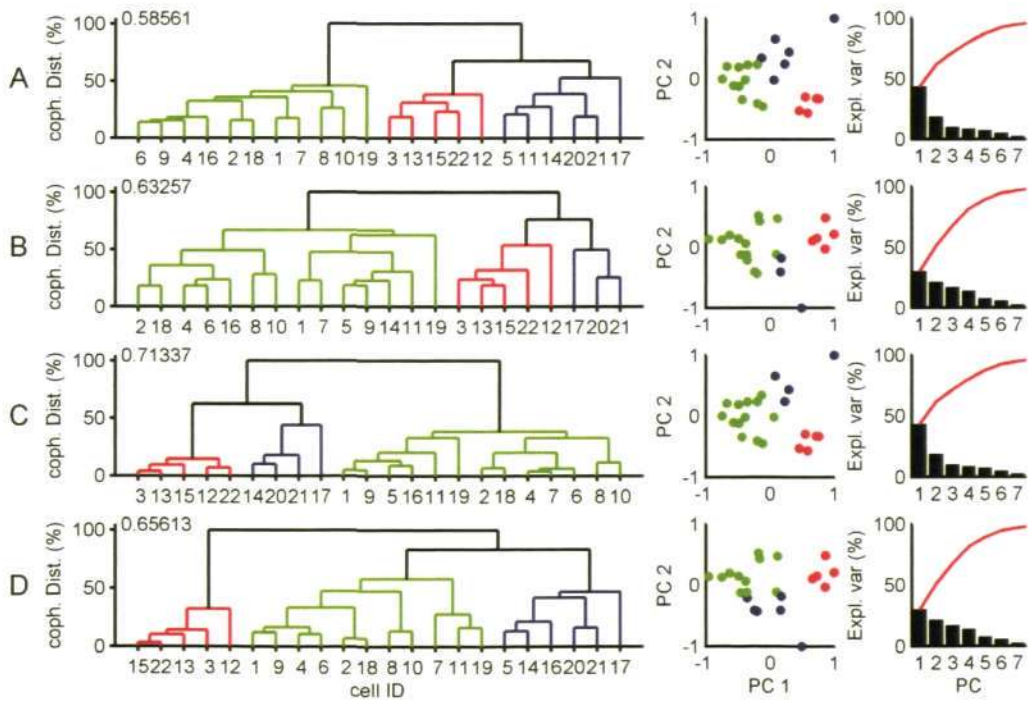

Figure 3.11 | Comparison of data preparation for cluster analysis
Inputs to the clustering were: A) Raw normalised of data, B) decorrelated data, C) principal components 1-3 or raw data, principal components 1-3 of the decorrelated dataset.

In row A the complete original dataset was fed into the cluster analysis, and a PCA on the original dataset was computed for comparison to the other results. In row B the manually de-correlated dataset was clustered and PCA was computed separately. In row C the first 3 principal components of the PCA from the full dataset were clustered. In row D the first 3 principal components of the manually de-correlated dataset were clustered. Here it seems that the direct clustering of principal components gives the highest correlation to the original dataset. Moreover, clusters seem to be more compact. Although the cluster assignment seems slightly counterintuitive in the scatter plot of principal components (C, 2nd column), the additional information in the 3rd principal component possibly adds to the distinction of cells. Based on this and on the fact that selecting highly correlated variables by hand imposes some sort of intentional bias to the dataset, I have settled for clustering the first 3 principal components. Support for this procedure comes from studies that have shown that PCA itself is related to clustering, and selects a subspace where the optimal clustering solution lies (Ding and He, 2004). It further increases the ratio between intra-cluster similarity and inter-cluster similarity and thus clustering in the reduced PCA space produces a more accurate solution than if the algorithm was run in the original feature space (Ding and He, 2004; Vempala and Wang, 2005; Andrews and Fox, 2007).

In the obtained results pair-wise significance between individual features of established clusters was assessed by one-way analysis of variance (ANOVA) or paired student t-tests.

4 Results

I have recorded 47 prefrontal deep layer pyramidal cells of which 22 cells retained a complete apical dendrite, as revealed by confocal imaging of Streptavidin-Alexa-488 Fluor stained cell morphologies. Only cells with intact morphology (especially intact apical dendrite) were included in the following analysis. All recordings were obtained while bath applying antagonists for all fast synaptic transmission receptors, AMPA-R, NMDA-R, $GABA_a$-R and $GABA_b$-R. All protocols were recorded under control conditions (only synaptic blocker), with added D2 agonist (quinpirole, 10 μM) or added D1 agonist (SKF 39383, 50 μM), in that order. In between pharmacological applications 5-10 minutes were allowed to washout a previous treatment and simultaneously wash-in a new application. Typical recordings lasted between 35 and 50 minutes. All data was tested for significant differences between obtained mean values of pharmacological conditions by independent sample t-test ($p=0.05$) or analysis of variance (ANOVA) with post-hoc Tukey-Kramer test.

Recorded cells are first analysed based on electrophysiological properties such as the passive membrane time constant, input resistance and various parameters quantifying firing properties established by injection of ramp and step protocols in current clamp and voltage clamp mode. These results are fed into a cluster analysis to identify systematic differences between intrinsic biophysical properties of pyramidal cells. These results are discussed in the light of previously conducted studies.

Next the analysis was extended to include dopaminergic modulation of biophysical properties. First I present an overall account for effects of dopamine receptor specific agonists by calculating mean effects over the whole dataset. Then dopaminergic effects are analysed based on cell type classification established in the previous chapter. Also, a cluster analysis including all dopaminergic parameters is performed. The resulting cluster properties will be analysed in more detail and compared to previously reported effects.

I present the results from imaging, digital reconstruction of morphology and quantitative morphometric analysis of recorded pyramidal cells. These results are fed into a separate cluster analysis to identify quantitative morphological differences between deep layer pyramidal cells.

Finally, I compare electrophysiological and morphological cluster and discuss the results in light of previous studies on biophysical and morphological properties of pyramidal cells in the rat PFC and will infer implications for computational properties of single cells and networks.

4.1 Classifying prefrontal pyramidal cells based on intrinsic properties

Nineteen variables calculated from raw electrophysiology data served as a database for hierarchical cluster analysis. Cells were clustered solely based on their intrinsic properties in control condition, i.e. all fast synaptic transmission blocked. The final result of the cluster analysis is visualised in Figure 4.1. A dendrogram (Figure 4.1, top) shows the result of clustering the first 3 principal components of the dataset using Ward's method with Euclidean distance matrix. Every leg at the bottom of the dendrogram represents a single cell. The bottom left of Figure 4.1 depicts the z-scores of all 19 variables that entered the analysis in a box and whisker plot. This is a convenient way to visualise basic statistical properties of a dataset by plotting the smallest observation within the 1.5 interquartile distance (whisker left), lower quartile (left end of the box), median (red line), upper quartile (right end of the box), and largest observation within the 1.5 interquartile distance (whisker left). All values outside the upper or lower 1.5 interquartile distances are plotted as red crosses and might be possible outliers. Variables have been sorted by their respective median value in the first cluster (dark blue). The bottom right of Figure 4.1 depicts a colour coded matrix of all z-scores (data matrix) sorted by the results of the cluster analysis, where values in each row of the matrix correspond to the variable in the neighbouring box plot and every column corresponds to results from a single cell, sorted according to the dendrogram above.

Here one can see 3 distinct clusters present in the dataset, as marked by different shades of blue in the dendrogram. There is a small cluster of 5 cells (dark blue) which is very compact has only small within cluster distances. As seen in the data matrix the cluster seems to separate well from neighbouring clusters. Figure 4.2 shows the firing patterns of cells in response to a brief suprathreshold current step grouped according to cluster membership. Here it becomes obvious that this cluster contains cells displaying burst firing and a strong AHP. Cells within this cluster will be referred to as intrinsically bursting (IB).

The second cluster (medium blue) is also small (n=4) but has rather large intracluster distances indicating a less homogenous group of cells. Indeed when inspecting the data matrix, it seems that only a few variables in these cells are strongly correlated (horizontal patterns in the matrix indicate a strong correlation). Those are the minimum slope [*I-V: min(dI/dV)*] and the bump deepness of the voltage clamp V-I curve [*I-V: bump*] and the reversal potential [*E(rev)*]. These variables are very distinct when compared to the other clusters. Other variables (especially in the top rows of the data matrix) seem to lay in between values of the first (IB) and the third cluster (see below). This cluster will be referred to as intermediate (IM).

Here it has to be noted that cell #17 displayed rather extreme values in a few measurements, for example no spikes were elicited during short current steps, but behaved within range for other measures; hence the cell was included into the analysis. A separate cluster analysis without cell #17 yielded the same grouping of cells (data not shown).

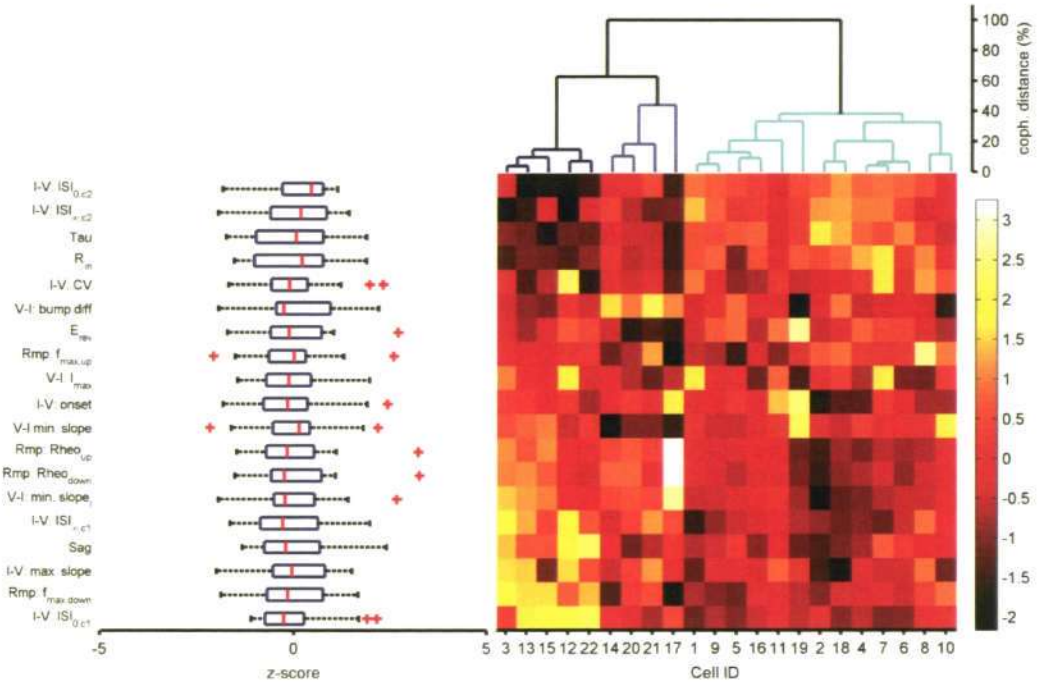

Figure 4.1 | Cluster analysis of electrophysiology variables from control condition
Top) Dendrogram of linkages obtained by Ward's method based on Euclidean distances between z-scores of all cell variables. Left) Box plot of z-score transformed variables. Right) Matrix of z-scores sorted according to the dendrogram.

The third cluster is the largest (n=13). Cells in this cluster seem to be quite opposite in most parameters compared to IB cells, as easily seen in the data matrix. When examining the firing pattern of cells in this cluster most cells display regular spiking (RS), although some cells display initial doublet spikes (#'s 8,10,11).

The factor loadings of the principal components fed into the clustering indicate which variables contribute to the differentiation of cells. The factor loadings represent the relative contribution of each variable to the respective principal component. Figure 4.3 summarises the results of the PCA. A biplot (Figure 4.3 A) shows individual cells (dots) in the axes spanned by the first 2 principal components and coloured by their cluster membership. Moreover, the contributions of single variables to the principal components are indicated by vectors, where length and direction are proportional to the factor loading in each principal component. Each vector is colour coded

by their contribution to the first principal component. A scree plot indicates the contribution of each principal component to the total variance in the dataset (Figure 4.3 B).

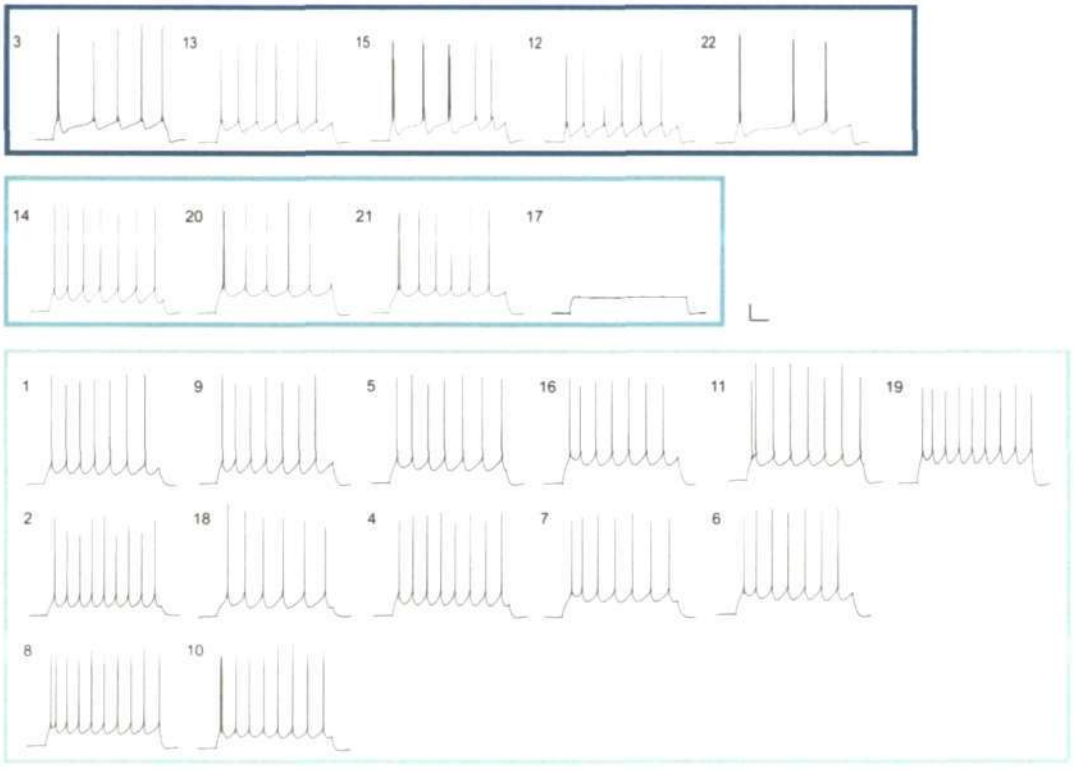

Figure 4.2 | Firing patterns grouped into cluster
Cells in the IB cluster (dark blue, top), display repetitive burst and strong AHP, where as cell in the IM (medium blue, middle) and RS cluster (light blue, bottom) display regular spiking patterns. Notice that cells #20, 21, 11, 8 and 10 display an initial doublet of spikes.

The first principal component explains about 43 % of the total variance, whereas PCs 1-3 sum up to 71.5% of the total variance. The contribution of each variable to PC1 is presented in Figure 4.3 C. Here, variables with the highest magnitude (either positive of negative) contribute most to the explained variability. For the positive half of PC1 these are notably passive properties, the estimated membrane time constant [*Tau*] and the input resistance [*R(in*], but also the second coefficients of the square root fit for spike latency [$b(ISI_0)$] and steady state [$b(ISI_\infty)$]. The current at the minimum slope of the voltage clamp I-V curve [*I(min(dV/dI))*], the first coefficient of the square root fit for spike latency [$a(ISI_0)$] and the rheobase currents for both upward and downward current ramp injection [*Rmp (u): rheobase, Rmp(d): rheobase*]. contribute most to the negative half of PC1. The PCA effectively groups correlated variables into the same PC, thus vectors in the same quadrant indicate groups of variables with similar covariance that distinguish cells.

This becomes evident when performing separate ANOVAs on every variable, using cluster membership as independent variable. Table 4.1 presents the result of separate unbalanced one-way ANOVAs including a posthoc Tukey-Kramer test.

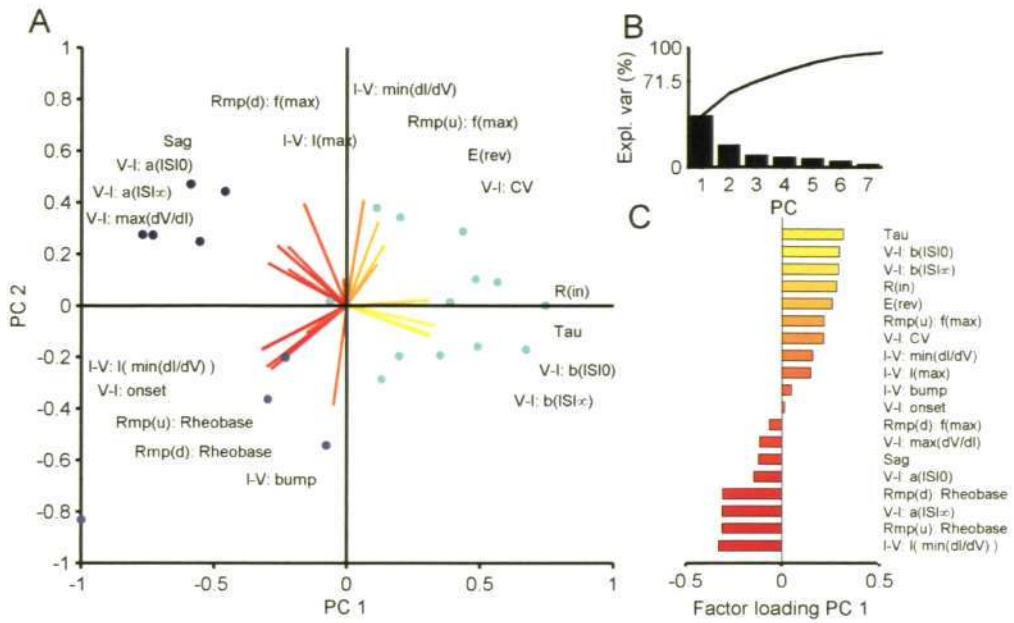

Figure 4.3 | Summary of PCA results
A) Scatter plot of cell positions (dots) within the coordinate system spanned by the first 2 PCs, cell are coloured according to the dendrogram in Figure 4.1. Factor loading of variables is indicated by coloured vectors according to C. B) Scree plot of PCs. PC1-3 explain 71.5% of the total variance in the dataset. C) Bar plot of factor loading for variables to the first PC.

Indeed 10 variables show highly significant effects of cluster membership. The highest significance *(p<10-5)* is displayed for the square root fit to spike latency [*a,b(ISI0)*] and the passive variable [*Tau*]. Slightly lower significant effects (p<10-4) are seen for [*R(in)*], the sag current [*sag*], the square root fit to steady state ISI [*a,b(ISI∞)*], for maximum firing rate of a downward ramp [*Rmp(d): max(f)*], the current level at the minimum slope of the voltage clamp I-V curve, [*I-V: I(min(dI/dV))*] and the upward current ramp rheobase [*Rmp(u): rheobase*]. Moreover, the resting potential, [*E(rev)*], the downward rheobase [*Rmp(d): rheobase*], the minimum slope [*I-V: min(dI/dV)*] and the bump deepness [*I-V: bump*] of the voltage clamp I-V curve show highly significant p values (p<0.01). This shows highly significant differences between the established physiological subpopulations, despite the relative low numbers of cells per cluster. Also, this indicates that the change in spike latency in response to a series of simple current steps is highly indicative of the cell type at hand and could be used for fast online determination of pyramidal cell type.

Table 4.1 Mean cluster properties

	Cluster			ANOVA	
	IB (n=5)	IM (n=4)	RS (n=13)	F(2,19)	p
V-I: a(ISI0)	7.03 ±1.14 •	4.20 ±0.82	3.39 ±0.73 ▲	28.34	0.000002
V-I: b(ISI0)	-69.38 ±11.60 •	-45.91 ±14.86 ■	-27.50 ±7.09 ▲	27.87	0.000002
Tau	16.26 ±1.93	20.32 ±3.76 ■	30.03 ±4.20 ▲	24.91	0.000005
R(in)	57.67 ±4.95	70.70 ±14.87 ■	99.10 ±16.10 ▲	15.48	0.0001
V-I: b(ISI∞)	-24.54 ±7.09	-19.13 ±5.42 ■	-8.63 ±4.70 ▲	14.98	0.0001
Sag	0.34 ±0.08 •	0.12 ±0.07	0.11 ±0.08 ▲	14.77	0.0001
V-I: a(ISI∞)	2.24 ±0.42	1.73 ±0.40 ■	1.00 ±0.43 ▲	14.68	0.0001
Rmp(d): max(f)	150.75 ±14.40 •	61.92 ±48.06	72.47 ±24.14 ▲	13.59	0.0002
I-V: I(min(dI/dV))	129.25 ±27.32	146.93 ±38.30 ■	75.03 ±22.06 ▲	12.64	0.0003
Rmp(u): Rheobase	138.29 ±24.58	169.91 ±53.07 ■	86.64 ±19.13 ▲	12.56	0.0003
I-V: bump	5.64 ±6.90 •	37.17 ±7.65 ■	9.31 ±12.82	10.12	0.001
Rmp(d): Rheobase	158.60 ±24.30	188.96 ±48.72 ■	120.04 ±16.67	9.74	0.001
I-V: min(dI/dV)	-1.01 ±1.40 •	-5.94 ±1.21 ■	-1.42 ±2.06	9.51	0.001
E(rev)	-59.60 ±2.03	-64.16 ±1.78 ■	-58.08 ±3.22	6.4	0.007
V-I: max(dV/dI)	0.16 ±0.05	0.13 ±0.03	0.10 ±0.04	3.35	0.056
I-V: max(I)	1146 ±271	792 ±116	992 ±314	1.55	0.24
V-I: CV	0.16 ±0.11	0.14 ±0.04	0.20 ±0.06	1.03	0.38
Rmp(u): max(f)	13.96 ±0.68	11.58 ±4.50	14.57 ±3.65	1.02	0.38
V-I: onset	135.21 ±21.14	157.00 ±39.92	126.56 ±51.90	0.62	0.54

Unequal sample size ANOVA with post hoc Tukey-Kramer test:
• IB vs. IM, ■ IM vs. RS, ▲RS vs. IB

In order to distinguish RS and IM cells the most informative parameters are [*Tau*], [*R(in)*] and the steady state measures [$a(ISI_\infty)$, $b(ISI_\infty)$], whereas for the distinction of IB cells one would mostly rely on the presence of a sag current [*sag*], and parameters from the voltage clamp I-V curve, in particular [*I-V: bump*].

To evaluate the impact of single variables on the clustering results I have performed a "leave-one-out"-type analysis. By performing the same analysis routine on a dataset where selected variables have been excluded, one can infer the robustness of the obtained cluster solutions.

I have selected 5 variables that were, based on the results from the ANOVA, either significantly different between all cell groups [*V-I:* $b(ISI_0)$], significantly different between IB and RS cells

[*Sag*], significantly different between IM and RS cells [*I-V: I(min(dI/dV))*], significantly different between IM and IB cells [*I-V: bump*], or not significantly different between groups [*Rmp(u): max(f)*].

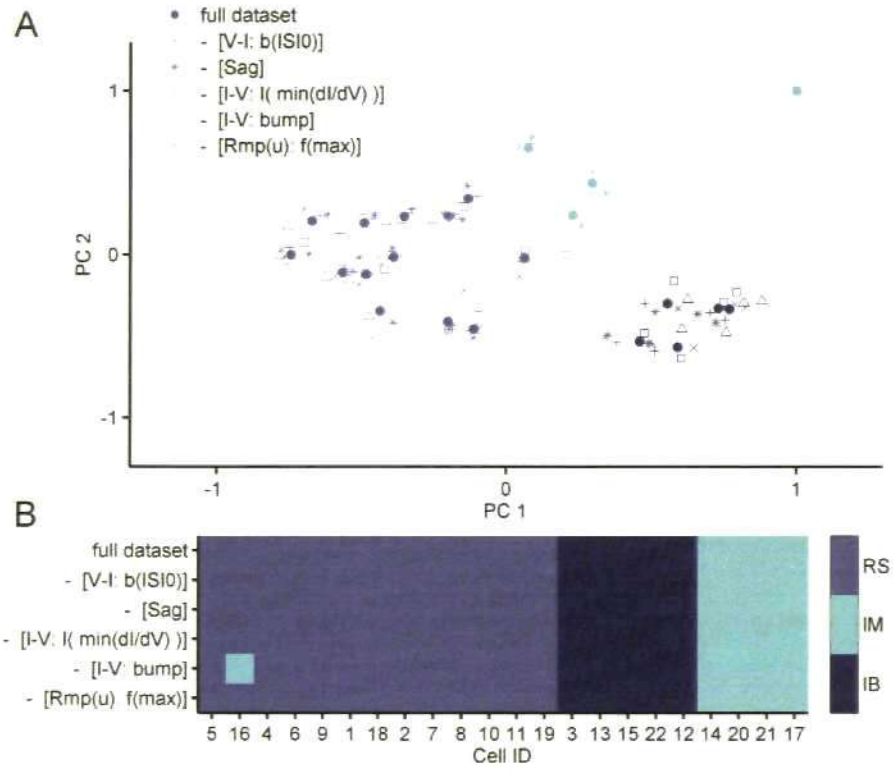

Figure 4.4 | Leave-one-out analysis
A) Cell positions in principal component axes and results of repeated HCAs (indicated by color) with the full dataset (full circles) and datasets without selected variables (see text for details. B) Comparison of cluster solutions from reduced datasets to full dataset. Colour codes are same as in Figure 4.3.

Each of these selected variables was removed from the dataset, and the reduced dataset subjected to the very same routine of PCA/HCA, as described above. The results were then compared to the results obtained with the full dataset. Figure 4.4 shows the cluster results obtained for different reduced datasets. Overall the cluster results are very robust against deletion of single variables from the dataset. All obtained cluster solutions occupy a narrowly defined area in a scatter plot of cells in principal components (Figure 4.4A) and are very similar to the solution obtained using the full dataset. I plotted the cluster membership for each cell in each cluster solution in a colour coded table (Figure 4.4B). Here it becomes obvious that all solutions, apart from one are indeed identical. Only when removing [*I-V: bump*] is one cell, otherwise classified as RS cell, included in the IM cluster. Since [*I-V: bump*] is one of the most characteristic variables for IM cells, this seems to reduce the distance between the centre of

mass of the IM cluster and that particular RS cell (ID#16), so that it gets included into the IM cell cluster. On the one hand, this shows that IM cells are closer to RS cells in their intrinsic parameter set, as can be readily seen by their distance to the RS cluster compared to the IB cluster. Moreover, since the number of IM cells is quite small, one can raise reasonable doubt whether IM cells do indeed form a separate cluster or are instead just extreme variants of RS-like cells. The current analysis suggests that IM cells do have particular properties that distinguish them well from RS cells (i.e. the rather large "bump" in the steady state voltage clamp IV curve), but only a larger database of recorded cells could provide final evidence.

In summary, RS type cells show higher mean membrane time constant [*Tau* = 30.03 ±4.20 ms], a lower sag current indicator [*sag* = 0.11 ±0.08 mV] and a higher mean input resistance, [*R(in)* = 99.10 ±16.10 MΩ].

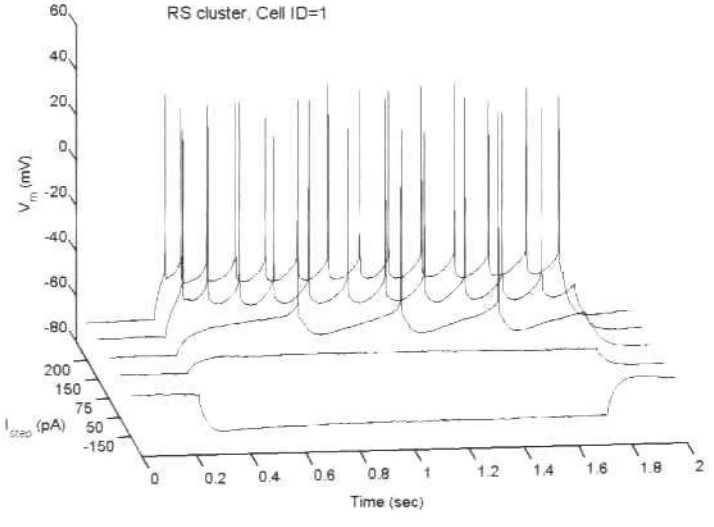

Figure 4.5 | Raw membrane voltage traces for an example RS cell (ID#1).

Notice the long spike latency for the low intensity step as quantified by the variables $a(1/ISI_0)$, and $b(1/ISI_0)$.

Figure 4.5 shows raw membrane voltage traces from selected brief (1.5 s) current step injections in one from the RS cluster. Here no bursting is observed, the cell emits only single spikes, a classic RS cell. In these cells the current value at the inflection point for the voltage clamp V-I curve is lower, with a mean of [*I-V: I(min(dI/dV))* =75.03 ±22.06 pA]. For both ramp injections, increasing and decreasing, rheobase currents were lower with means of [*Rmp(u): Rheobase* = 86.64 ±19.13 pA] and [*Rmp(d): Rheobase* 120.04 ±16.67 pA], respectively. Also, the maximal instantaneous firing rate evoked by a decreasing ramp was on average lower [*Rmp(d): max(f)* = 72.47 ±24.14 Hz]. When looking at measures extracted from the long current step injection, RS cells showed lower coefficients [$a(ISI_0)$ = 3.39 ±0.73, $a(ISI_\infty)$ = 1.00 ±0.43], but higher values for the y-axis intercept [$b(ISI_0)$ = -27.50 ±7.09, $b(ISI_\infty)$ = -8.63 ±4.70]. These values indicate a flatter fit to the ISI curve over different current steps, i.e. cells exhibit a smaller range of firing frequencies.

In contrast, IB cells seem to have mostly opposite properties to RS cells. Figure 4.6 shows raw voltage membrane traces in response to selected brief current step stimulation from an example IB cell. Notice the repetitive bursting at lower stimulation intensities, whereas regular spiking occurs after an initial burst at high stimulation intensities. Here the strong after depolarisation (ADP), on top of which additional spikes during a burst occur, is clearly visible. Also, these cells display rather strong after-hyperpolarisation (AHP) in between bursts, when compared to RS cells (Figure 4.5). Cells in the IB cluster have a lower membrane time constant [*Tau* =16.26 ±1.93 ms], a higher sag component [*Sag* = 0.34 ±0.08 mV] but a lower input resistance [*R(in)* = 57.67 ±4.95 MΩ]. In terms of excitability IB cells exhibit a shallower V-I curve [*I-V: bump*= 5.64 ±6.90 pA] and the curve is shifted slightly to higher currents [*I-V: I(min(dI/dV))* = 129.25 ±27.32 pA] compared to RS cells. They have higher rheobase currents [*Rmp (u): rheobase* = 138.29 ±24.58 pA], but the maximum instantaneous firing rate obtained from a decreasing ramp protocol is much higher [*Rmp(u): max (f)* = 150.75 ±14.40 Hz], which is a reflection of burst firing. Furthermore, bursting cells show higher coefficients but lower y-intercepts for both spike latency [*V-I: a(ISI$_0$)*=7.03 ±1.14, *V-I: b(ISI$_0$)*=-69.38 ±11.60], and steady state FR [*V-I: a(ISI∞)* = 2.24 ±0.42, *V-I: b(ISI∞)* = -24.54 ±7.09], which is opposite to cells in the RS cluster.

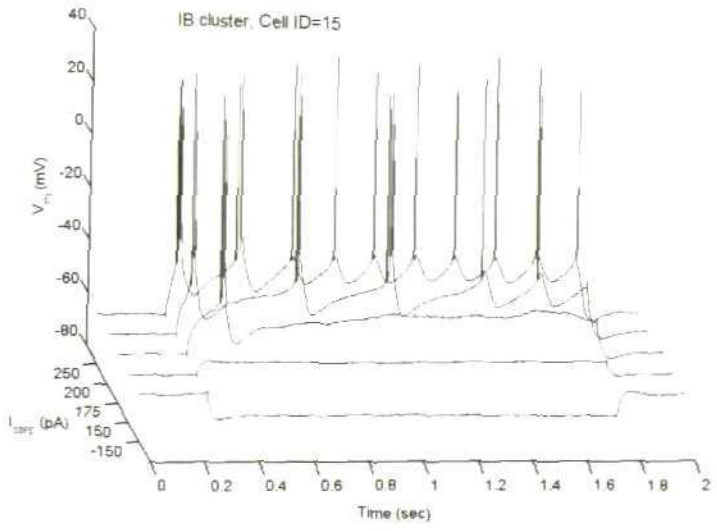

Figure 4.6 | Raw membrane voltage traces for an example IB cell (ID#15).

Notice the repeated occurrences of bursts at the 175 pA current step. Also, the first spike (burst) occurs at much higher stimulus intensities (as quantified by the rheobase current), when compared to RS cells.

Cells in the 3rd cluster seem to have properties of both RS and IB cells and hence have been termed intermediate (IM). Figure 4.7 shows raw voltage membrane traces in response to selected brief current step stimulation from an example IM cell. This particular cell responds with an initial spike doublet to current step stimulation, but then switches into repetitive single spike firing mode. Not all IM cells show the initial doublet, and some cells in the RS cluster show an initial doublet as well. IM cells have literally intermediate values for certain parameters, i.e. for mean membrane time constant [*Tau* = 20.32 ±3.76 ms], input resistance

[*R(in)* = 70.70 ±14.87 MΩ], and for the coefficient and y-intercept of root square fits to spike latency [$a(ISI_0)$ = 4.20 ±0.82, $b(ISI_0)$ = -45.91 ±14.86] and steady state FR [$a(ISI_\infty)$ = 1.73 ±0.40, $b(ISI_\infty)$ = -19.13 ±5.42]. Interestingly, for other parameters these cells seem to be either more IB-like or more RS-like. The sag component has a similar low value as in RS cells [*sag* = 0.12 ±0.07 mV], but rheobase currents are on average higher than those for bursting cells [*Rmp(u): rheobase* = 169.91 ±53.07 pA; *Rmp(d): rheobase* = 188.96 ±48.72 pA] and maximum firing rates during ramps are lower than for RS cells [*Rmp(d): max(f)* = 61.92 ±48.06 Hz]. In their voltage clamp I-V curve these cells have a very pronounced kink [*I-V: bump* = 29.03 ±12.10 mV], but the curve is shifted to higher current values [I-V: *I(min(dI/dV))* = 146.93 ±38.30 pA].

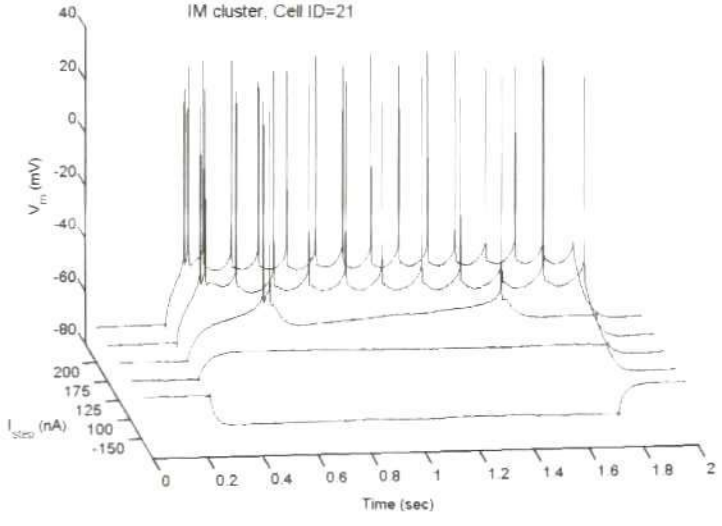

Figure 4.7 | Raw membrane voltage traces for an example IM cell (ID#21).

Note the initial doublet in response to step stimulation. This cell shows a small ADP, little AHP and very regular spiking after the initial spike doublet.

Input –output functions of established cell groups

These significant differences reflect how cells in different cluster respond to input. Figure 4.8 shows the mean input-output functions for each cluster derived for 3 different stimulation protocols probing excitability, i.e. current ramps, voltage clamp steps and long current steps, where each protocol presents different aspects of input-output relations. For the voltage clamp steps the mean I-V curves summarise behaviour of the total membrane current at different voltages on a relatively long time scale (800-1000 ms), which is well in the steady state for most intrinsic membrane conductances (Figure 4.8 A). RS cells have a less steep sub-zero I-V relation; the curve is more N-shaped and reaches smaller total membrane currents. In contrast, IB cells have steeper sub zero I-V relation, the curve is less N-shaped, greater total membrane currents are reached, the upper part of the curve, above the zero crossing, is shifted towards higher currents compared to RS cells. IM cells have an intermediate sub-zero I-V relation, with

a very strong N-shape. Their curve is more IB-like near threshold, but reaches smaller total membrane currents (RS-like).

For both upward and downward ramp injection (Figure 4.8 B1, B2), the firing rate was binned over 0.5 second bins (9 seconds in total) and plotted against the average current during ramp injection (for ease of readability the current axis for the downward ramp was reversed in B1). For RS cells this ramp f-I curve had a lower onset (rheobase) and was shifted towards lower currents compared to IB and IM cells. Also, RS cell achieve higher average firing rates compared to IB cells in this protocol (as opposed to the instantaneous firing rates discussed above). IB and IM cells have a higher onset (rheobase), where IB cells reach higher firing rates during strong stimulation compared to IM cells.

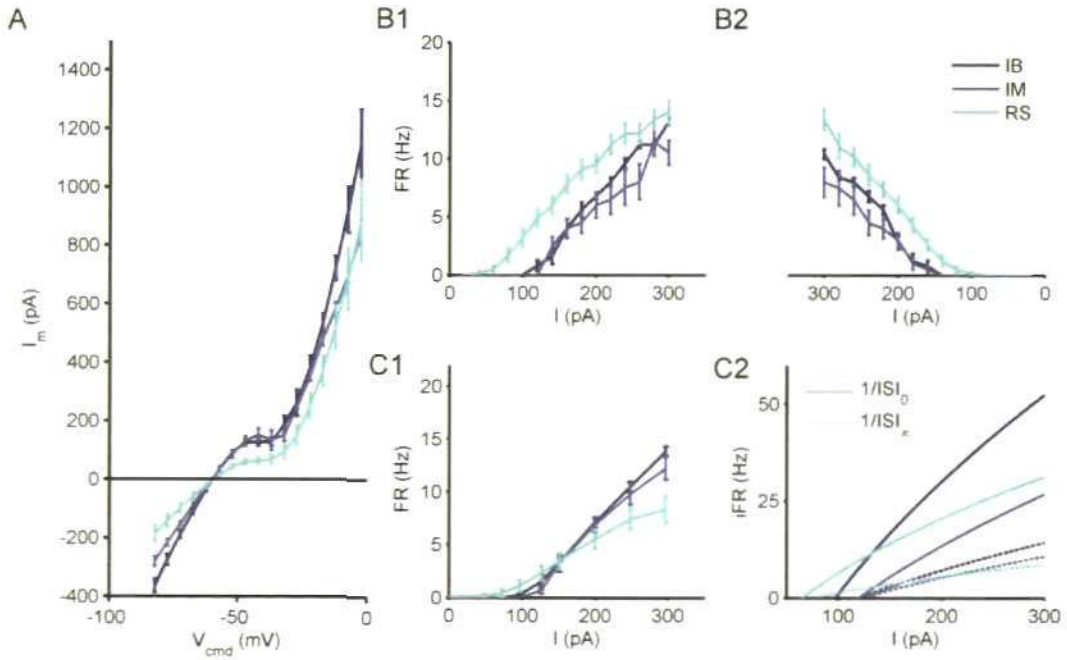

Figure 4.8 | Average input-output functions for each cluster
A) Mean voltage clamp I-V curves. B) Mean f-I curves for upward (B1) and downward (B2) ramp injection. Note the reversed x-axis in B2. C) Steady state f-I curves (C1) and mean square root fit to $1/ISI_0$ and $1/ISI_\infty$ (C2) from long current step stimulation. Error bars indicate SEM.

The steady state f-I curve based on long current injections (Figure 4.8 C1) points to differences in the steady state behaviour of the cell groups. IB cells have a similar ramp f-I curve, a higher onset of the f-I curve and a higher slope (gain). In contrast, RS type cells have lower onset, IM cells behave more IB-like for low intensity input, but might have slightly lower gain.

The mean square root fits to 1/ISI for different input strengths illustrate both transient ($1/ISI_0$) and steady state ($1/ISI_\infty$) output (Figure 4.8 C2). This is mainly useful for depicting the degree of accommodation. Here IB cells fire a fast action potential in fast response to (relatively strong)

incoming input (lower spike latency) and show higher firing rates in the steady state as shown in the steady state f-I curve. On first view IB cells seem to show large accommodation from very high to rather low firing rates in steady state, but analysis of the second and third ISI (Figure 4.9) shows that the following ISIs are very close to the steady state response, hence IB cells show little or no accommodation. Indeed, consecutive ISI are shorter compared to previous ones, that is, later spikes fire at a higher frequency than earlier ones. Compared to IB cells, spiking of RS cells occupies a wide range of frequencies, mainly due to varying levels of accommodation. 1/ISI curves are distributed evenly, with stronger accommodation after the initial spike. The response to input is much slower in RS cells (probably due to a slowly inactivating potassium current I_A), but are more sensitive to weak input. IM cells need stronger inputs, but seem to display moderate but fast accommodation.

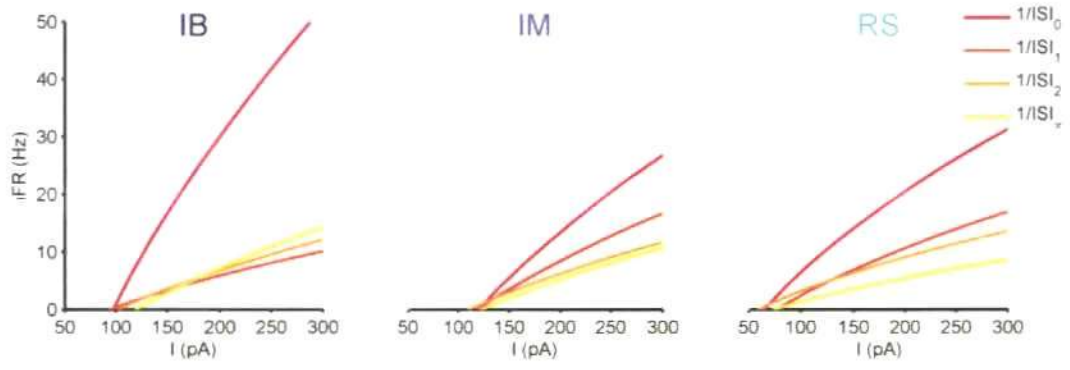

Figure 4.9 | Average square root fit for each cluster
Mean square root fits for 1/ISI0,1,2, ∞, for long current step stimulation. Note the increase in iFR towards the steady state in IB cells.

Discussion

In conclusion the current analysis identified 3 distinct cluster of deep layer pyramidal cell in a parameter space spanned by intrinsic biophysical properties. These cluster are in good agreement with previously reported 'cell types' in the rat PFC (Kawaguchi, 1993; Yang et al., 1996; Degenetais et al., 2002; Morishima and Kawaguchi, 2006; Otsuka and Kawaguchi, 2008) and other cortical areas (Connors et al., 1982; McCormick et al., 1985; Connors and Gutnick, 1990; Larkman and Mason, 1990).

One of the earliest accounts of discrete cell types in the PFC comes from Kawaguchi (1993). They differentiated deep layer pyramidal cells into a high and a low input resistance group. The low resistance group seemed to display initial bursts but also moderate firing rate adaptation, whereas the high input resistance group showed fast adaptation. They did not report intrinsically bursting cells, as reported in other cortical areas at the time (Connors et al., 1982; McCormick et

al., 1985; Connors and Gutnick, 1990), but this might be due to recording in slices from young rats (P<26) and recording at room temperature.

In contrast, Yang et al. (1996) observed bursting cells in rat prefrontal slices. In fact they stated IB cells were the main type of pyramidal cells in the rat PFC. This could be partially explained by differences in recording techniques ('sharp' intracellular recording at 34° C), but more importantly they used different criteria for defining RS and IB cells. Their RS cells are very fast adapting, showing a strong fast AHP, and sodium dependent subthreshold oscillations. Their IB cells made up 64% of all recorded neurons and displayed an initial spike doublet but then changed into a regular spiking pattern (sometimes referred to as phasic-tonic firing cells). The key feature they used to distinguish IB cell from RS cells was a calcium dependent depolarising afterpotential (DAP or ADP). Interestingly, these IB cells had a similar input resistance and membrane time constant compared to their 'RS' cells. They also described one other cell type, rhythmic oscillatory bursting cells (ROB), which fired repeated bursts to low intensity stimulation but changed to initial burst and regular firing at higher intensities. These cells had significantly lower input resistance and a very strong sag component.

Recently Otsuka and Kawaguchi (2008) classified cells as either slowly adapting, slowly adapting with a spike doublet or as fast adapting. They did not report any bursting cells, which could be due to recording at 30°C.

An intracellular recording study performed in anaesthetised animals *in vivo* (Degenetais et al., 2002) has adopted a similar scheme to classify prefrontal deep layer pyramidal cells. They divide RS cells into slow adapting RS and fast adapting RS and together these made up 70% of recorded cells. Slow adapting cells are further divided into cells with doublet and without, where cells with doublets showed no adaptation during steady state firing. RS cells without a doublet showed no ADP but adaptation well beyond the initial 2-3 spikes. Their IB cells have low input resistance, strong ADP and strong medium AHP (similar to non-inactivating bursting cells in Connors et al., 1982). They displayed multiple bursts upon low intensity stimulation but RS-like pattern for strong stimulation.

In relation to these previous studies the results of the current analysis confirm these qualitative reports. The RS cluster in the current analysis correlates to the high input resistance group of Kawaguchi (1993), the RS and IB type of Yang et al. (1996), and to the RS type of Degenetais et al. (2002). The IB cluster of the current analysis relates to the low input resistance of Kawaguchi (1993), the ROB type of Yang et al. (1996) and the IB type of Degenetais (2002). Indeed the current analysis suggests that doublet firing and non-doublet firing cells are very much alike in terms of intrinsic properties, as they were not distinguished into distinct cluster; hence the nomenclature of Degenetais et al. seems more appropriate and has been adopted here.

All these studies have reported qualitative morphological properties in addition to physiology; these will be discussed in the context of the results presented in the following chapters. IM cells might form a distinct third cluster. Yang et al. (1996) have also described IM type cells in prefrontal slices. They constituted only 4% of recorded cells, and their intrinsic properties were reported to be inbetween RS and IB cells, very much like the IM cells described in the current study.

The emphasis in the current analysis lies less on actual firing patterns, as these can be influenced by a variety of factors (Steriade, 2004), but more on capturing a wide range of intrinsic parameters and also functional input-output relationships. For example, there is good evidence for dendritic input promoting bursting in all types of pyramidal cells, especially through a combination of back propagating action potentials and evoked dendritic calcium plateaus (Larkum et al., 1999, 2001; Williams and Stuart, 1999).

To this end, I have focussed on the difference in intrinsic properties as measured from a variety of stimulation protocols. These differences in intrinsic properties manifest as differences in input-output functions of the obtained cell classes. RS cells respond to smaller inputs (lower rheobase) but can reach high firing rates upon ramp stimulation. In steady state they reach much lower firing rates compared to bursting cells, enabling them to encode a wider range of input strengths (at low input intensities). In opposition, IB cells need stronger input to be activated (higher rheobase) but can maintain much higher firing rates in their steady state.

One interesting effect seen in the input-output functions is hysteresis of firing rate changes, when comparing upward and downward current ramp injections (Figure 4.8 B). Hysteresis means that identical current levels during an upward ramp result in higher firing rates than during downward ramp stimulation. This can be easily seen in the rheobase: rheobase currents for upward ramps are always smaller than rheobase currents for downward ramp injection. This hysteresis has been observed in all cell types and is most likely due to inactivated sodium currents after initial strong stimulation during the downward ramp. Here hysteresis is clockwise, as described in pyramidal cells before (Calvin and Sypert, 1976) as opposed to counter-clockwise hysteresis in firing rate seen in alpha-motor neurons (Hounsgaard et al., 1988). The implications of this hysteresis on information processing in cortical neurons have received little attention so far. The transition from resting to spiking and vice versa indicate dynamical properties of neurons (Izhikevich, 2007), but this would need further investigation and is beyond the current study.

Only a few studies systematically investigated the influence of intrinsic properties on input-output functions of cortical pyramidal cells. One apparent difference between IB and RS cells is the increased adaptation found in RS cells. Adaptation has been studied extensively through

experimental and theoretical work to determine its importance for neural coding. It has been suggested to implement temporal masking of subsequent stimuli (Wang, 1998), may correlate to contrast adaptation in the visual cortex (Sanchez-Vives et al., 2000), remove temporal correlations from input streams (Wang et al., 2003), implement a high pass filter (Benda et al., 2005) or stabilise network oscillations (Crook et al., 1998; Fuhrmann et al., 2002).

One recent study by Prescott and Sejnowski (2008) examined how different types of adaptation influence coding mechanisms in pyramidal cells. They found that adaptation induced by a low threshold activated persistent potassium current (I_M) enhances the firing of independent, reliable single spikes in a close-to-threshold regime. Hence the combination of subthreshold oscillations and specific adaptation mechanisms might provide RS cells with the possibility to resonate with ongoing population oscillations, but also to encode information by reliable spike patterns rather than mean firing rates, as implicated by integrate-and-fire models (La Camera et al., 2008).

Another recent study investigated the influence of slow AHP on the input-output function of cortical cells (Higgs et al., 2006). They demonstrated that the amount of slow AHP in pyramidal cells determines the gain modulation seen through synaptic noise. Pyramidal cells with strong adaptation are more susceptible to gain increase through increased synaptic noise than non-adapting cells. Thus RS cells in this study (showing greater adaptation) are more likely to be gain modulated by synaptic inputs than IB cells (with little adaption). Since non-adapting cells are less prone to gain changes through synaptic noise they might be better suited for temporal integration, whereas adapting pyramidal cells change from integration to differentiation of inputs with increasing synaptic noise (Higgs et al., 2006).

Influence of in vivo like conditions

Since all data in this study was collected with synaptic transmission blocked, one key question is how these cell types react to incoming input, when faced with constant background synaptic bombardment found *in vivo*. Background synaptic activity puts single neurons into a 'high-conductance state' that profoundly differs from the *in vitro* situation (Destexhe et al., 2003). Various studies have examined the influence of synaptic input on input-output relationships, with sometimes conflicting results. Dendritic input has been shown to both increase (Fellous et al., 2003; Larkum et al., 2004) and decrease Chance et al. (2002) the gain of input-output functions. For example Chance et al. (2002) used dynamic clamp as an *in vitro* model of *in vivo*-like synaptic input, and found a gain reduction (reducing the slope of the f-I curve) in somatosensory cortical neurons through increased variance in balanced excitatory-inhibitory background noise. In contrast, Fellous et al. (2003) used a similar approach in prefrontal areas and observed a gain increase through variance. Interestingly, the f-I curves differed between the

two areas, Fellous et al. found a more sigmoid input-output function (much like the RS function observed in this study) compared to a more steeper, more second-order polynomial f-I curve that included a 'hard threshold' observed by Chance et al., which might point to differences in excitability seen here between RS and IB cells.

It would be interesting to repeat similar *in vitro* experiments for both RS and IB cells and see how they differ in integrating inputs under these *in vivo* like conditions. Surprisingly few studies have addressed pyramidal cell type (bursting v regular spiking) specific integration of synaptic inputs. One notable exception is a recent study by Otte et al. (2010), where cell type specific response to gamma frequency input was investigated *in vitro*. They have found a striking difference in sensitivity to oscillatory input between bursting and non-bursting deep layer pyramidal cells in the somatosensory cortex of mice. Regular spiking neurons show a strong increase in firing rate when somatic stimulation contains larger amplitude sinusoidal components, whereas bursting cells are largely insensitive to change in sinusoidal input amplitude variations. Yet, through increasing synaptic noise in the stimulation, bursting cells can be pushed into a regime where their output rates faithfully reflect the level synchrony in received input (i.e. the amplitude of the sinusoidal input component).

This demonstrates that the interplay of intrinsic biophysical properties and synaptic input critically shape input-output functions of pyramidal cells. Indeed the modifications of input-output functions can be used to implement complex computational operations. Gain shifts along the input strength axis can implement subtractive and additive computations, whereas gain increase or decrease can implement multiplicative/divisive computations (Silver, 2010). A recent study showed how manipulation of input-output functions in cortical networks can be exploited to implement stimulus discrimination during working memory. Through stimulus dependent shaping of input-output functions of neuronal populations, Machens et al. (2005) implemented a single network model that can both maintain working memory and compare stimulus properties by entering a 'line attractor' state. This line attractor critically depends on the similarity between input-output function of different encoding populations. Since input-output functions can be readily modulated through intrinsic plasticity (Cudmore and Turrigiano, 2004), synaptic inputs (Chance et al., 2002; Fellous et al., 2003; Higgs et al., 2006) and neuromodulation (see below), a dynamic task dependent modulation of input-output functions is well conceivable. Thus, further examination of input-output functions of cortical cells promises to provide more insight into fundamental computational properties of neocortical neurons.

In summary, a complicated interaction between intrinsic, dendritic and synaptic factors determines the input-output behaviour of pyramidal cells. In the following section, I will look at modulation of these input-output relations through dopaminergic receptor agonists.

4.2 Dopaminergic modulation of biophysical properties of deep layer pyramidal cells

Here I present the effects of applying selective dopamine receptor agonists SKF39383 (D1 receptor agonist) and quinpirole (D2 receptor agonist) on the intrinsic properties described above. These cells present only a subset (n=18) of the control dataset, since not all cells displayed stable patch clamp conditions until the end of the pharmacological stimulation.

First I will present an overview over the mean effects of dopaminergic stimulation, including a brief discussion of cell type specific effects. The results obtained from dopaminergic stimulation were analysed in a separate cluster analysis to reveal dopamine receptive subgroups, without any bias from previous classifications.

Overall effects of DA agonists

There were only few significant effects of dopamine receptor agonists on the measured variables. Table 4.2 shows the mean values for all cells for control (C), SKF39383 (D1) and quinpirole (D2) condition. All significant differences reported here are marked in the table and are based on separate one-way ANOVAs including post-hoc Tukey-Kramer test for multiple comparison ($p<0.05$). Application of either D1 or D2 agonist does not affect the affect the time constant [*tau*, C: 24.39 ±7.35 ms, D1: 25.53 ±6.57 ms, D2: 24.76 ±7.38 ms], the sag estimate [*sag*, C: 0.17±0.13 mV, D1: 0.22±0.18 mV, D2: 0.20±0.16 mV], the input resistance [*R(in)*, C: 85±24.07 MΩ, D1: 90.85±27.71 MΩ, D2:83.78±25.85 MΩ] or the reversal potential [*E(rev)*, C: -60.09 ±2.78 mV, D1: -57.89 ±3.54 mV, D2: -59.32 ±4.32 mV].

A significant change occurs for the current value at the minimum slope of the voltage clamp I-V curve after D1 stimulation [*I(min(dV/dI))*, D1: 69.16±32.08 pA] compared to control conditions [*I(min(dV/dI))*, C: 102.85±43.94 pA]. D1 seems to shift the V-I curve towards lower current values, effectively increasing excitability.

D1 agonist application significantly reduced both the upward rheobase current values [*Rmp (u): rheobase*: C: 117.70 ±47.02 pA, D1: 80.89 ±31.86 pA, D2: 102.60 ±55.51 nA] and the downward ramp rheobase [*Rmp (d): rheobase*: C: 146.87 ±39.91 pA, D1: 109.51 ±27.32 pA, D2: 140.31 ±55.62 nA], whereas the D2 agonist had no significant effect. Also, neither a D1 nor a D2 agonist has a significant effect on the maximum firing rate during an upward ramp injection [*Rmp(u): max (f)*, C: 13.86 ±3.57, D1: 14.57 ±2.88, D2: 14.32 ±4.31 Hz]. But in the case of a downward ramp injection, both application of either D1 or D2 receptor agonist reduces the maximally evoked firing rate significantly [*Rmp(d): max (f)*, C: 92.52 ±46.39 Hz, D1: 59.93 ±32.7 Hz, D2: 63.14 ±33.74 Hz].

Table 4.2 Mean effects of dopamine receptor agonists.

	Control	D1	D2
Tau	24.39 ±7.35	25.53 ±6.57	24.76 ±7.38
Sag	0.17 ±0.13	0.22 ±0.18	0.20 ±0.16
R(in)	85.03 ±24.07	90.85 ±27.71	83.78 ±25.85
E(rev)	-60.09 ±2.78	-57.89 ±3.54	-59.32 ±4.32
I-V: min(dV/dI)	-2.25 ±2.36	-2.24 ±3.23	-1.15 ±2.65
I-V: I(min(dV/dI))	102.85 ±43.94	**69.16 ±32.08 ***	91.65 ±46.99
I-V: bump	12.71 ±12.72	11.77 ±16.67	5.85 ±13.24
I-V: max(I)	1051.24 ±287.76	930.00 ±327.48	964.46 ±382.40
Rmp (u): rheobase	117.70 ±47.02	**80.89 ±31.86 ***	**102.60 ±55.51&**
Rmp (d): rheobase	146.87 ±39.91	**109.51 ±27.32 ***	**140.31 ±55.62#,&**
Rmp(u): max(f)	13.86 ±3.57	14.57 ±2.88	14.32 ±4.31
Rmp(d) max(f)	92.52 ±46.39	**59.93 ±32.71 ***	**63.14 ±33.74 ***
V-I: max(dI/dV)	0.11 ±0.05	0.11 ±0.05	0.12 ±0.04
V-I: onset	118.66 ±39.64	100.83 ±32.99	120.03 ±45.70
V-I: a(ISI_0)	4.67 ±1.74	4.54 ±1.73	5.27 ±2.05
V-I: b(ISI_0)	-43.21 ±20.91	-37.34 ±16.24	**-49.31 ±27.34&**
V-I: a(ISI_∞)	1.43 ±0.70	**0.99 ±0.54 ***	**1.43 ±0.93&**
V-I: b(ISI_∞)	-14.25 ±9.29	**-7.35 ±6.42 ***	**-13.69 ±12.19&**
V-I: CV	0.18 ±0.08	0.22 ±0.13	0.22 ±0.13

* significant difference to Control (two tailed t test, $p<0.05$), # significant difference of D1 against D2 (two tailed t test, $p<0.05$), & significant difference in variance D1 against D2 (two tailed F-test $p<0.05$). See Methods for appropriate units.

Dopaminergic agonists had little effect on the measured parameters during long current ramp injection. The D1 agonist decreased the coefficient [*V-I: a(ISI_∞)* C: 1.43 ±0.70, D1: 0.99±0.54, D2: 1.43±0.93] and the y-intercept [*V-I: b(ISI_∞)*, C:-14.25±9.29, D1:-7.35±6.42, D2: -13.69 ±12.19] of the square root fit to the steady state ISI. Therefore a D1 agonist reduces the steady state firing rate as the square root fit is less steep for the D1 condition.

To briefly summarise, when looking at the average across all cells recorded with D1 and D2 agonist, there are 6 significant changes in variables induced by D1 receptor agonist and 1 significant change induced by a D2 receptor agonist.

Bath application of a D1 receptor agonist significantly reduced the current value at which the minimum slope occurred in the voltage clamp V-I curve. It significantly reduced both rheobase currents (increasing and decreasing ramp), but also decreased the maximum firing rate evoked

through a decreasing ramp and significantly reduced both parameters of the square root fit for the steady state ISI.

This shows that dopamine receptor activation has significant effects across different subtypes of deep layer pyramidal cells, but they depend on the stimulation protocol. D1 receptor activation increases excitability for a slow increase in excitatory input (during a slow upward current ramp). In contrast, the response to sudden and strong excitatory drive (downward current ramp) is reduced and the transition from spiking to rest (rheobase, down) is shifted towards lower currents. Furthermore, activity towards the steady state seems to be reduced as well as both coefficients for the square root fit of ISI intervals are significantly reduced.

D2 receptor activation shows only one significant effect, it reduces the maximally evoked firing rate for a downward ramp, which is identical to the D1 effect.

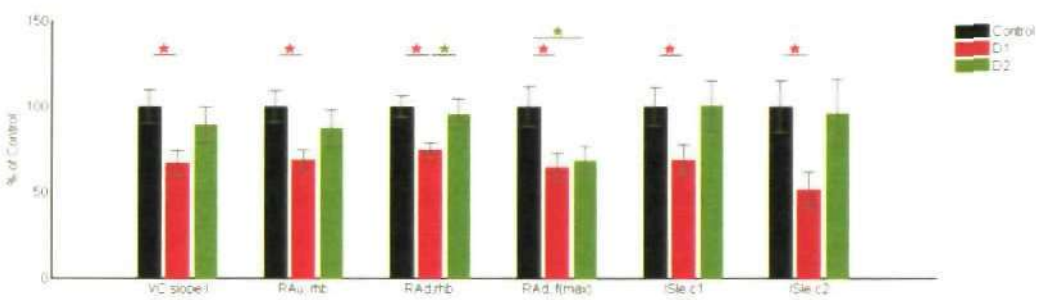

Figure 4.10 | Summary of overall DA agonist effects
Six variables show significant effects of either D1 (red) or D2 (green) agonist application compared to control condition (black), when averaged across all recorded cells. *two tailed independent sample Student test ($p<0.05$)

Analysis based on control condition cluster

In order to recognise possible cell type specific effects I have reanalysed the data through a series of one-way ANOVAs using cluster assignments obtained from the control dataset as independent variables (Table 4.3). Only cells with all protocols recorded during D1 and D2 agonist application were included (n=18). For RS cells (n=8) D1 decreases maximum firing rate for a decreasing ramp significantly (unequal sample size 1-way ANOVA, with post hoc Tukey-Kramer test, $p<0.05$). For the IB cells (n=5) six significant effects remain. In IB cells D1 stimulation increases the membrane time constant and the maximum firing rate for an increasing current ramp injection, but reduces the minimum slope of the voltage clamp V-I curve, the rheobase current for both increasing and decreasing current ramp injection, and the maximum frequency for a decreasing current ramp injection (Table 4.3). Surprisingly, the effects of D1

and D2 receptor activation seem to be similar for most of these variables (with exception of the time constant and the downward rheobase current).

There are no significant effects of dopamine receptor agonists on the IM cell type cluster.

A more detailed look at D1 and D2 effects reveals that some responses for D1 and D2 receptors can be very heterogeneous across different cells. Figure 4.11 depicts values for four selected variables and the effect of dopamine receptor agonists. Here two characteristics of the voltage clamp based I-V curve (minimum slope and bump height) show quite heterogeneous changes after dopamine receptor application. Especially for the bump height D1 or D2 agonist induces either increase and decrease in the bump height. Although the means [*I-V: bump,* C: 12.71 ±12.72 pA, D1: 11.77 ±16.67 pA, D2, 5.85 ±13.24 pA], which are indicated as bars in Figure 4.11, are not significantly different. Instead all variables show rather large standard derivations, as seen in the spread of points. In contrast, other variables, for example the coefficient and y-intercept for the square root fit of the spike latency, show rather homogenous effects. Due to the large heterogeneity of some variables, I sought to assess receptor specific effects through a separate PCA/HCA analysis that included D1 and D2 modulated variables into the database.

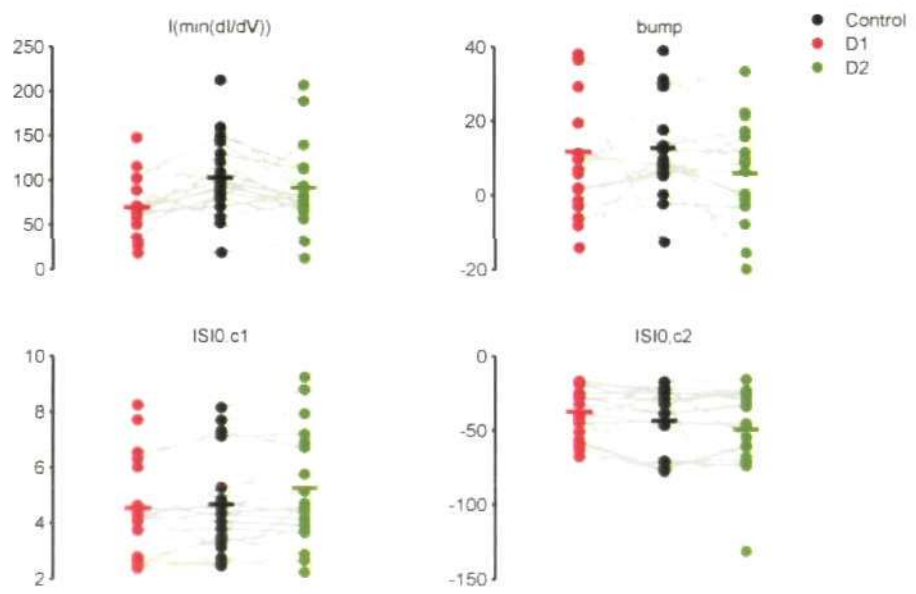

Figure 4.11 | Inhomogeneous effects of dopamine receptor stimulation
Top) DA agonist application can have heterogeneous effects on variables: e.g. the current of the maximum slope [*I-V: I(max(dI/dV))*] (top left) and the bump height [*I-V: bump*] (top, right) measured from the voltage clamp I-V curve.
Bottom) DA agonist application can also have homogenous effects on other variables: e.g. both constants of the square root fit to spike latency [$a(ISI_0)$, $b(ISI_0)$]. Note the clustering of control values.

Table 4.3 DA effects in control cluster

	IB			IM			RS		
	Control	**D1**	**D2**	**Control**	**D1**	**D2**	**Control**	**D1**	**D2**
Tau	16.26	20.19 *	17.92	19.87 [&]	25.06	23.37	29.80 [&]	28.33	28.6
Sag	0.34 [&]	0.46	0.39	0.13 [&]	0.21	0.22	0.1	0.1	0.09
R(in)	57.67	59.18	58.74	69.53 [&]	82.76	72.99	103.36[&]	109.1	99.54
E(rev)	-59.60[&]	-57.11	-57.79	-64.09	-58.32	-63.26	-59.15[&]	-58.14	-58.91
I-V: max (dV/dI)	-1.01[&]	-0.38	-0.53	-6.28	-5.74	-5.16	-1.67 [&]	-2.12	-0.25
I-V:I (max (dV/dI))	129.25	**81.84** *	**88.11** *	154.80[&]	79.23	123.67	74.06 [&]	59.8	83.81
I-V: bump	5.64[&]	1.89	2.64	33.27	31.15	25.76	10.07 [&]	10.9	1.48
I-V: max(I)	1146.62	988.79	990.12	848.43	741.54	754.65	1064.39	957.14	1014.57
Rmp (u): rheobase	138.29	**89.90***	**96.26** *	182.26[&]	109.04	139.52	88.03 [&]	67.94	94.69
Rmp (d): rheobase	158.6	**114.30***	121.25	205.82	134.04	167.17	123.31[&]	99.75	141.78
Rmp(u): max (f)	13.96	**16.50***	**16.26** *	9.23	13.25	12.39	15.20 [&]	14	13.93
Rmp(d): max (f)	150.75[&]	**99.09** *	**95.27***	44.79 [&]	62.91	63.64	77.73	**39.46** *	**46.93** *
V-I: max(dV/dI)	0.16	0.17	0.15	0.12	0.12	0.12	0.09	0.08	0.1
V-I: onset	135.21	119.72	119.71	167.14	142.75	149.22	111.92	89.06	129.96
V-I: a(ISI_0)	7.03 [&]	6.97	7.52	4.56 [&]	4.1	4.87	3.53	3.47	4.26
V-I: b(ISI_0)	-69.38	-59.33	-66.75	-51.09[&]	-39.7	-49.49	-27.75[&]	-25.64	-40.53
V-I: a($ISI\infty$)	2.24	1.55	2.3	1.55 [&]	1.05	1.56	0.99	0.69	0.96
V-I: b($ISI\infty$)	-24.54	-13.52	-22.17	-17.59[&]	-9.61	-17.06	-8.1	-3.58	-8.44
V-I: CV	0.16	0.2	0.16	0.13	0.16	0.13	0.21	0.24	0.28

* One-way ANOVA with post-hoc Tukey-Kramer test, $p<0.05$.

See Methods for appropriate units.

Hierarchical cluster analysis of dopaminergic modulated biophysical properties

To unravel possible specific effects of dopamine receptor activation I have performed a hierarchical cluster analysis which included variables from dopamine receptor agonist conditions. Here I have used the same procedure as described before for clustering the control variables. First I employed PCA to reduce the dimensionality of the data (a total of 57 variables from 18 cells). Again the first 3 principal components were then fed into a cluster analysis to establish group effects.

Figure 4.12 summarises the results of the hierarchical cluster analysis of combined control and DA-modulated variables (n=18). Similar to the previous section, I have combined a bar and whisker plot (left) with a dendrogram (top, right) and a colour coded data matrix of all variables (bottom, right) to show the result of the cluster analysis. Three distinct clusters were found. These cluster will be referred to as cluster DA-a (n=9, dark purple), DA-b (n=5, light purple), and one possible third cluster (DA-c, n=3, purple). There is also one cell with a very high distance to cluster DA-b which will be excluded from further analysis. The two largest clusters show a clear separation in the data matrix. Cluster DA-c is more similar to DA-a, than DA-b. In fact the second cluster, DA-b, is identical with the previously established IB cluster. The DA-b cluster is compact and has small inter-cell distances in the dendrogram, but with the two other clusters inter-cell distance is fairly large, which point to more heterogeneity within these clusters.

Figure 4.13 visualises the overlap between two cluster solutions by indicating cluster membership by different colours. Here it is easy to see that the IB cell cluster is identical with the DA-b cluster. The DA-a cluster consists of cells that have previously been classified as either RS (overlap =5) or IM (overlap=4) cells. Cluster DA-c (n-3) consists entirely of RS cells. This indicates that dopaminergic modulation of RS and IM cells is more heterogeneous. In the following section I will describe differential effects of dopamine for these clusters.

The results of the PCA were analysed to identify the variables contributing most to the principal components. Figure 4.14 shows a summary of the PCA results. A plot of cell properties in the reduced variable space (biplot) shows that the established clusters are well separated (Figure 4.14 A). Here all 3 principal components are plotted, since a scree plot of summed variances for each PC (Figure 3.7 B) revealed that the PC1 only contributes about 40% of the total variability. Together the first three PCs sum up to 64% of total variance, which slightly less than for the previous PCA. This is likely due to the higher number of variables included in this PCA. Still, the first three PCs explain considerable variability in the dataset. This was deemed sufficient since clustering results with more PCs included did not differ qualitatively (not shown). The variables with the highest factor loading for each PC are indicated as vectors in the biplot

(positive: yellow, negative: red, Figure 4.14 A) to illustrate their contribution relative to the PCs.

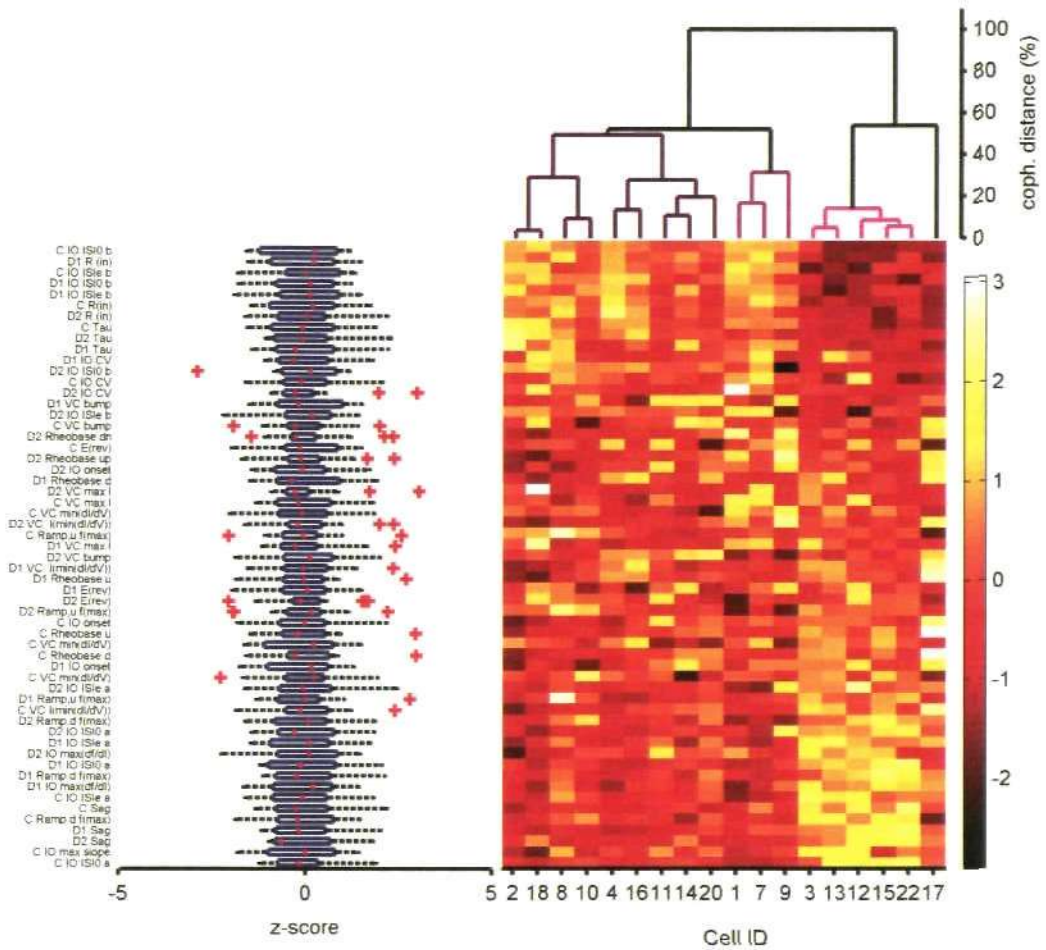

Figure 4.12 | Summary of cluster analysis including dopaminergic conditions
Top) Dendrogram obtained for Ward's method using a Euclidean distance matrix of control and dopamine modulated variables. Bottom, left) Box and whisker plot of all variables. Bottom, right) Colour coded normalised data matrix. Note the clear separation of the two largest clusters in the data matrix.

The passive membrane time constant [*Tau*] in control condition and the maximum slope of the steady state firing f-I curve [*I-V: max (dV/dI)*] in the D1 condition have the highest factor loading for PC1. The maximum firing rate for an upward ramp [*Rmp(u): max (f)*] in control condition and the rheobase current for an upward ramp [*Rmp (u): rheobase*] have the highest factor loading for PC2, whereas the maximum slope for the voltage clamp I-V curve [*max (dV/dI)*] in control condition and the I-V curve bump deepness [*I-V: bump*] in the D2 condition have the highest factor loading for PC3. Here it appears that all positive loadings include control variables, but the highest negative loadings are either D1 or D2 related variables. Indeed, when looking at the six most contributing variables for each PC (Figure 4.14 C), PC1 distinguishes

control and D1 variables, whereas PC2 distinguishes control and D2 variables. PC3 is a combination of variables in all three conditions.

To assess significant differences between cluster and between pharmacological treatments within cluster I performed a series of one-way ANOVAs. Table 4.4 shows a summary of all significant effects of DA in clusters DA-a, DA-b and DA-c.

In the largest cluster, DA-a, two variables are significantly modulated by D1 receptor activation. D1 receptor agonist SKF38393 reduced the maximum frequency during a downward current ramp injection from [*Rmp(d): max (f), C:* 80.09 Hz] to [*Rmp(d): max(f),* D1: 45.07 Hz]. Additionally, D1 reduced the y-axis intercept of the square root fit to $1/ISI_{\infty}$ from [$b(ISI_{\infty})$, *C*: 10.84 Hz] to [$b(ISI_{\infty})$, D1: -4.58 Hz].

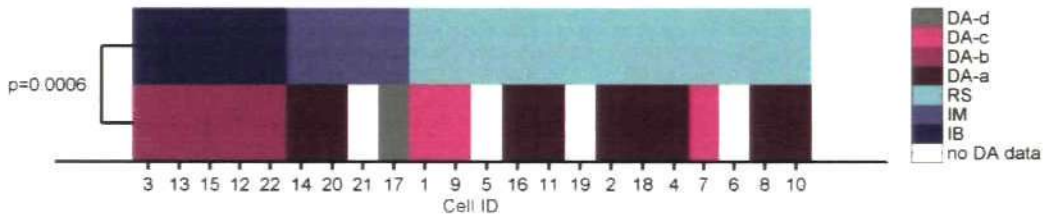

Figure 4.13 | Cluster overlap of control and DA cluster
When including DA modulated variables into the dataset, IB cluster is found again in the DA dataset (DA-b). A cluster assignment is found for non-IB cells, where a subgroup of RS (n-3) cells form a new cluster (DA-c)

As mentioned previously, DA modulation for IB cells is very consistent. Cells in the DA-b cluster (IB cells) exhibit two significant effects that are unique to D1 receptor activation (i.e. not similar to the D2 condition): Bath application of SKF38393 increased the membrane time constant from [*Tau*, C: 16.26 ms] to [*Tau*, D1: 20.19 ms] and decreased rheobase current for a downward current ramp injection from [*Rmp(d): rheobase,*C: 158.60 pA] to [*Rmp(d): rheobase* D1: 114.30 pA]. The values for the respective D2 condition show a similar trend to the D1 values, but did not reach significance. Besides, four significant effects remain that show similar values for both D1 and D2 application. D1 or D2 application increased the maximum firing rate during an upward current ramp injection from [*Rmp(u): max (f),* C: 13.96 Hz] to [*Rmp(u): max (f)*, D1: 16.50 or D2: 16.26 Hz], but decreased the maximum instantaneous firing rate during a downward current ramp injection from [*Rmp(d): max (f),* C: 150.75 Hz] to [*Rmp(d): max (f),* D1: 99.09, D2: 95.27 Hz]. In addition, D1 or D2 receptor agonist application attenuated the current value at the minimum slope of the voltage clamp V-I curve from [*I-V: I (max(dV/dI)),* C: 129.25 pA] to [*I-V: I (max(dV/dI)),* D1: 81.84 pA, D2: 88.11 pA]; and reduced the rheobase current for an increasing current ramp injection from [*Rmp(u): rheobase*, C: 138.29 pA] to

[*Rmp (u): rheobase*, D1: 89.90 pA, D2: 96.26 pA]. There are no significant differences between D1 and D2 effects for all these variables.

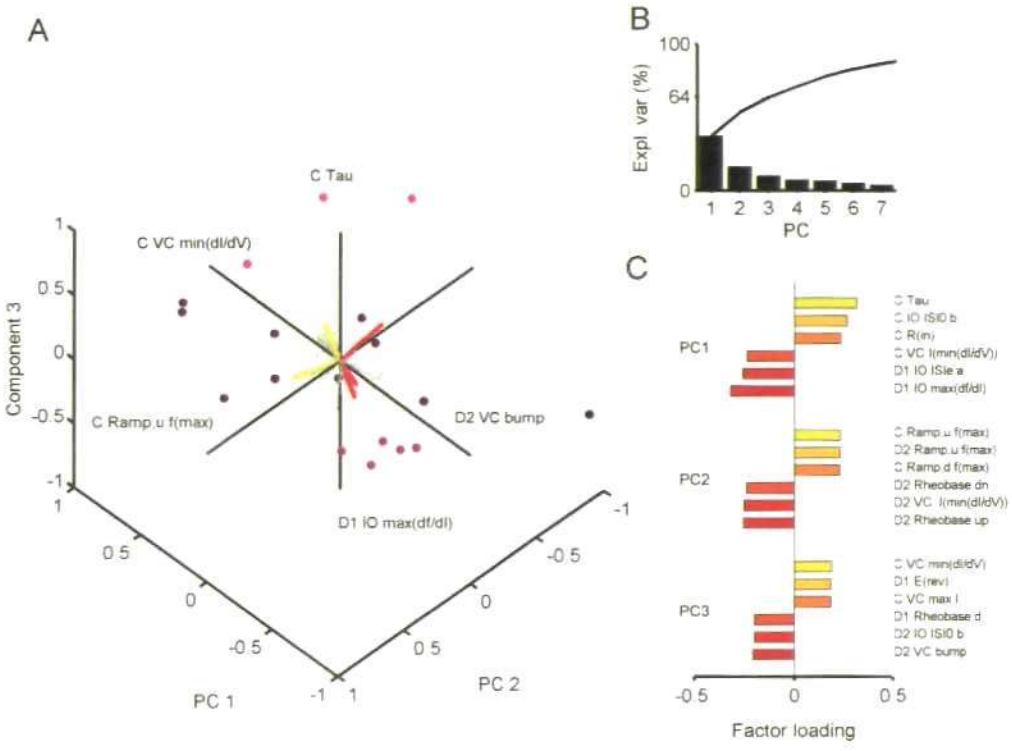

Figure 4.14 | PCA results by DA cluster solution
A) Scatter plot of cell positions (dots) within the coordinate system spanned by the first 3 PCs, cell are coloured according to the dendrogram in Figure 4.10. B) Scree plot of PCs. PC1-3 explain 64% of the total variance in the dataset. C) Bar plot of variables that contribute most to the first 3 PCs.

In the small DA-c cluster (n=3) D2 effects are very strong and reach significance despite the few cells recorded. In particular quinpirole increased the mean rheobase current for an upward ramp from [*Rmp (u): rheobase*, C: 95.24 pA] to [*Rmp (u): rheobase*, D2: 172.83 pA] which is only significantly different compared to the value D1 condition [*Rmp (u): rheobase*, D1: 64.63 pA]. Quinpirole also increased the mean rheobase current for a downward ramp from [*Rmp(d): rheobase*, C: 131.22 pA] to [*Rmp(d): rheobase*, D2: 223.49 pA] which is, again, only significant compared to the D1 condition [*Rmp(d): rheobase*, D1: 88.34 pA]. D2 agonist application also decreased mean maximum firing rates during both ramp protocols. quinpirole decreased the maximum firing rate during an upward current ramp from [*Rmp(u): max (f)*, C: 12.83 Hz] to [*Rmp(u): max (f)*, D2: 7.62 Hz], which is also only significant compared to the value obtained under D1 agonist application [*Rmp(u): max (f)*, D1: 13.54 Hz]. Likewise, quinpirole significantly decreased the mean maximum instantaneous firing rate during a downward current ramp to [*Rmp(d): max (f)*, D2: 15.93 Hz] compared to the control value [*Rmp(d): max (f)*, C:

62.49Hz]. Subsequent D1 agonist application reversed this effect partly [*Rmp(d): max (f)*, D1: 31.41Hz], but was not significantly different compared to the control or the D2 value.

Figure 4.15 summarises the main effects of DA agonist. DA-a shows only D1 effects, DA-b cells show both similar D1 and D2 effects, whereas cells in cluster DA-c show only D2 effects.

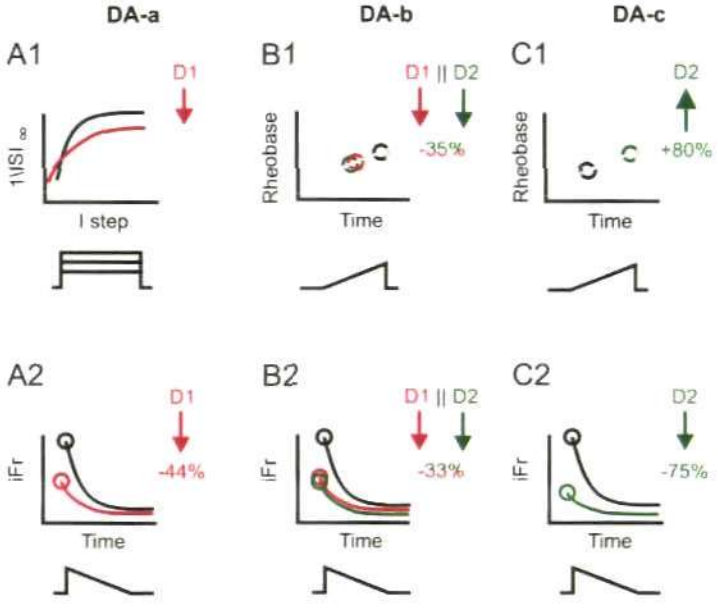

Figure 4.15 | Summary of main significant DA agonist effects.
Schematic of the most significant DA effects in all DA clusters. DA-a: A1) D1 reduces the coefficient and y-intercept of the sqrt(1/ISI_∞) fit . A2) D1 agonist reduces max iFR by 44%. DA-b: B1) D1 and D2 reduce the rheobase current by 35% and the max iFR during downward ramp by 33%. DA-c: C1) D2 receptor stimulation increases rheobase current by 80%, and C2) reduces max iFR by 75%.

To investigate systematic differences between clusters in further detail, the input-output functions obtained from all protocols were plotted for each cluster.

When plotting the average I-V relationship obtained from voltage clamp for each cluster (Figure 4.16), there are no significant differences between control and application of dopaminergic agonists for the large cluster DA-a (independent sample t-test for, $p<0.05$). In contrast, for cells in cluster DA-b there are significant differences for both, the D1 agonist at voltage levels -45 and -40 mV, and the D2 agonist at voltage of -45 mV to the control condition. Here both dopamine agonists decrease the net membrane current near the threshold for action potential initiation. For the smallest of the three clusters DA-c, there are significant differences for lower voltage values. Here the opposite effect of D1 vs. D2 receptor activation within the cluster is visible, but also D2 stimulation seems to have opposite effects in terms of excitability compared to those seen in DA-b (IB) cells. The voltage clamp I-V curve is shifted upwards on the current

axis and flattened out compared to the control condition. But significant differences are only seen in a few mean values with very low standard errors. This is probably due to the low number of cells in this cluster. The I-V curve is significantly different from the control condition for current values at more hyperpolarised voltage levels of 60 and 55 mV (green stars, independent sample t-test, $p< 0.05$). The curve obtained in the D2 agonist condition is also significantly different from the D1 condition at voltage levels 55 and 50 mV (blue stars, independent sample t-test, $p< 0.05$).

Additionally, I examined the results of the slow current ramp injections. Figure 4.17 depicts the binned firing rate (in steps of 42 pA, or 0.5 s) against the binned injected current, for an increasing current ramp (Figure 4.17 A) and a decreasing current ramp (Figure 4.17 B) for each cluster. Note that Figure 4.17 B shows the injected current values on an inverse x-axis. There are no significant effects of dopamine receptor agonists on cells in cluster DA-a (Figure 4.17, left). In contrast, there are significant effects of both D1 and D2 agonist application on the binned firing rate during a slow upward and downward current ramp injection in the DA-b/IB cluster. Here Both D1 and D2 agonist shift the f-I curve towards lower current values, effectively increasing excitability. For cells in the DA-c cluster a strong inhibitory effect after D2 agonist application is observed (Figure 4.17, right). Although this effect appears strong, there are only a few significant differences in average firing rate. Only at two current levels there are significant differences induced by D2 agonist application (green stars, independent sample t-test, $p<0.05$). More values show significant differences between D2 and D1 agonist application (blue stars, independent sample t-test, $p<0.05$), although D1 effects themselves are not significantly different from control. Overall, D2 receptor agonist application reduces the average firing rate for both increasing and decreasing current ramps for the whole range of current values.

Next I compared the mean transient (first 5 seconds of the long current step, Figure 4.18 A) and steady-state (last 5 seconds of the long current step, Figure 4.18 B) f-I curve for each cluster. For cluster DA-a there are some significant effects of D1 application on the transient f-I curve (independent sample t-test, $p<0.05$) at medium current levels (Figure 4.18 A, left). There are no significant differences between dopamine agonist application and control condition for the steady state f-I curve. Although D1 receptor activation seems to slightly shift the curve to the left, this does not reach significance for any current level.

Table 4.4 Mean values of DA cluster.

	DA-a (n=9)			DA-b (n=5)			DA-c (n=3)		
	Control	D1	D2	Control	D1	D2	Control	D1	D2
Tau	28.31 &	28.07	30.41	16.26 ◊	**20.19** *	17.92	29.61	30.07	**21.22** * #
Sag	0.09 &	0.08	0.12	0.34 ◊	0.46	0.39	0.15	0.22	0.07
R(in)	95.70 &	105.57	99.54	57.67 ◊	59.18	58.74	110.77	114.08	90.27
E(rev)	-60.35	-58.62	-58.28	-59.6	-57.11	-57.79	-58.43	-56.11	-63.05
I-V: max (dV/dI)	-2.49	-2.99	-2.36	-1.01	-0.38	-0.53	-2.26	-2.54	2.51
I-V:I (max (dV/dI))	84.31	57.14	65.55	129.25	**81.84** *	**88.11** *	77.74	57.9	143.39
I-V: bump	15.03	15.72	12.01	5.64	1.89	2.64	11.27	13.8	-12.5
I-V: max(I)	924.67	835.96	913.24	1146.62	988.79	990.12	1349.48	1161.92	1114.68
Rmp (u): rheobase	97.77	71.36	72.03	138.29	**89.90** *	**96.26** *	95.24	64.63	**172.83** #
Rmp (d): rheobase	131.94	107.82	115.2	158.6	**114.30** *	121.25	131.22	88.34	**223.49** #
Rmp(u): max (f)	14.99	14.09	15.92	13.96	**16.50** *	**16.26** *	12.83	13.54	**7.62** #
Rmp(d): max (f)	80.09 &	**45.07** *	58.86	150.75 ◊	**99.09** *	**95.27** *	62.49	31.41	**15.93** *
V-I: max(dV/dI)	0.1	0.08	0.11	0.16	0.17	0.15	0.09	0.07	0.12
V-I: onset	110.3	93.55	118.98	135.21	119.72	119.71	134.64	108.7	158.95
V-I: a(ISI_0)	3.94 &	3.7	3.86	7.03 ◊	6.97	7.52	2.73	3.2	5.55
V-I: b(ISI_0)	-32.51 &	-27.5	-30.67	-69.38 ◊	-59.33	-66.75	-22.68	-28.47	-69.33
V-I: a(ISI_∞)	1.22 &	0.79	1.04	2.24 ◊	1.55	2.3	0.56	0.45	0.94
V-I: b(ISI_∞)	-10.84 &	**-4.58** *	-8.54	-24.54 ◊	-13.52	-22.17	-4.41	-2.36	-10.18
V-I: CV	0.19	0.22	0.22	0.16	0.2	0.16	0.26	0.28	0.36

Significant differences between clusters in control condition (one-way ANOVA with post-hoc Tukey-Kramer test, $p<0.05$) denoted by & (DA-a v DA-c) and ◊ (DA-b v DA-c). Significant differences within clusters but between pharmacological treatments (one way ANOVA with post-hoc Tukey-Kramer test, $p<0.05$) denoted by *(significant difference of D1 or D2 to control condition) and # (significant difference between D1 and D2 condition). See Methods for appropriate units.

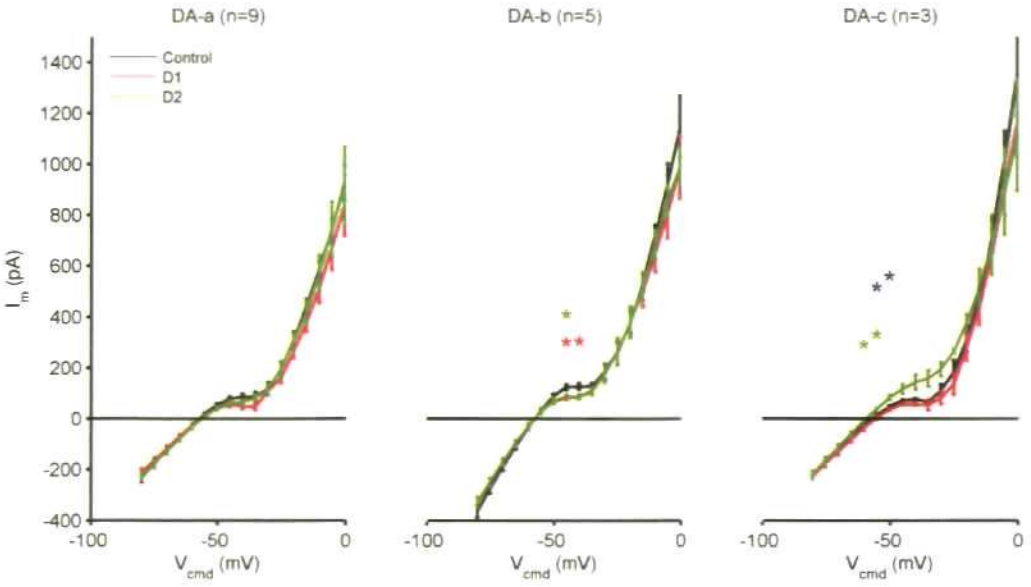

Figure 4.16 | Influence of dopaminergic agonist on voltage clamp I-V curves
Mean I-V curves for voltage clamp step stimulation for control (black), D1 (red) and D2 condition (green) for each cluster. Error bars indicate SEM, independent sample t-test ($p<0.05$): D1 vs. Control (*), D2 vs. Control (*), D1 vs. D2 (*).

The changes induced by dopamine receptor agonists are more pronounced in the DA-b cluster compared to cluster DA-a, for both the transient and the steady state f-I curve. The f-I curves obtained with bath application of a D1 or a D2 agonist both show a clear shift to the left (Figure 4.18, middle), which results in significant differences at four different current levels for D1 agonist application and at 5 different levels for D2 agonist application. Only a D2 agonist still achieves a shift of the f-I curve at very high current inputs (300 pA).

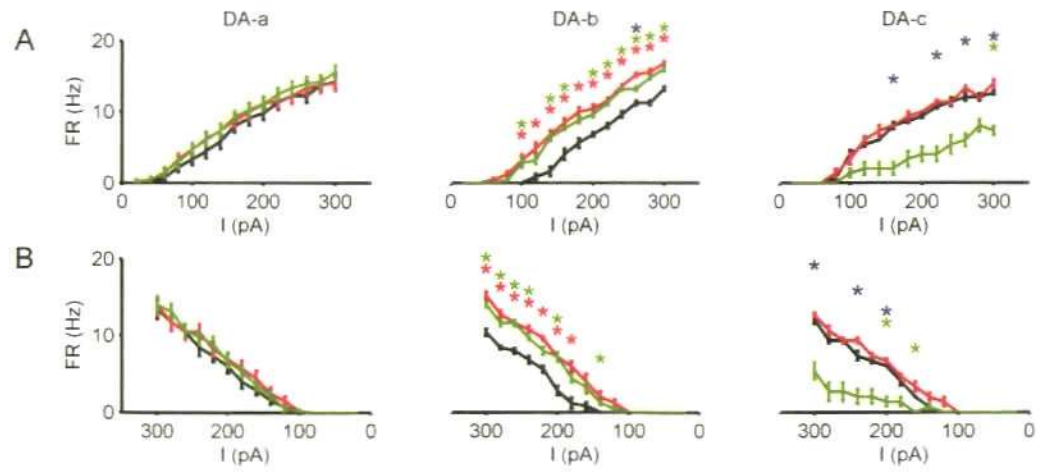

Figure 4.17 | Influence of dopaminergic agonists on ramp evoked f-I curves.
Mean f-I curves for an upward (A) and downward (B) ramp injection for DA cluster in control (black), D1 (red) and D2 condition (green). Error bars indicate SEM, independent sample t-test ($p<0.05$): D1 vs. Control (*), D2 vs. Control (*), D1 vs. D2 (*).

The steady state f-I curve for the smallest cluster (DA-c) showed different effects for transient and steady state f-I curve. The transient f-I curve (Figure 4.18 A, right) is shifted rightward and the gain is reduced, after application of a D2 agonist although this reaches significance only for one low current value (100 pA). There is no significant shift for either D1 or a D2 agonist of the steady state f-I curve (Figure 4.18 B, right). Although here it seems that there is a slight D1 effect for very low stimulus intensities, but this does not reach significance. Interestingly the average f-I curves for all conditions in this cluster seem have a lower overall gain (slope) compared to cluster DA-a.

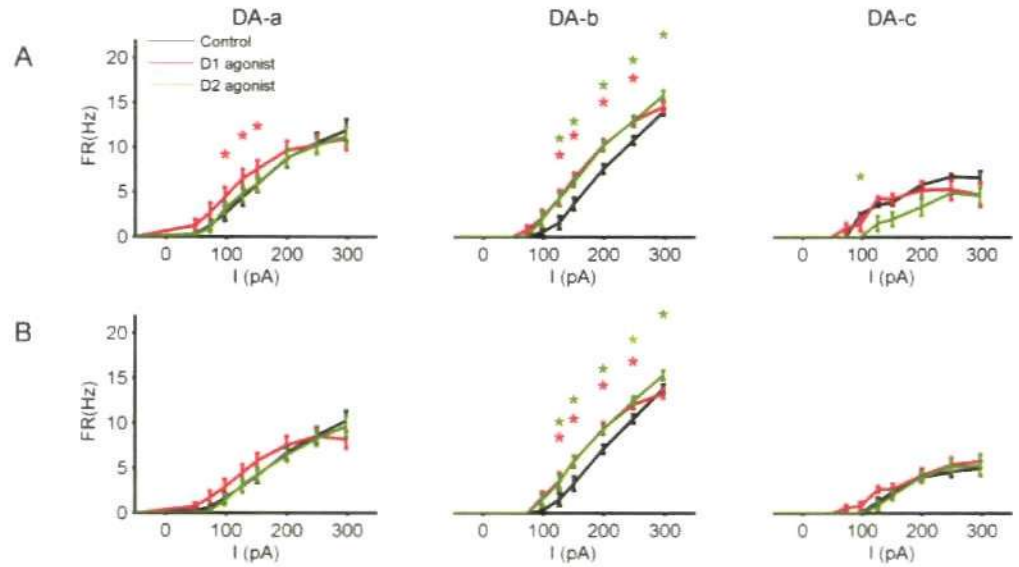

Figure 4.18 | Influence of dopaminergic agonists on transient and steady state f-I curve
A) Transient (first 5 sec) f-I curves for clusters DA-a to DA-c. B) Steady state (last 5 sec) f-I curves for DA cluster in control (black), D1 (red) and D2 condition (green). Error bars indicate SEM, independent sample t-test ($p<0.05$): D1 vs. Control (*), D2 vs. Control (*).

The results of the transient and steady state f-I functions are consistent with the results from averaging all mean square root (1/ISI) functions in Figure 4.19. For cluster DA-a there are no obvious effects of D1 or D2 agonist application on the average 1/ISI function. In contrast, for cluster DA-b the application of D1 or D2 agonist shift the spike latency curve ($1/ISI_0$) clearly to the left DA-b. For the steady state curve ($1/ISI_\infty$), D2 receptor agonist quinpirole shifts the curve clearly to the left, whereas D1 application also reduces the gain (slope) of the fitted curve. For the last cluster, D1 application seems to have little effect on average, but D2 receptor agonist quinpirole, shifts both the spike latency and the steady state curve strongly to the right (i.e. to higher current values).

To illustrate dopamine receptor influence on overall spiking statistics, ISI histograms of all ISIs (during all stimulation steps) for typical example cells from each cluster were plotted (Figure

4.20). The ISI distribution for cell number 2 from cluster DA-a (Figure 4.20, top) shows a peak at slightly above 10 Hz firing (100 ms ISI), with no ISIs at higher frequencies (<50 ms, 20Hz), and falls of very smoothly to lower frequency ISIs. D1 agonist application shifts the peak of the distribution towards lower ISI lengths and also broadens the whole of the distribution compared to control condition. This peak occurs at higher stimulation intensities, whereas for lower intensities D1 seems to enhance lower frequency firing. Thus the differential effects of D1 seem to be dependent on input strengths: D1 seems to reduce firing rate in response to strong inputs, but increases firing in response to low intensity stimuli. This is effectively a gain reduction and shift of the input-output curve to the left, although this effect does not become significant when comparing mean f-I relationships. Interestingly, the peak of the distribution lies at around 150 ms, which correlates to theta frequency firing (~7 Hz). Although, for some cells in this cluster the effect is less pronounced, or D1 even introduces higher frequency firing. Application of a D2 agonist also shifts the distribution to lower frequency firing, but less pronounced than D1 agonist application. The peak lies at around 10 Hz, with similar width and height as the control condition distribution.

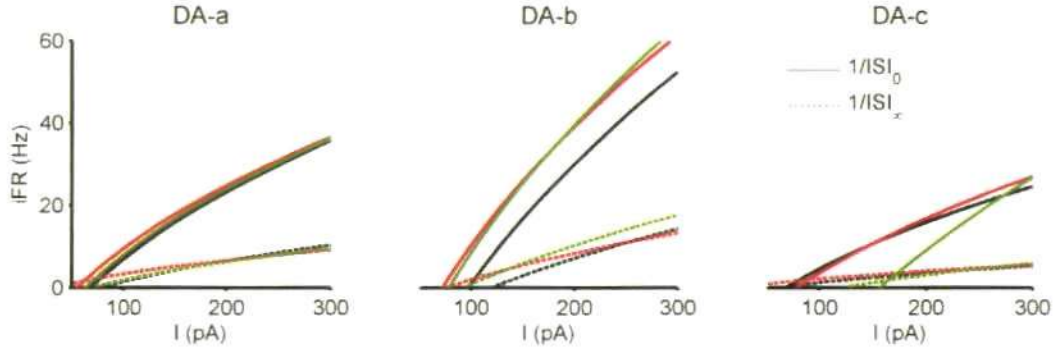

Figure 4.19 | Influence of dopamine agonists of averaged square root 1/ISI functions.
Mean square root fits in control (black), D1 (red) and D2 condition (green) to 1/ISI0 (solid line) and 1/ISI∞ (dashed line) for DA cluster.

For cells in cluster DA-b, the ISI distributions did not change much in mean or shape after D1 or D2 agonist application. In this particular example (Figure 4.20, middle), both agonists seem to increase the number of spikes in the same frequency ranges as those spikes that are fired during control condition. There is a slight increase in ISIs at around 125-150 ms, and a very slight increase in very low ISIs, that correspond to bursting (~10ms).

One cell from cluster DA-c shows a quite distinct ISI distribution, with the peak of the distribution at much higher ISIs compared to both DA-a and DA-b cells. Also, the distribution is much flatter and the cell emits less spikes overall (note different scale on the count axis), with a peak around 200-250 ms (5-4 Hz). This pattern of ISI distribution correlates to fast adapting

cells, which fire only a few number of spikes at low frequencies. D1 application increases the number of spikes fired for most ISI lengths and also shifts the peak slightly towards higher frequencies. This presents a mechanism for selectively increasing excitability for low or high intensity inputs. D2 application shifts the ISI distribution towards shorter ISIs, but reduces firing at intermediate frequencies (6-4 Hz) but D1 allows for higher frequency firing.

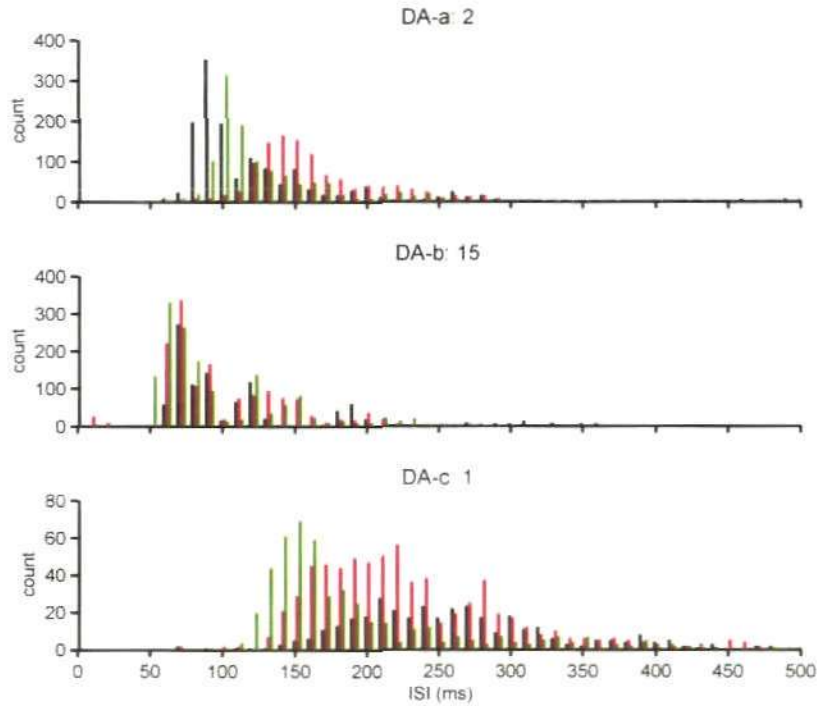

Figure 4.20 | DA influence on ISI histograms
Representative examples of ISI histograms of all spikes evoked by long current step stimulation at different current levels in control (black), D1 (red) and D2 condition (green). Top) cell #2 in cluster DA-a, middle) cell #15 in cluster DA-b, bottom) cell #1 in cluster DA-c.

Discussion of DA modulated cluster results: D1 effects

To summarise, D1 effects in all clusters except from DA-b, seem to be weak but consistent. For cluster DA-a, one significant effect was found within the cluster (Table 4.4). D1 agonist application reduces the maximum instantaneous firing rate for a downward current ramp injection. In addition D1 introduces a slight shift at intermediate current values in the transient long step f-I curve, although no significant effects were measured in the averaged ramp protocol f-I curve, or the long step steady state f-I curve. The same is true for the small DA-c cluster. There are no significant effects of D1 application when compared to control condition, but a few when compared to the D2 agonist condition.

In contrast, D1 receptor stimulation has a distinct effect on IB cells. D1 agonist application increases the gain for low intensity inputs both transiently and in the steady state, and there is a tendency to reduce firing in response to very strong stimulation. Overall, D1 receptor stimulation enhances excitability, especially to low stimulus intensities, and reduces firing to high intensity stimuli (i.e. the maximum instantaneous firing rate for a downward ramp) in all clusters.

The effects of D1 receptor stimulation seen in this study fit well with previous reports of D1 receptor modulation of intrinsic properties. D1 receptor activation has been shown to activate persistent sodium currents (Gorelova and Yang, 2000) which results in increased excitability and might also promote burst firing. Furthermore, D1 activation has been shown to reduce various potassium currents, i.e. inward rectifying potassium channels (IRKC) and a slow inactivating voltage gated potassium current, $I_{(K,D)}$. Both channels contribute to repolarising the cell to resting membrane potential and a reduction leads to an increase in excitability (Yang and Seamans, 1996; Dong and White, 2003; Dong et al., 2004). Furthermore, D1 stimulation has been shown to regulate calcium electrogenesis in prefrontal neurons (Yang and Seamans, 1996; Young and Yang, 2004; Seamans and Yang, 2004). This regulation is input dependent and might explain the effects of D1 receptor stimulation in cluster DA-a. In detail, Young and Yang (2004) showed that D1 receptor activation modulates mainly somatically located calcium channels dependent on the input strength. D1 receptor activation reduces supra-threshold calcium spikes through a PKC dependent pathway, but enhances sub-threshold calcium potentials through a PKA dependent activation of L-type calcium channels. This explains the selective gain increase for low intensity inputs seen in the current study and the reduction of high frequency firing by D1 receptor activation, since reduced calcium influx will be detrimental to calcium dependent back-propagating of action potentials, which can promote continuous firing.

A recent study by Thurley et al. (2008) has examined the effects of DA on input-output function of deep layer pyramidal cells in the rat prefrontal cortex. Using similar control conditions as in the current study (all fast synaptic transmission blocked) they have reported similar effects of DA on the gain of input-output functions, i.e. gain increase for low to intermediate intensity stimulation and reduction of firing rates to strong inputs. It has to be noted that Thurley et al. claim to have recorded only from regular spiking cells, but detailed characterisation of firing patterns is not reported. The stronger effect on regular spiking neurons seen in their study might also relate to the use of noisy current injections, which itself shifts the f-I curve of prefrontal pyramidal cells towards lower current values and higher firing rates (Arsiero et al., 2007). Thurley et al. (2008) also report a significant increase in membrane time constant through bath application of high DA concentrations (100 μM) while blocking fast synaptic transmission

(NMDA, AMPA and GABAa). This resembles the D1 effect seen in DA-b/IB cells in the current study, but as mentioned above Thurley et al. report to have recorded only RS type cells. In my hands RS-type cells did not show any significant changes in passive membrane properties. This might point to possible confusion of cell types in the study by Thurley et al., which is also indicated by their reported low averages for time constants (similar to IB cells) in very similar experimental conditions to the current study.

D2 effects

The effects of D2 receptor stimulation seem to be more diverse and depend on the cell type at hand. There is no evidence for D2 effects in the largest cluster DA-a. None of the values used in the PCA/cluster analysis did show significant effects, nor did any of the input-output relationships. The example ISI distribution might indicate reduced high firing rates, but the effect is not consistent across cells within cluster DA-a. On the contrary, D2 receptor stimulation has distinct and reproducible effects on bursting cells in cluster DA-b. It seems to enhance excitability for all input strengths, i.e. it shifts the input-output function clearly towards lower current input, without affecting the gain of the curve. The last cluster DA-c seems to consist of cells where D2 receptor stimulation reduces transient excitability dramatically. Bath application of a D2 receptor agonist reduces the gain of the f-I curve obtained by an upward or downward current ramp, and shifts it to higher current values. A similar effect is seen in the transient f-I curve for long current steps and the respective square root fits to ISIs. Hence a subpopulation of pyramidal cells that responds differently to D2 receptor activation might exist.

Previous reports on the effects of D2 receptor activation on intrinsic properties of pyramidal cells have been diverse and often contradicting. D2 receptor agonist have been shown to have mostly inhibiting effects in slice preparations, attributed mainly to activation D2 receptors on local inhibitory interneurons (Gorelova et al., 2002; Gao et al., 2003; Gao and Goldman-Rakic, 2003; Trantham-Davidson et al., 2004). In opposition, other studies have reported D2 receptor effects that could increase cell excitability. Gulledge and Jaffe (1998) reported increase in excitability after D2 receptor stimulation in the presence of a GABAa receptor blocker. Dong et al. (2004) showed that D2 receptor activation can reduce IRKC, and this is in fact the predominant effect observed *in vitro*. Moreover, D2 receptor activation has been shown to promote bursting in intrinsically bursting cells though a combination of synaptic (AMPA) and intrinsic mechanisms, where D2 receptor stimulation has been linked to augmenting low threshold spikes carried by low-threshold activated calcium currents (Wang and Goldman-Rakic, 2004). The latter could explain the observed effect of D2 receptor activation in bursting cells in the current study. Indeed, low voltage activated calcium currents have been reported to occur mainly in deep layers of the rodent PFC (de la Pena and Geijo-Barrientos, 1996).

These inhibitory effects of D2 receptor agonists on excitability in pyramidal cells in the DA-c cluster have, to my knowledge, not been observed yet. These effects might have coincided with effects observed in interneurons. Since in the current study all GABA transmission was blocked, effects mediated by local interneurons should be excluded, unless synaptic blocking was incomplete. This is unlikely, since ACSF solution was first switched to contain only synaptic blockers where the disappearance of spontaneous PSP was carefully monitored, and only then were dopamine receptor agonists bath applied. Still, further experiments are advised to confirm this D2 receptor mediated inhibition, since the number of cells that show this particular effect is small.

Opposite effects of D1 and D2 receptor stimulation

Opposing actions of D1 vs. D2 receptor stimulation can be explained by their action on intracellular signalling mechanisms. For example, application of a D1 agonist induces a significant increase in the membrane time constant in DA-b/IB cluster cells, whereas D2 receptor activation reduces the membrane time constant in cells in the cluster DA-c (Table 4.4). Although the membrane time constant tau, as estimated here from brief depolarising current steps, has been used as a measure of passive synaptic integration, it has been pointed out that tau can be only used as a rough estimate of integrative properties of neurons (Koch et al., 1996). Instead, it is likely that fast currents activated near threshold contribute to shaping the time constant estimated from hyperpolarising steps. In fact, D1 receptor stimulation has been shown to increase the membrane time constant in EC pyramidal cells by increasing intracellular cAMP (via G_s-type G-proteins) and reducing HCN currents (I_h) (Rosenkranz and Johnston, 2006). Since IB-type cells in this study showed stronger I_h components (sag) it is likely that a similar mechanism is in place in this cell type. Indeed there is a non-significant increase in the sag component after D1 agonist application in IB cells, in favour of this explanation. It might equally explain the reduction of the time membrane constant seen in the DA-c cluster. D2 type receptors coupled to G_i-type G-proteins inhibit adenylate cyclase, thus reduce intracellular cAMP formation (Neve and Neve, 1997), which concurs a reduced mean sag after D2 agonist application in cluster DA-c cells. Why these opposing DA receptor effects do not occur simultaneously in the same cell type remains to be explained.

DA effects by cell type

As seen in the comparison between cluster solutions (Figure 4.13), cells previously classified as RS cells are heterogeneous in their response to DA. Three cells from the previous RS cluster formed cluster DA-c (showing strong D2 effects), whereas two cells from the intermediate

cluster were included into the large DA-a cluster (showing weak D1 effects). One simple explanation for heterogeneous DA effects might be different expression levels of D2 receptor expression within RS cells, i.e. a possible subpopulation of RS cells that has increased D2 receptor numbers. Indeed DA receptor expression varies considerably for pyramidal cells and interneurons, across and within layers in the rat PFC (Vincent et al., 1993, 1995; Gaspar et al., 1995; Santana et al., 2009). One recent study, where DA receptor expression was assessed through in situ hybridisation (Santana et al., 2009), shows that the highest proportion of D1 and D2 receptor expressing pyramidal cells is found in layer V, where some cells express very high levels of either D1 or D2 mRNA (colocalisation was not tested) compared to average expression in the PFC. These 'hot spots' of DA receptor expression might explain variability in responses to dopamine receptor stimulation.

IB cells constitute a very distinct cell population with consistent DA modulation of intrinsic properties. The counterintuitive result of this study is that D1 or D2 receptor stimulation seems to have almost identical effects on excitability of cells in the IB/DA-b cluster. Both D1 and D2 agonists increase excitability in response to current stimulation in the form of a slow ramp protocol or long current step. Previously both D1 and D2 receptor agonist application has been shown to have long lasting effects on synaptic conductances that outlast the application of the respective agonist (Seamans et al., 2001a, 2001b). It could be argued that similar effects of D1 and D2 receptor activation seen in the current study stem from the sequence of agonist application in the experiment (first quinpirole, then SKF 39383), where D1 receptor activation failed to have any effect, but instead a persistent D2 effect would be measured. Preliminary results from application of only a D1 receptor agonist to intrinsically bursting cells (data recorded by Thomas Gabriel) indicate that D1 receptor agonist SKF 39383 shows a similar effect on the steady state f-I curve as seen in the current study.

To my knowledge, no other study has reported specific effects of DA receptor activation on subtypes of pyramidal cells. Although Yang and colleagues have distinguished several pyramidal cell types in the rat PFC (Yang et al., 1996), they did not report any cell type specific dopaminergic effects in an accompanying paper on dopamine modulation (Yang and Seamans, 1996). Although this characterisation of dopaminergic in deep layer pyramidal cells is far from complete, it points to some interesting possibilities of cell type specific actions of dopamine.

This raises the important question of how DA receptor activation would affect the computational properties of these different pyramidal cell populations in the prefrontal cortex.

In RS cells you can see an amplification of low intensity inputs, effectively making the resting to spiking transition easier. The input-output function shifted towards lower stimulus intensities

and increased sensitivity for transient inputs, as shown in the transient V-I curve during upward current ramp injection. This is similar to the effect described by Thurley et al (2008). In a network simulation of integrate and fire neurons Thurley et al. show that this increase in gain for low intensity inputs stabilises persistent activity states through widening the basin of attraction for the respective stable fixed point.

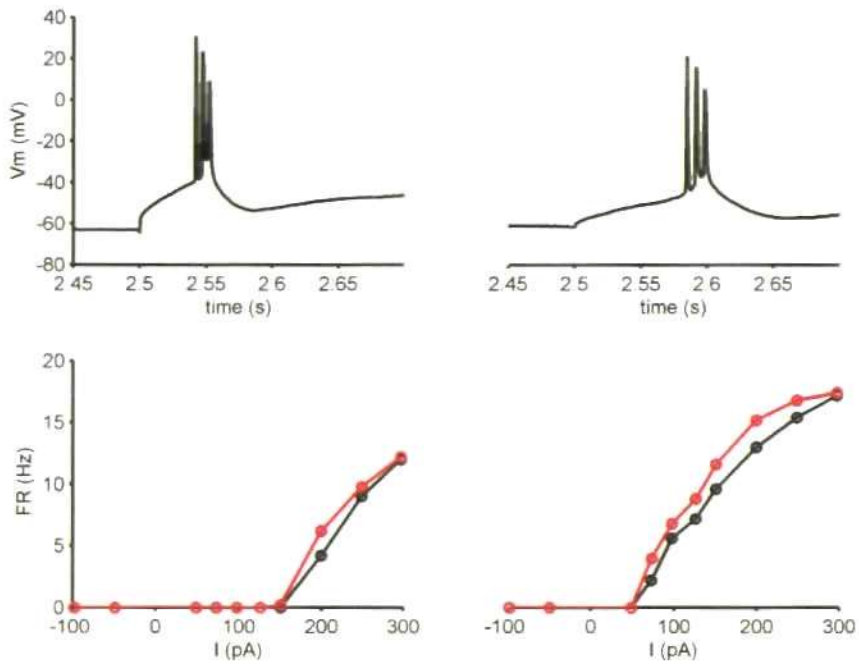

Figure 4.21 | D1 agonist application in bursting pyramidal cells
Application SKF 39383 (50 µM) plus blocker for all fast synaptic transmission (without previous D2 agonist application) introduces a similar increase in gain of f-I curve for putative IB cells (recorded by Thomas Gabriel).

In addition, a D1 receptor agonist shifts the voltage clamp I-V curve towards lower current values, essentially pushing DA-a and DA-c cells closer towards intrinsic bistability. Hence, these cells become more susceptible to low intensity input and are easier pushed into a stable firing rate regime, which can be used as a short term memory buffer to encode recent stimulus inputs after these stimuli have gone. This would be in line with previously described effects of D1 receptor stimulation on synaptic properties (Durstewitz and Seamans, 2002) and further contribute to stabilisation of persistent activity in prefrontal networks. Moreover, there is a slight reduction in responsiveness to very strong inputs (reduced maximum instantaneous firing rates to downward ramp) which probably relates to reduced intraburst ISIs. This might indicate a dampening of strong inputs to further enhance stability of persistent firing regimes and prevent runaway excitation.

In a subset of cells (cluster DA-c) D2 receptor activation has the opposite effect: it shifts the I-V curve up on the current axis and makes the I-V curve more monotone. This effect is only observed in a few cells (n=3). It might implement a cell type specific shunting of activity after D2 receptor activation, but further experiments need to confirm this cell type specific action of D2 receptors.

In DA-b cells both D1 and D2 type receptor activation shifts input-output functions towards lower strength inputs, but interestingly in DA-b cells D1 activation reduces non-significantly bump deepness of the voltage clamp I-V curve, i.e. it makes the I-V curve more monotonic. Therefore, DA receptor stimulation increases intrinsic excitability in DA-b cells but, in contrast to cells in cluster DA-a and DA-c, pushes cells away from bistability. The data from ISI histogram might suggest a possible shift in preferred frequency ranges, but a detailed experimental investigation has to be undertaken to unravel specific effects of DA on resonance properties of bursting pyramidal cells.

4.3 Morphometric Analysis

22 recorded neurons were filled with biocytin, fixed and their morphology was visualized by a Streptavidin-Alexa 488 Fluorophore conjugate. Confocal image stacks were acquired on a Zeiss LSM510 confocal microscope using a 10x Apochromat objective. Combined image stacks were then imported into Neurolucida and the cell morphology was reconstructed by manually tracing the neuron in the image stack. All reconstructed neurons were analysed with the Neurolucida NeuroExplorer analysis tool, which has multiple analysis methods readily implemented (see Methods). The results of these morphometric measures were exported to spreadsheets (OpenOfficce.org) and imported into the Matlab environment for further analysis. Some variables were excluded after careful evaluation: I have excluded x-y and z angles since they describe angles in a relative coordinate system that depends on slicing and imaging of the cell. I have also excluded the soma convexity since only discrete values were observed, which is probably due to an error in the calculation method. All diameter based variables (except for the soma) were excluded, since the limited resolution of the acquired image stacks (voxel dimension: x: 0.82, y: 0.82, z: 0.80 μm) would not allow reliable diameter measurements, especially for fine distal dendrites.

Figure 4.22 shows the results of the cluster analysis based on the first 3 principal components calculated from the remaining morphometric variables. The dendrogram shows that morphologies of recorded cells can be divided into 3 clusters, which have been colour coded in the dendrogram. The largest cluster contains 13 cells and will be referred to as cluster M-a (light green in the dendrogram). The distances between individual cells within the cluster are relatively small, although the dendrogram might suggest two subgroups with the cluster, but the data matrix (displayed below) does not indicate a distinct separation between subgroups. The second largest cluster includes 6 cells (dark green in the dendrogram) and will be referred to as cluster M-b. This cluster is identical to previously established clusters IB and DA-b, with one cell (#ID 17) added. This cell has been classified as an IM cell based on control data regulation, and was classified as single cluster in the DA dataset. Within this cluster there is a larger distance between two groups of 3 cells each, which might point towards subgroups within this cluster. The last cluster comprises 3 cells and has rather large inter-cell distances, i.e. this group of cells is rather heterogeneous in morphology, but is more similar to cluster M-a than to cluster M-b. This third cluster will be referred to as cluster M-c.

The results of the pre-cluster analysis PCA were used to determine variables that contributed to separating cells in the morphology based parameter space. Figure 4.23 depicts the summary of the PCA results. Notably, there is no steep decrease in explained variance for principal components in the scree plot (Figure 4.23 B), as expected to be seen for a faithful

dimensionality reduction. The explained variance for the first 3 PCs sums only up to 47% of the total variance in the dataset. Despite this low sum of explained variance cluster analysis was based only on the first 3 PCs, since including of up to 7 PCs (74% of total variance) did not change the results of the cluster analysis qualitatively (not shown). As seen in the 3D biplot, cells separate well in the reduced parameter space of the first three PCs (Figure 4.23 B). The variables with the highest positive and negative factor loading are indicated as vectors in the biplot.

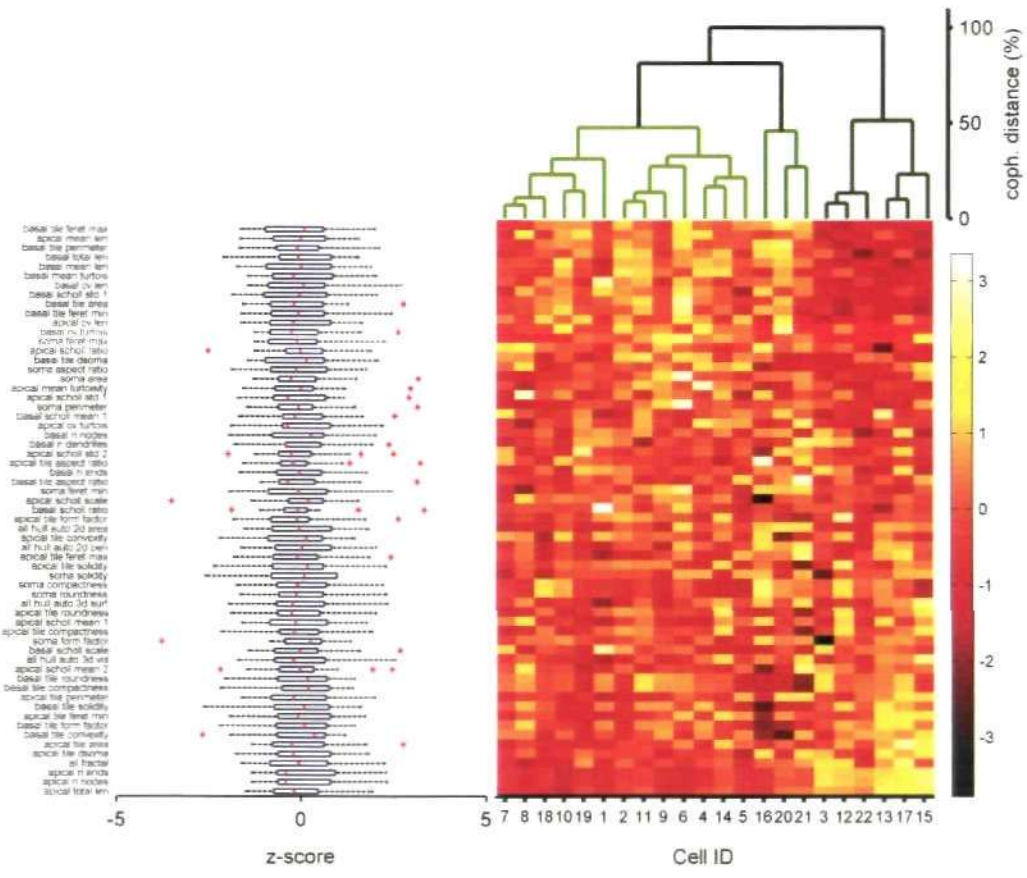

Figure 4.22 | Cluster analysis of morphometric variables
Top) Dendrogram of linkage obtained by Ward's method based on Euclidean distances between z-scores of all morphology variables. Bottom, left) Box plot of z score transformed morphology variables, rows sorted by mean values of cluster M-b (dark green). Bottom, right) Colour coded matrix of z scores, columns sorted according to dendrogram.

Figure 4.23 C shows the six variables with the highest factor loading for each PC in a bar plot, where colours of the bars correlate to the vectors in the biplot. Here it appears that the first principal component distinguishes mainly between properties of the basal dendrite and the apical dendrite. In particular, positive factor loadings correlate to variables describing properties

of the tile analysis applied to the basal dendrite ([*basal tile perimeter*], [*basal tile feret max*]), i.e. the area covered by the basal dendrite. The mean length of a basal dendritic section [*basal mean len*] has the third highest factor loading for PC1, which is indirectly linked to the area covered by the basal dendrite. Variables that relate the 'complexity' of the apical dendrite reach the highest factor loadings for PC1, i.e. the total length of the apical dendrite [*apical total len*], the number of apical dendrite endings [*apical n ends*] and the number of apical branch points [*apical n nodes*].

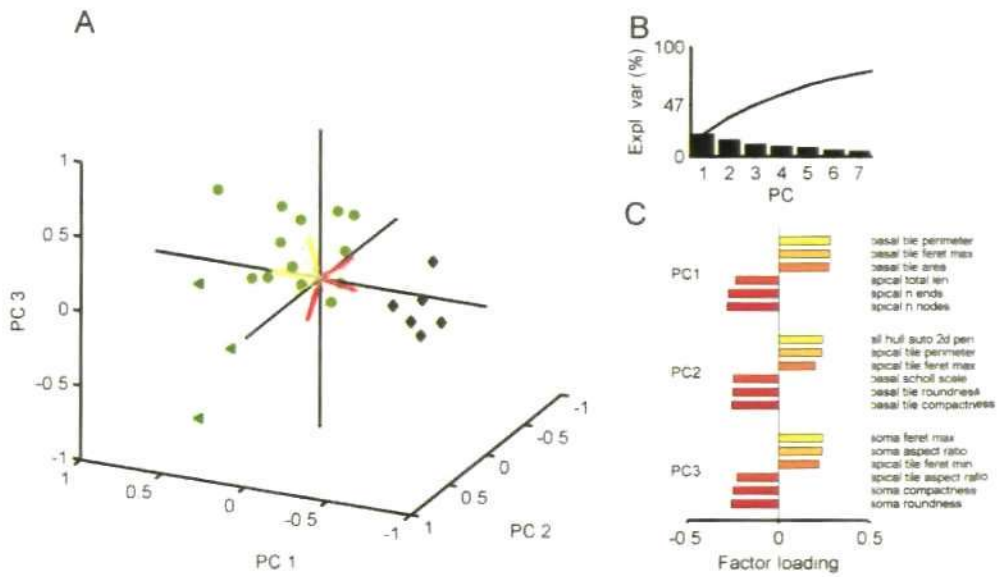

Figure 4.23 | Summary of pre-cluster PCA
A) Scatter plot cell positions within coordinates of the first 3 PCs, cells are labelled according to subsequent clustering. Variables with the highest factor loading for each PC are indicated as vectors, colour coded according to C. B) Scree plot of explained variance per principal component (bars) and cumulative sum (line). The first 3 PCs explain 47% of the total variance. C) Bar plot of 6 variables with the highest factor loading for PCs 1-3.

Variables with high positive factor loadings in PC2 relate to shape factors of the apical dendrite or the whole neuron dendrite. The perimeter of an automatically constructed 2-dimensional hull [*all hull auto 2d peri*] has the highest positive factor loading followed by the perimeter of the apical tile [*apical tile perimeter*] and the maximum Feret diameter of the apical tile [*apical tile feret max*]. Negative factor loadings in PC2 are shown by variables that describe basal dendrite properties. In detail variables that describe form factors of the basal dendrite tile have the highest loading, i.e. the roundness [*basal tile roundness*] and compactness [*basal tile compactness*] of the basal tile. Additionally, the scaling of the Gaussian fit to results of the Sholl analysis [*basal sholl scale*] has the third highest factor loading. This scaling factor is needed to scale the bimodal fit to normal distributions with probabilities ranging from 0 to 1, hence it is proportional to the total number of counts.

The highest factor loadings for PC3 are reached mainly by variables describing size and form of the soma, with the exception of one apical variable. The highest positive loadings are achieved by the maximum and the minimum Feret diameter of the soma [*soma feret max, soma feret min*] and the aspect ratio of the soma. High negative factor loadings of PC3 include form factors of the soma, i.e. the roundness [*soma roundness*] and the compactness [*soma compactness*] but also the aspect ratio of the apical tile [*apical tile aspect ratio*].

Overall, the PCA successfully separates different aspects of somato-dendritic morphology. There is high presence of apical and basal variables in the first two PCs indicating the highest variance in the dataset is present in dendritic morphology. To a lesser extend, somatic properties contribute to variability in morphology.

The properties of the obtained clusters become more obvious when plotting the morphologies ordered by the cluster solution (Figure 4.24). In this plot the complexity of dendritic arbours increases from cells placed on the left towards cells on the right side of the figure. The 3 cells in cluster M-c (left, medium green box) have simple apical dendrites that show only few arborisations, especially towards superficial layers, although not distinctively different from cells in cluster M-a. Instead these cells seem to have a somewhat skewed basal dendrite. In contrast, cells in the largest cluster (M-a, light green box, middle) show a range of complexity in apical dendrites, where cells at the top have less complex apical dendrites but complexity increases towards the bottom of the box. Also, the basal dendrite seems slightly more elaborated when compared to cells in cluster M-c. Cells in cluster M-b exhibit the most complex dendritic arbours with complex elaborated apical dendrites, especially when reaching superficial layers (tufted apical dendrite). The apical dendrite also shows multiple arborisations at the proximal half near the soma. The basal dendrite appears more complex compared to cells in the other cluster, but also more compact and less extended, i.e. the span of the apical tuft is larger than the span of the basal dendrite.

To determine variables that bear statistically significant differences between clusters, unequal sample size one-way ANOVAs were calculated separately for each variable, using the cluster as independent variables (Table 4.5). Individual significance between clusters was tested by a post-hoc Tukey-Kramer test. Out of 61 variables included, 30 showed significant effects ($F>3.5$, $p<0.05$) between cluster. For the sake of clarity and briefness I will only describe these most significant effects.

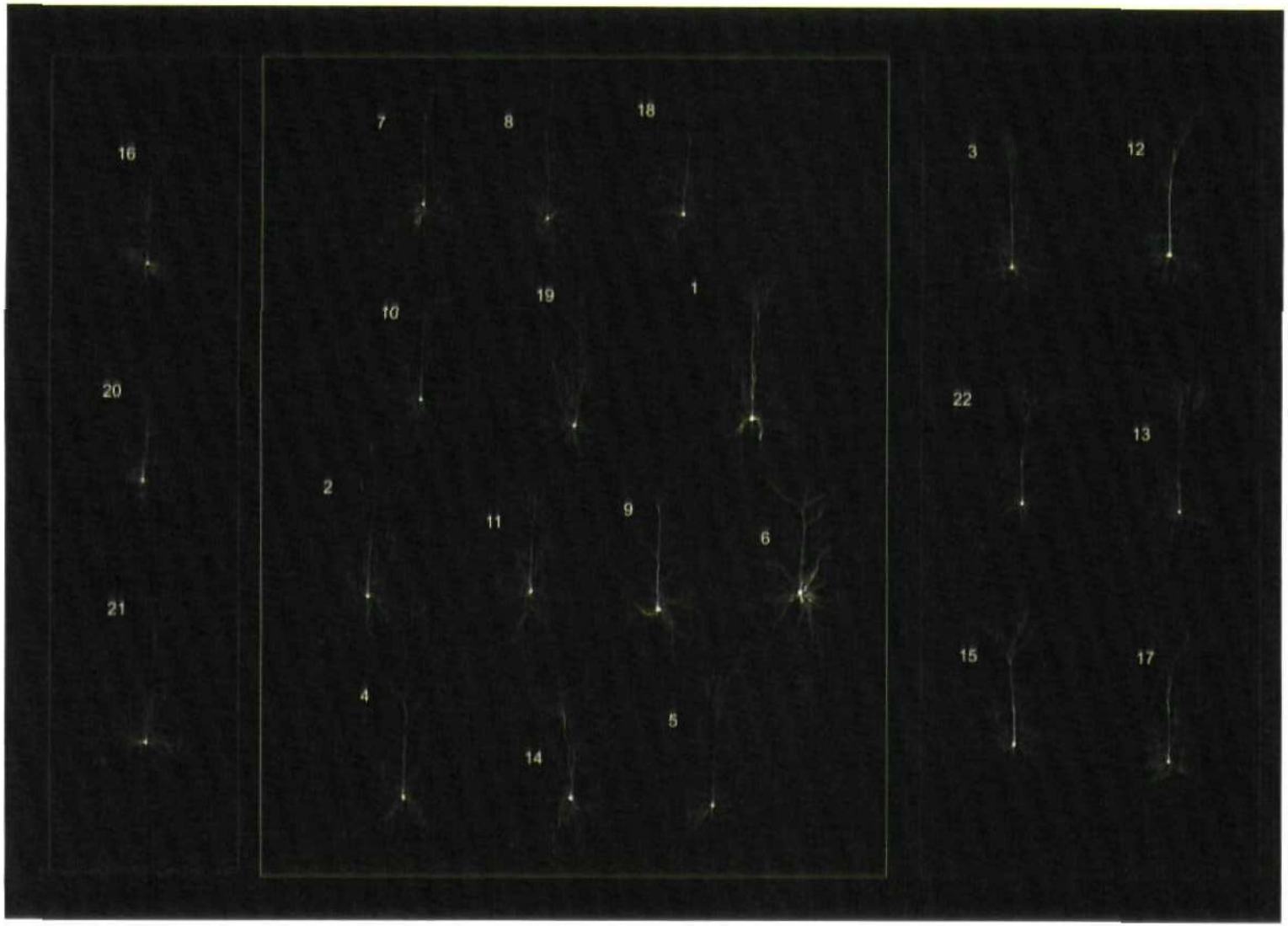

Figure 4.24 | Morphologies of recorded neurons grouped by clustering results. Somatodendritic morphology of recorded cells sorted by clustering based on morphology variables. Left) Cluster M-c (medium green box), Middle) cluster M-a (light green box), cluster M-b (dark green box).

Significant variables describing apical and basal dendrites can be separated into those describing the size and shape of the area covered by the dendrite and variables describing mean properties of individual sections. Properties of apical sections best distinguish cluster M-b compared to M-a/M-c. Indeed some of the highest F values are obtained by apical section variables, where cluster M-b clearly stands out with a higher average number of apical nodes [*apical n nodes* = 38.33 ±1.76, F=51.41, p=2.16e-8] and ends [*apical n nodes* = 40.17 ±1.85, F=50.21, p= 2.60e-8], longer total apical length [*apical total length* = 6647 ±353 µm, F=23.05, p=8.30e-06] but a lower mean section length [*apical mean length* = 84.86 ±4.037 µm, F=8.22, p=0.0027]. The apical dendrite of M-b cells also covers a greater area [*apical tile area* = 1.19e5±1.0e4 μm^2, F=5.06, p=0.017]. Figure 4.25 shows example morphologies for each of the obtained morphological cluster. Here the difference in apical dendrite morphology between M-a and M-b cluster cells becomes clear. Cell #4 has a slimmer apical dendrite and fewer branches when compared to cell # 22.

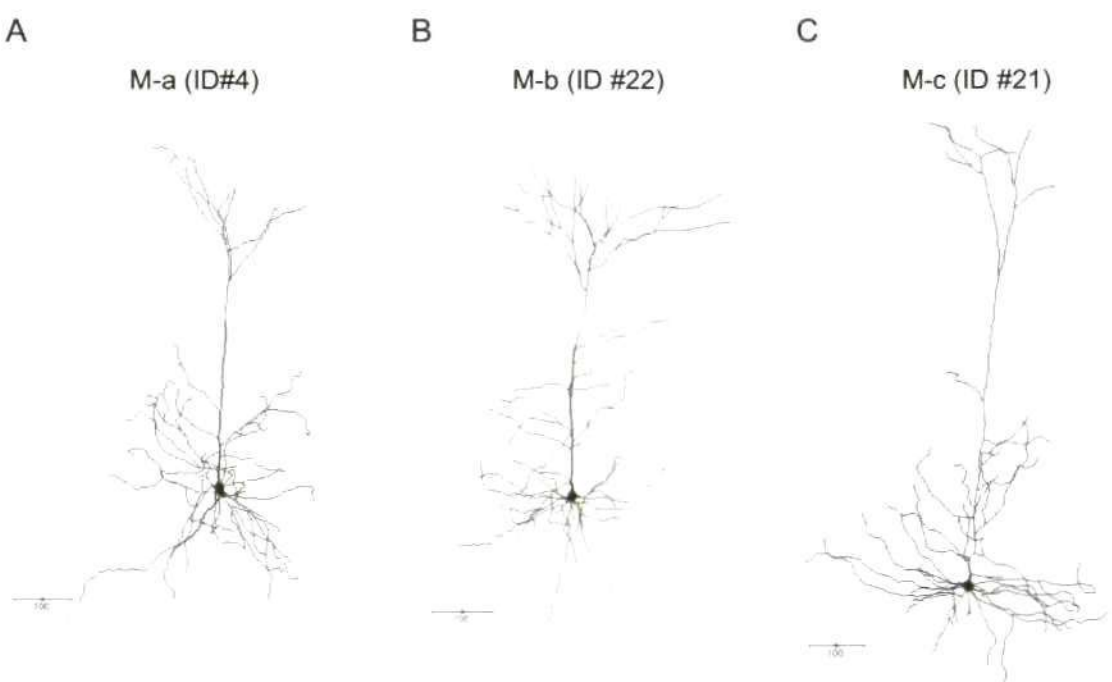

Figure 4.25 | Example morphologies from the established morphological cluster.
A) Morphology of cell #4, cluster M-a. Notice the slimmer apical dendrite and rather round appearance but wider extend of the basal dendrite. B) Morphology of cell #22, cluster M-b. The apical dendrite occupies a larger area and has more arborisations, whereas the basal dendrite is more compact when compared to M-a cells. C) Morphology of cell #21, cluster M-c. This cell has a longer apical dendrite which is similar in complexity to M-a cells, but the basal dendrites extend mainly in perpendicular directions to the apical dendrite.

Notably some variables describing form factors of the apical dendrite might also distinguish cluster M-a from clusters M-b/M-c. Cells in cluster M-c have a longer apical tile perimeter

[*apical tile perimeter* = 2600 ±206.4 μm, F=4.60 p=0.024], greater aspect ratio [*apical tile aspect ratio* = 2.687 ±0.242, F=4.45, p=0.026] and a greater maximum Feret diameter [*apical tile feret max* = 786.6 ±48.63 μm, F=4.23, p=0.030], compared to clusters M-a/M-b. This can be seen in Figure 4.25, where the longer apical is seen in the comparison to both M-a and M-b cells (images are scaled to match scale bars).

When comparing effects for basal dendrite variables, size of area variables and section variables generally best distinguish cluster M-b vs. M-a/M-c. Here M-b cells have a shorter the basal tile perimeter [*basal tile perimeter* = 1034 ±82.83 μm, F=15.33, p=0.00011], smaller tile area [*basal tile area* = 55110 ±8667 μm^2, F=8.49 p=0.0023], a lower mean section length [*basal mean length* = 75.15 ±4.00 μm, F=11.81 p=0.00046] and total basal dendrite length [*basal total length* 3425 ±302 μm, F=6.49, p=0.0071]. Again these differences are seen by eye when comparing the example morphologies in Figure 4.25.

One distinct exception from the similarity between M-a and M-c is the maximum Feret diameter of the basal tile [*basal tile feret max*, F=25.70, p=3.94e-06], which was found to be the only variable significantly different between all clusters. M-b cells have the lowest maximum Feret diameter [*basal tile feret max* = 358.1 ±19.67 μm] followed by M-a cells [*basal tile feret max* = 495 ±13.37 μm] and M-c cells [*basal tile feret max* = 579.8 ±27.82 μm]. In addition, M-b cells have smaller CV in section length [*basal cv length* = 0.83 ±0.036 F=6.25, p=0.0082], lower turtoisity of sections [*basal mean turtoisity* = 1.123 ±0.014 F=4.46, p=0.026] and a smaller width in the unimodal fit to Sholl analysis results [*basal sholl std 1* = 52.12 ±5.684 μm, F=4.26, p=0.030] compared to M-a cells.

Variables that best distinguish M-c vs. M-a/b cells describe form factors of the basal dendrite tile. The basal tile of M-c cells has a smaller form factor [*basal tile form factor* = 0.36 ±0.05, F=12.24, p=0.00038], solidity [*basal tile solidity* = 0.67 ±0.04, F=9.53, p=0.0014], compactness [*basal tile compactness* = 0.57 ±0.034, F=9.43, p=0.0014] and roundness [*basal tile roundness* = 0.32 ±0.047, F=8.31, p=0.0026]. Also, an automatically generated 2-dimensional hull applied to the whole neuron dendrite differs in area [*all hull auto 2d area* = 3.6e5 ±2.16e3 μm^2, F=7.16, p=0.0048] and perimeter [*all hull auto 2d peri* = 2441 ±75.72 μm, F=6.02, p=0.0094] between M-c cells and M-a/M-b cells. A weaker effect can also be seen for the soma aspect ratio, which is smaller for M-c cells [*soma aspect ratio* = 1.163 ±0.067, F=4.10, p=0.033] compared to M-a cells.

In summary, size of dendritic area and section features are most different between clusters M-a and M-b, where M-b cells cover a greater apical area with a greater number of nodes and sections, but smaller basal area and smaller total length of basal dendrite. The small M-c cluster differs from M-a/M-b cells mainly in the shape of the basal dendrite, with lower values for

shape factors such as roundness, solidity and compactness. These lower values describe the basal dendrites as further away from an ideal circle, indicating a asymmetric spatial field of the basal dendrite.

Table 4.5 Mean values of morphology cluster

	Cluster			ANOVA	
	M-a (n=13)	M-b (n=6)	M-c (n=3)	F	p
apical n nodes	**17.85 ±1.14***	**38.33 ±1.68***	22.67 ±2.37	51.41	2.16e-08
apical n ends	**19.08 ±1.18***	**40.17 ±1.74***	24.33 ±2.47	50.21	2.60e-08
basal tile feret max	**495 ±13.37***	**358.1 ±19.67***	**579.8 ±27.82 ***	25.70	3.94e-06
apical total len	**3837±232.6***	**6647 ±342.3***	4748 ±484.1	23.05	8.30e-06
basal tile perimeter	**1486 ±56.27***	**1034 ±82.83 ***	1747 ±117.1	15.33	0.00011
basal tile form factor	0.56 ±0.02	**0.65 ±0.03***	**0.36 ±0.05***	12.24	0.00038
basal mean len	**96.63 ±2.72***	**75.15 ±4.00***	102 ±5.67	11.81	0.00046
basal tile solidity	0.8223 ±0.019	**0.8817 ±0.029***	**0.6667 ±0.040***	9.53	0.0014
basal tile compact	0.7123 ±0.0162	**0.7383 ±0.024***	**0.5667 ±0.034 ***	9.43	0.0014
basal tile area	**98240 ±5888 ***	55110 ±8667	86990 ±12260	8.49	0.0023
basal tile round	0.51 ±0.022	**0.55 ±0.032***	**0.32 ±0.047***	8.31	0.0026
apical mean length	**104.6 ±2.743 ***	84.86 ±4.037	100.5 ±5.71	8.22	0.0027
hull auto 2d area	2.69e5 ±1.0e4	**2.88e6 ±1.52e4***	**3.6e5 ±2.16e4***	7.16	0.0048
basal total length	**4533 ±205***	**3425 ±302 ***	5078 ±427	6.49	0.0071
basal cv len	**0.967 ±0.023***	**0.83 ±0.036***	0.994 ±0.049	6.25	0.0082
hull auto 2d peri	2150 ±36.38	**2200 ±53.54 ***	**2441 ±75.72 ***	6.02	0.0094
basal tile feret min	**341.8 ±17.34 ***	243.4 ±25.53	320.7 ±36.1	5.12	0.017
apical tile area	**82000 ±6858***	119500±10090	81260±14280	5.06	0.017
Fractal dim	**1.149 ±0.006***	1.182 ±0.009	1.173 ±0.012	4.95	0.019
apical tile peri	2001 ±99.13	2375 ±145.9	**2600 ±206.4 ***	4.60	0.024
apical scholl ratio	0.679±0.029	**0.561±0.042***	0.767 ±0.060	4.51	0.025
basal mean turtoisity	**1.173 ±0.009 ***	1.123 ±0.014	1.151 ±0.020	4.46	0.026
apical tile aspect	1.967 ±0.1162	**1.84 ±0.1711 ***	**2.687 ±0.242 ***	4.45	0.026
basal scholl std 1	**70.78 ±3.861 ***	52.12 ±5.684	74.13 ±8.038	4.26	0.030
apical tile feret max	640.1 ±23.36	709.5 ±34.38	**786.6 ±48.63 ***	4.23	0.030
soma aspect ratio	1.372 ±0.032	1.3 ±0.047	**1.163 ±0.067 ***	4.10	0.033
apical tile d soma	240.9 ±11.13	284.4 ±16.38	295.6 ±23.16	3.76	0.042
basal tile convexity	0.9062 ±0.013	**0.9333 ±0.020 ***	0.84 ±0.028	3.71	0.044
apical tile compact	0.5038 ±0.019	**0.5467 ±0.028***	0.4167 ±0.039	3.68	0.045
apical cv length	**0.818 ±0.015 ***	0.7484 ±0.022	0.7826 ±0.031	3.55	0.049

Significant variables from separate one-way ANOVA (non-equal sample size)
post-hoc Tukey-Kramer test ($p<0.005$) : * M-a vs M-c #M-b vs M-a ◊ -M-c vs M-b.
See Methods for appropriate units.

Discussion of morphology based clustering

The PCA based cluster analysis of morphological structure presented here has identified at least two distinct populations of deep layer pyramidal cells based on quantitative morphological parameters: a complex cell population with a wide apical tuft and small basal dendritic area and a heterogeneous population of cells with wide, symmetric basal dendrite but variable apical tufts.

The results of this analysis agree with previously reported qualitative morphological properties of deep layer pyramidal cells, which were originally classified into two main groups based on somatodendritic morphology, projection site, and physiology (Hallman et al., 1988; Chagnac-Amitai et al., 1990; Larkman and Mason, 1990; Mason and Larkman, 1990; Kasper et al., 1994): Type I neurons have thick tufted apical dendrites and are more likely to exhibit bursting, and project to the superior colliculus, the spinal cord, the basal pons or the striatum. In contrast, Type II neurons have slender apical dendrites, mostly show regular spiking behaviour, and project either to contralateral cortical sites or the ipsilateral striatum. This basic characterisation has been proven to be useful, but is certainly oversimplified.

To my knowledge this is the first quantitative study on deep layer pyramidal cell morphology in the rat PFC. Previous studies that report qualitative morphological features of prefrontal deep layer pyramidal cells have shown similar classifications, where a thicker apical dendrite and more complex dendritic arborisation was associated with bursting behaviour (Yang et al., 1996; Degenetais et al., 2002; Otsuka and Kawaguchi, 2008).

Other studies have focussed on classifying morphology and electrophysiology of prefrontal pyramidal cells based on their projection targets. For example Morishima and Kawaguchi (2006) have used retrograde tracing methods to selectively label subpopulations of deep layer prefrontal pyramidal cells. Injection of fluorescent tracer into the pons and the striatum revealed non-overlapping populations of deep layer pyramidal cells. Corticostriatal cells were morphologically heterogeneous especially with regard to their apical tuft structure as opposed to corticopontine neurons which appear to be more homogenous, but distinctly different in dendritic morphology. It is likely that these two populations have been sampled in the current study, where M-b cells would correlate with corticopontine neurons and M-a cells correlate with corticostriatal/callosal cells. Thus morphological characteristics are correlated with projection targets, as demonstrated for other cortices (Gao and Zheng, 2004; Hattox and Nelson, 2007), and dendritic structure can be used as indicator of projection target, if such information is not available. In Morishima and Kawaguchi (2006) whole cell patch clamp recordings revealed that corticopontine neurons preferably exhibit bursting whereas corticostriatal/callosal neurons exhibit regular spiking patterns. More interestingly, using dual cell recordings they showed that

corticostriatal cells with similar morphology are more likely to be synaptically connected. Also, corticostriatal/callosal neurons are more likely to be non-recurrently connected to corticopontine neurons than to neurons of their own type. Hence morphologically defined sub-networks might exist in the rat prefrontal cortex where bursting, complex apically arborised pyramidal cells integrate information from corticocortical and corticostriatal networks.

One other recent study described a distinct morphological phenotype in the prefrontal cortex of ferrets (Wang et al., 2006). This phenotype showed a characteristic proximal split of the apical dendrite and showed a higher number of dendritic apical and dendritic arborisations. Hence it was termed 'complex pyramidal cell', as opposed to the 'simple pyramidal cell' which is the main cell type found in the visual cortex. The complex pyramidal cell was reported to be the major cell type in the ferret prefrontal cortex (89%) and to be distinct in terms of connectivity and synaptic plasticity. In this study out of 22 reconstructed cells, 4 cells (IDs: 1, 14, 19, 20) had a similar early split in the apical dendrite. These cells were all classified into cluster M-a/M-c, together with other cells lacking such a feature. In Wang et al. (2006) only few quantitative morphological measurements were reported, but most significant was the total length of apical dendrite which was reported to be ~6108 ±744 μm (Suppl. Information in Wang et al., 2006). These values are much closer to cells in cluster M-b [*apical total len* = 6647 ±353 μm] although no proximal split of apical dendrites exists. Simple cell values were reported to be 3025 ±1100 μm (Wang et al., 2006) which agree with values obtained for cluster M-c [*apical total len* = 3603 ±386 μm]. Thus, deep layer pyramidal cells in the adult rat seem different from those observed in ferrets, although some overlap exists. Cells with proximal apical split exist, but do not seem to form a defined cell type, neither based on morphology nor physiology.

Other studies have used cluster analysis successfully for unbiased morphological classification of cortical interneurons (Cauli et al., 2000; Kozloski et al., 2001; Krimer et al., 2005; Dumitriu et al., 2007) and pyramidal cells (Tsiola et al., 2003). One recent study has employed hierarchical clustering to characterise deep layer pyramidal cell morphologies in the visual cortex of mice (Tsiola et al., 2003). They described five main classes of pyramidal cells, where the typical large pyramidal cell (with apical dendrite extending to superficial layers) constituted only one distinct cluster. Other cluster were formed by cells with polarised and short dendrites, cells with narrow dendritic arbours, small pyramidal cells with small dendrite and soma, and atypically oriented pyramidal cells. The cluster containing large pyramidal cells was divided into two subgroups mainly due the size of their apical tufts, i.e. wide and narrow-tufted tall pyramidal cells. The identified groups in the current study relate to subgroups of tall pyramidal cells described by Tsiola et al. (2003). Cluster M-a possibly relates to Tsiola et al.'s narrow-tufted pyramidal cells, whereas cluster M-b relate to tall wide-tufted pyramidal cells. Yet, Tsiola et al.'s wide tufted pyramidal cells seem less complex than cells found in cluster M-b, which is

in line with the view that pyramidal cell complexity (e.g. number of spines and dendrites) is increased in prefrontal areas, as discussed above (Elston, 2003b; Wang et al., 2006). Furthermore, Tsiola et al. (2003) report one cell type that has asymmetric basal dendrites which they referred to as 'narrow pyramidal cells'. This cell type might correlate with cluster M-c, but because of the low number of cells that form cluster M-c, this conclusion is rather speculative.

Altogether the current analysis demonstrates the existence of morphological subpopulations in deep layer pyramidal cells of the rat PFC.

4.4 Pyramidal cells in a combined feature space

To achieve a classification of pyramidal cells in a combined feature space formed by physiology and morphology variables, I have performed a HCA using the first principal component of the electrophysiological data obtained under control condition and the first principal component from the morphological dataset. Figure 4.26 A shows the resulting dendrogram after HCA. Here four very compact cluster emerge. Figure 4.26 B shows a scatter plot of cell positions plotted in coordinates spanned by intrinsic (PC1 Electrophysiology Control) and morphological (PC1 Morphology) properties. I have computed single one-way ANOVAs on selected variables, using the EM cluster as independent variable, to determine where differences between clusters stem from. Table 4.6 presents results from those ANOVAs that describe some of the most significant differences between the obtained cluster.

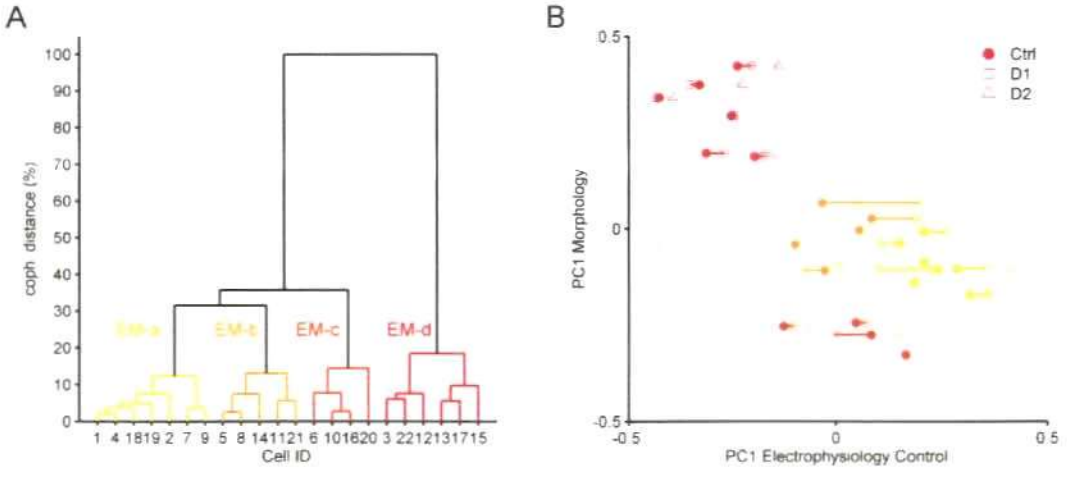

Figure 4.26 | HCA of principal components from physiology and morphology
A) Dendrogram depicting results from HCA of PC1 from both morphology and physiology.
B) Scatter plot of cells (•) in coordinates spanned by PC1 of morphology variables and PC1 of control electrophysiology variables. Values for dopamine modulated cell parameters are added through out-of-sample extension of DA datasets, D1: □, D2: △. To illustrate changes from control to DA modulated condition, control data are connected through lines to their respective D1 dataset (solid line) and D2 dataset (dashed line).

The most distinct cluster is cluster EM-d (red). It is identical to cluster M-b which, as discussed above, corresponds to bursting cells (cluster IB). The cells are well separated on both principal component axes from all other cells, which is in agreement with cluster analyses shown above. When computing one-way ANOVAs with multiple comparison tests (Tukey-Kramer), the two variables with the highest F values are the y-intercept for the square root fit to spike latency [$b(1/ISI_0)$] and the number of apical ends [*apical n ends*]. Both are significantly higher when compared to all other cluster (Table 4.6). This is in line with cluster solutions presented in

previous sections, where bursting cells have always been classified as separate groups in all datasets (i.e. control electrophysiology, DA modulated, and morphology).

Non-IB cells are split into three cluster, of which the largest one contains 7 cells (EM-a, yellow). These cells are drawn exclusively from the previous RS/M-a cluster. This cluster appears to be very similar in morphology to next biggest cluster EM-b (n=5, light orange) as seen in their very similar positioning on the morphology axis in Figure 4.26 B. Thus differences in intrinsic properties must explain the split into two separate clusters. When comparing this cluster solution with the clustering results from the sections above (Figure 4.27), it appears that EM-b consists of four RS and one IM cell of control condition cluster. Results from one-way ANOVAs give insight into where differences between EM-a and EM-b stem from. Indeed, only 3 electrophysiology variables are significantly different between EM-a and EM-b, the input resistance [*R(in)*], and the two coefficients for the square root fit to steady state ISI's [*a(ISI,eq)*, *b(ISI,eq)*]. For example EM-a cells have a higher input resistance [*R(in)* = 107.8 ±4.7 MΩ], compared to EM-b cells [*R(in)* = 83.45 ±5.6 MΩ]. Since the standard deviation in these clusters is much smaller compared to the values from cluster RS [*R(in)*, RS: 99.10 ±16.10 MΩ] and IM [*R(in)*, IM: 70.70 ±14.87 MΩ], the current clustering seems to have found more homogenous groups within non-IB cells.

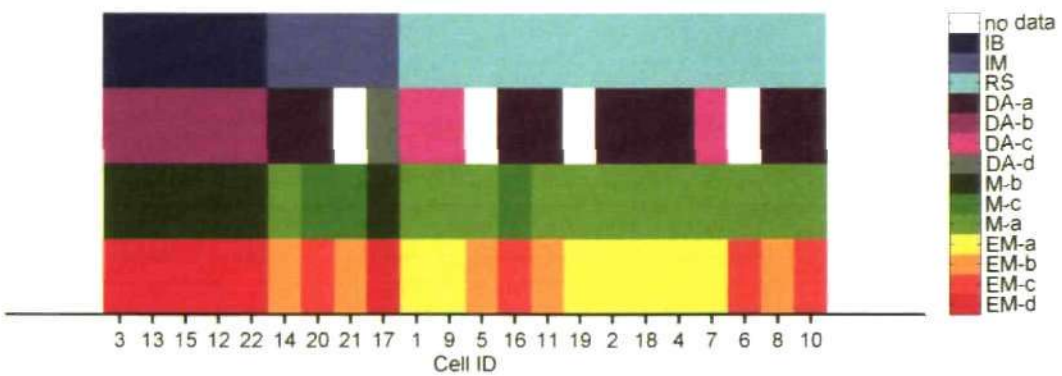

Figure 4.27 | Comparison of all cluster solutions
Comparison of cluster solutions for different datasets. Here IB cells show up as distinct cluster in all datasets (although cell 17 has been classified as IM cell based in control physiology variables). Non-IB cells are more heterogeneous and possible subpopulations based on morphology, DA modulation and in the combined parameter space might exist.

Cluster EM-c is comprised of 2 IM cells (M-c) and two RS cells (M-a) in the control condition (morphology) cluster (Figure 4.27). In the principal components axes these cells are mainly separated by morphology variables from the larger cluster EM-a and EM-b, whereas physiological properties are similar. Indeed variables describing the basal dendrite are those that show the highest significant differences, as established by separate one-way ANOVAs. The

basal tile perimeter [*basal tile peri* = 1861±72 µm] and the basal maximum Feret diameter [*basal feret max* = 416.8±24 µm] is significantly larger compared to all other clusters (Table 4.6). Standard deviations for basal tile perimeter of cluster EM-c are smaller when compared to morphological cluster [*basal tile perimeter*, M-a 1486 ±56.27 µm, M-c 1747 ±117.1 µm] but not for the basal maximum Feret diameter [*basal max feret*, M-a:495 ±13.37 µm, M-c: 579.8 ±27.82 µm]. Thus, cluster EM-c appears, at least for a subset of variables, more homogenous compared to clustering based on morphology alone.

DA modulation projected into control parameter space

I did not include the dopaminergic data into the current HCA, since no data was available for four cells. Instead, I used out-of-sample extension to plot the respective DA modulated datasets into the PC coordinates in Figure 4.26 B. Out-of-sample extension is simply achieved by using the coefficients for the transformation of the control dataset into principal components, and apply them to the datasets obtained with dopaminergic agonists. These changes are indicated as horizontal lines between the control (full circles), D1 (solid line, open squares) and D2 (dashed line, open triangle) condition in Figure 4.26 B.

Table 4.6 | Selected ANOVAs of EM cluster

	Cluster				ANOVA	
	EM-a	**EM-b**	**EM-c**	**EM-d**	$F_{(3,18)}$	**p**
b(ISI$_0$)	-23.07 ±3.0^{d}	-35.38 ±3.6^{d}	-33.13 ±4.0^{d}	-69.52 ±3.2^{a,b,c}	38.61	4.76e-8
apical n ends	19.29 ±1.7^{d}	22 ±2.0^{d}	19 ±2.3^{d}	40.17 ±1.8^{a,b,c}	27.82	5.62e-7
basal tile perimeter	1441 ±54^{c,d}	1405 ±64^{c,d}	1861 ±72^{a,b,d}	1034 ±58^{a,b,c}	26.64	7.71e-7
R(in)	107.8 ±4.7^{b,d}	83.45 ±5.6^{a,d}	87.74 ±6.2^{d}	56.15 ±5.1^{a,b,c}	18.25	1.08e-5
a(ISI$_\infty$)	0.69 ±0.14^{b,d}	1.55 ±0.17^{a}	1.34±0.19^{d}	2.17 ±0.15^{a,b,c}	15.71	2.87e-5
basal tile feret min	317.2 ±18^{c}	303.7 ±21^{c}	416.8 ±24^{a,b,d}	243.4 ±19^{a,b,c}	10.48	0.0003

Selected one-way ANOVAs with post-hoc Tukey-Kramer test ($p<0.05$). a: significant against cluster EM-a, b: significant against cluster EM-b, c: significant against cluster EM-c, d: significant against cluster EM-d. See Methods for appropriate units.

This comprehensively illustrates the changes introduced by DA agonists on physiological variables. Cells in cluster EM-d (IB) seem to react similarly to both D1 and D2 receptors, where bursting cells seem to get closer to non-IB cells on the physiology axis. This is line with the observed effects, described in the previous analysis of the DA dataset, where for example D1 or D2 stimulation reduce the rheobase current (for an upward current ramp injection) of bursting cells, i.e. bringing it closer to values seen in non-bursting cells (Table 4.4).

For non-IB cells DA effects seem more variable, with D1 effects being mostly stronger (longer solid lines), but with some cells exhibiting very strong D2 effects (dashed lines). Here it can be seen that all cells forming the DA-c cluster (cells exhibiting strong D2 effects) were assigned to cluster EM-a (Figure 4.27). This demonstrates the possibility of a subpopulation of pyramidal cells expressing high levels of D2 receptors, as discussed above (Section 4.2).

Discussion of EM clustering

The clustering of pyramidal cells in a combined feature space revealed two main results. Firstly, intrinsically bursting neurons present a very distinct cell population that differs in many variables to all other recorded pyramidal cells. Secondly, non-bursting cells are rather heterogeneous, and different datasets (as described in the sections above) lead to different groupings of cells.

In IB cells the correlation between morphology and electrophysiology is very high. This is manifest in their consistent appearance as a cluster in analyses of separate datasets (control electrophysiology, DA and morphology) and is confirmed through clustering in the combined feature space. In contrast, correlation between electrophysiology and morphology seems less pronounced in non-bursting cells. Here, classifying cells based on both electrophysiological and morphological variables might present an advantage, where clustering reveals less obvious correlations between physiology and morphology.

Extensive work has been dedicated to reveal the impact of dendritic morphology on physiological properties of neurons. Since the groundbreaking theoretical work of Rall in the 1950's and 1960's (Rall, 1959; Rall et al., 1995), there is a large body of experimental and theoretical evidence, that dendritic morphology critically shapes synaptic inputs, affecting neuronal signal integration and the generation of somatic action potentials (Stuart et al., 2000). In particular, the relationship between dendritic morphology and bursting has received special attention. The correlation between bursting and cell morphology has been described qualitatively by the first studies to report bursting in deep layer pyramidal cells (Connors et al., 1982; Chagnac-Amitai et al., 1990; Connors and Gutnick, 1990; Larkman and Mason, 1990). Later Mainen & Sejnowski (1996) demonstrated how increased complexity of the dendritic tree

alone, can give rise to various firing patterns in biophysical model neurons, including bursting behaviour. Although there is more experimental evidence for the influence of dendritic structure on neuronal firing patterns (Kasper et al., 1994; Mel, 1994; Bastian and Nguyenkim, 2001), further studies have shown that a variety of mechanisms can induce bursting, even in regular spiking neurons, for example through appropriate dendritic stimulation (Larkum et al., 1999; Williams and Stuart, 1999; Lemon and Turner, 2000). Moreover, active conductances in dendrites modulate transmission of synaptic signals to the soma and have critical impact on elicited firing patterns (Häusser et al., 2000). Thus, not only the structure of dendrites, as captured in the current analysis, but also their equipment with voltage gated channels contributes to differences in firing patterns and ultimately input-output functions (Reyes, 2001).

To this end, the current analysis shows that correlations between biophysical properties, input-output functions and morphology are robust in bursting cells, but harder to detect in non-bursting cells. In this respect, multivariate analysis including parameters from both physiology and morphology will most likely improve the detection of these correlations, and more truthfully detect similarities between cells, but given the greater variability in non-bursting cells, larger datasets are needed to reliably identify sub-populations in deep layer pyramidal cells of the rat PFC.

5 Final Discussion and Outlook

The current study has for the first time presented a quantitative analysis of electrophysiological and morphological properties of deep layer pyramidal cells in the adult rat PFC.

The analysis showed distinct clusters of pyramidal cells in a parameter spaces spanned by intrinsic biophysical properties, dopaminergic modulation, morphology or in a combined feature space. These clusters point towards distinct subclasses within prefrontal deep layer pyramidal cells. Moreover, cluster in obtained different parameter spaces overlap which highlights the correlation between electrophysiology and dendritic structure.

The most distinct subpopulation consists of intrinsically busting (IB) cells that fire repetitive bursts of action potentials upon low intensity stimulation. They show a low input resistance and fast membrane time constant and short spike latency.

When dopamine modulation of variables was included into the analysis IB cells showed very consistent DA effects. Indeed, this study has for the first time identified specific modulation of IB cells through DA receptors. Both DA receptor subtypes induce a shift of the input-output function towards lower input intensities. IB cells can further be identified based on the overall shape of basal and apical dendrite, with wider apical dendrites but smaller basal dendrites. These different area shapes might indicate sampling of different cortical information streams, where apical dendrites of IB cells sample inputs from all superficial layers. Bursting cells in the PFC have been shown to integrate input from neighbouring corticocortical cells (Morishima and Kawaguchi, 2006). IB cells are probably identical with previously reported corticopontine and corticothalamic cells (Kasper et al., 1994; Hattox and Nelson, 2007), which have been shown to form specific sub-networks within deep layers of the cortex (Markram et al., 1997; Morishima and Kawaguchi, 2006). With their extended apical dendrite IB cells probably also have enhanced capabilities for local dendritic computation (London and Häusser, 2005). Thus circuit specific action of dopamine in prefrontal networks might enable selective control of information flow towards thalamic and subcortical circuits depending on cognitive demands. The interaction between cell type specific DA modulation and dendritic function is one interesting point for future investigations.

All other recorded cells are grouped into different clusters depending on the chosen dataset. This denies a clear identification of subpopulations in non-bursting cells. Based on the results from electrophysiology non-bursting cells have been separated into regular spiking cells (RS), which fire regular spikes (sometimes an initial spike doublet) with varying degrees of adaptation

in response to current stimulation and intermediate cells (IM), which shows intermediate values for the membrane time constant and input resistance. Non-IB cells also display a higher variability in dendritic structure, with smaller apical dendrites but wider basal dendrites. Also, a possible subtype of non-IB cells with skewed basal dendrites might exist.

When using both physiological and morphological parameter for cluster analysis, new cluster emerge in non-IB cells, that do not overlap with cluster solutions from physiology or morphology data alone. The combination of physiology and morphology variables probably has greater power in finding similarities between cells, since some cluster in the combined feature space show much reduced variance (as measured by standard deviation). Yet, final conclusions on the "true" subpopulations cannot be drawn, due to the limited number of non bursting cells recorded. Non-IB cells probably correlate corticocortical and corticostriatal cells (Morishima and Kawaguchi, 2006; Otsuka and Kawaguchi, 2008). Their heterogeneity might provide a richer spectrum of computational properties, allowing more flexible processing of information streams.

Non-IB cells show weak but consistent D1 receptor modulation of excitability, where D1 activation increases gain for low intensity inputs and pushes cells towards intrinsic bistability. This D1 effect might complement DA effects synaptic mechanisms that stabilise persistent activity states in PFC networks (Durstewitz et al., 2000a; Thurley et al., 2008).

Furthermore, a subpopulation of non-IB cells may exist, which shows strong D2 receptor agonist response. In this subset D2 receptor activation pushes neurons away from bistability. Thus D2 activation could, in this subpopulation, facilitate the reversal of previous persistent firing states, thereby enabling clearance of respective short term memorised information (Durstewitz and Seamans, 2008). This is highly speculative based on the current dataset and more detailed analysis of non-IB type pyramidal cells and their D2 receptor mediated modulation is needed.

Criticism

Several points of critique can be raised. The catalogue of electrophysiological stimuli was selected to characterise neuronal responses on different time scales and for a wide range of input strengths, but the set of chosen stimulation protocols used rather static somatic stimulation through ramps and steps. Other studies have emphasised the need for dynamic input stimuli to reliably describe input-output functions of cortical pyramidal cells (Chance et al., 2002; Fellous et al., 2003; Badel et al., 2008; Thurley et al., 2008; London et al., 2008; La Camera et al., 2008). For example Badel et al. (2008) have used sophisticated stimulation patterns and analysis to analyse input-output functions of neocortical pyramidal cells. They have used measurements

of the membrane capacitance to estimate the time dependent membrane current during ongoing activity. This yields an exact description of the current to membrane voltage relationship (input-output curve) and accurately predicted spike times when plugged into an integrate-and-fire neuron model. This curve was coined 'dynamic input-output function' to highlight the difference to conventional ramp and step stimulations (as used in the current study), that rely on steady state values for membrane current or voltage. These steady state values might indeed include large fractions of inactivated voltage gated sodium and/or potassium channels, due to the stimulation procedure. Thus for a faithful description of input-output functions, that could be used to parameterise biophysical models, more sophisticated techniques are advisable. Since in the current study the focus lied on comparing different cells under similar conditions, this amount of detail may not be crucial for the presented results. Yet, more exact description of input-output function might help to reveal consistent differences in non-bursting deep layer cortical pyramidal cells. Hence, future studies will have to address this through applying more realistic input patterns.

Moreover, input-output functions were only measured through somatic stimulation which is not suited to quantify the influence of dendritic conductances on input-output functions. Future studies would need to use more advanced recording techniques, i.e. simultaneous somatic and dendritic patching (Davie et al., 2006), to elucidate the exact biophysical and dendritic properties of the more diverse non-bursting pyramidal cell populations in the prefrontal cortex of rats.

The current use of DA receptor agonists assumes reversible and transient effects of D1 and D2 receptor activation. Critical for the peer reviewed publication of the current results will be the demonstration of washout of D2 effects and/or repetition of experiments for similar cell types with only D1 or D2 receptor agonist. Also, time and dose dependent effects should be included in future investigations of cell type specific DA effects.

This study has demonstrated that the combined use of dimensionality reduction through PCA and classification through hierarchical cluster analysis is suited to analyse a large number of variables that characterise a small number of cells. This statistical problem of classifying items based on a large feature space is commonly referred to as p>>N (Hastie et al., 2009). The current approach presents computationally simplified method that relies on the combination of two reliable and well documented methods. Indeed the results obtained show that combined PCA/HCA analysis is well suited to identify similarity in datasets with a large feature space. Moreover, the obtained cluster solutions seem robust against omission of single variables, as demonstrated by a leave-one-out type analysis. The influence of single variables in shaping cluster solutions seems balanced by a certain amount redundancy of information in the principal components. The principal components have here been calculated on normalised variables (z-

score) which essentially sort variables according to covariance, thus missing one variable does not affect the cluster solutions strongly, if similar information is carried in other variables.

Probably the largest limitation of the current study is the relatively small database of recorded cells. Final conclusions on possible subpopulations of non-IB cells cannot be drawn at this point. It has to be noted that whole cell patch recording in adult brain slices is considerably harder, compared to recording in young tissue. Furthermore, the manual reconstruction of neuronal cell morphology is very labour intensive. Recently, various groups have published a number of automated reconstruction algorithms, that should ease the reconstruction of neuronal morphology considerably (Cohen et al., 1994; Al-Kofahi et al., 2002; Evers et al., 2005; Rodriguez et al., 2008; Losavio et al., 2008). This should lead to a high throughput morphological analysis of cells based on confocal image stacks, since confocal LSM is readily available in most laboratories.

Outlook

The thorough quantitative measurement of single cell physiology and morphology in the current study provide the foundation for detailed biophysical models of prefrontal pyramidal cell types. To achieve this, series of high resolution image stacks of labelled neurons can be acquired, subsequently semi-automatically traced and reconstructed. These morphologically detailed pyramidal cell models can then be tuned to reproduce physiological responses measured *in vitro*. Eventually this will allow investigation of single cell computational properties in far greater detail. Thus the current database will further contribute to unravelling computational functions of deep layer pyramidal cells in the PFC.

Future work will also investigate how single cell properties observed *in vitro* might influence cortical network behaviour. For example, networks of pyramidal cells models and fast spiking interneurons with random variations in synaptic and intrinsic parameters have been implemented. These randomised networks were then subjected to different dopamine regimes. Preliminary results suggest that D1 dominated network states exhibit of low frequency oscillations and increased synchronisation between individual cells. Therein, ensembles with similar cross correlation patterns arise, favouring self organised weakly phase locked neuronal assemblies (Bartsch and Durstewitz, 2006). Furthermore it will be interesting to investigate combined effects of DA on intrinsic and synaptic plasticity in network simulations (Kyle et al., 2009), in particular with respect to recently proposed synaptic mechanisms of working memory (Mongillo et al., 2008).

To conclude, the current study has shown one approach to multivariate classification of cortical pyramidal cells. The current analysis is by no means complete, but nevertheless provides a

quantitative reference frame for future investigations. In particular the combination of physiology, neuromodulation and morphological characteristics has proven that prefrontal deep layer pyramidal cells do indeed form distinct and overlapping clusters in these different parameter spaces. The issue of identifying distinct subpopulations within cortical pyramidal cells has received increasing attention in the last decade (Elston, 2003c; Molnár and Cheung, 2006; Borst, 2008; Brown and Hestrin, 2009a; Bernard et al., 2009). In particular the prospect of identifying specific genetic markers for pyramidal cell populations (Molnár and Cheung, 2006) raises hopes for more specific tools, such as transgenic labelling in mice, or retroviral infection in rats to further elucidate the complex function of cortical pyramidal cells.

List of References

Abeles M (1991) Corticonics: neural circuits of the cerebral cortex. Cambridge, UK: Cambridge University Press.

Akert K (1964) Comparative anatomy of frontal cortex and thalamofrontal connections In J. Warren & K. Akert, eds. The frontal granular cortex and behavior New York: McGraw-Hill, p. 372-396.

Al-Kofahi K, Lasek S, Szarowski D, Pace C, Nagy G, Turner J, Roysam B (2002) Rapid automated three-dimensional tracing of neurons from confocal image stacks. IEEE Transactions on Information Technology in Biomedicine 6:171-187

Amit D, Brunel N (1995) Learning Internal Representations in An Attractor Neural-Network with Analog Neurons. Network-Computation in Neural Systems 6:359-388

Andrews NO, Fox EA (2007) Recent Developments in Document Clustering. Available at: http://eprints.cs.vt.edu/archive/00001000/ [Accessed January 14, 2010].

Armstrong CM, Bezanilla F, Rojas E (1973) Destruction of Sodium Conductance Inactivation in Squid Axons Perfused with Pronase. Journal of General Physiology 62:375-391

Arnsten AF (1997) Catecholamine regulation of the prefrontal cortex. J. Psychopharmacol. (Oxford) 11:151-162

Arsiero M, Luscher H, Lundstrom BN, Giugliano M (2007) The Impact of Input Fluctuations on the Frequency-Current Relationships of Layer 5 Pyramidal Neurons in the Rat Medial Prefrontal Cortex. Journal of Neuroscience 27:3274-3284

Ascoli GA et al. (2008) Petilla terminology: nomenclature of features of GABAergic interneurons of the cerebral cortex. Nat Rev Neurosci 9:557-568

Badel L, Lefort S, Brette R, Petersen CCH, Gerstner W, Richardson MJE (2008) Dynamic I-V Curves Are Reliable Predictors of Naturalistic Pyramidal-Neuron Voltage Traces. J Neurophysiol 99:656-666

Baeg E, Kim Y, Huh K, Mook-Jung I, Kim H, Jung M (2003) Dynamics of Population Code for Working Memory in the Prefrontal Cortex. Neuron 40:177-188

Barbas H, Ghashghaei H (2002) Anatomic basis of functional specialization in prefrontal cortices in primates In Handbook of Neuropsychology , p. 1–27.

Barbas H, Henion THH, Dermon CR (1991) Diverse thalamic projections to the prefrontal cortex in the rhesus monkey. The Journal of Comparative Neurology 313:65-94

Barbas H (2000) Connections underlying the synthesis of cognition, memory, and

emotion in primate prefrontal cortices. Brain Research Bulletin 52:319-330

Bartsch U, Durstewitz D (2006) Dopamine modulates slow frequency oscillations and coherence in a prefrontal cortex network model In FENS Abstracts., p. A116.

Bastian J, Nguyenkim J (2001) Dendritic modulation of burst-like firing in sensory neurons. J. Neurophysiol 85:10-22

Bates JF, Goldman-Rakic PS (1993) Prefrontal connections of medial motor areas in the rhesus monkey. The Journal of Comparative Neurology 336:211-228

Bean RC, Shepherd WC, Chan H, Eichner J (1969) Discrete Conductance Fluctuations in Lipid Bilayer Protein Membranes. J. Gen. Physiol. 53:741-757

Benavides-Piccione R, Hamzei-Sichani F, Ballesteros-Yanez I, DeFelipe J, Yuste R (2006) Dendritic Size of Pyramidal Neurons Differs among Mouse Cortical Regions. Cereb. Cortex 16:990-1001

Benda J, Longtin A, Maler L (2005) Spike-Frequency Adaptation Separates Transient Communication Signals from Background Oscillations. J. Neurosci. 25:2312-2321

Bernard A, Sorensen SA, Lein ES (2009) Shifting the paradigm: new approaches for characterizing and classifying neurons. Current Opinion in Neurobiology 19:530-536

Bernardi G, Cherubini E, Marciani M, Mercuri N, Stanzione P (1982) Responses of intracellularly recorded cortical neurons to the iontophoretic application of dopamine. Brain Res 245:267-274

Bertschinger N, Natschläger T (2004) Real-time computation at the edge of chaos in recurrent neural networks. Neural Computation 16:1413-1436

Borst A (2008) How does nature program neuron types? Front. Neurosci. 2:4-5

Boutet de Monvel J, Le Calvez S, Ulfendahl M (2001) Image Restoration for Confocal Microscopy: Improving the Limits of Deconvolution, with Application to the Visualization of the Mammalian Hearing Organ. Biophysical Journal 80:2455-2470

Brodmann K (1909) Vergleichende Lokalisationslehre der Grosshirnrinde in ihren Prinzipien dargestellt auf Grund des Zellenbaues. Leipzig: Barth.

Brody C, Hernandez A, Zainos A, Romo R (2003) Timing and neural encoding of somatosensory parametric working memory in macaque prefrontal cortex. Cereb.Cortex 13:1196-1207

Brown SP, Hestrin S (2009a) Cell-type identity: a key to unlocking the function of neocortical circuits. Current Opinion in Neurobiology 19:415-421

Brown SP, Hestrin S (2009b) Intracortical circuits of pyramidal neurons reflect their long-range axonal targets. Nature 457:1133-1136

Brown VJ, Bowman EM (2002) Rodent models of prefrontal cortical function. Trends in Neurosciences 25:340-343

Brunel N, Wang X (2001) Effects of neuromodulation in a cortical network model of object working memory dominated by recurrent inhibition. J Comput.Neurosci. 11:63-85

Burke KA, Franz TM, Miller DN, Schoenbaum G (2008) The role of the orbitofrontal cortex in the pursuit of happiness and more specific rewards. Nature 454:340-344

Cajal SRY (1899) Comparative Study of the Sensory Areas of the Human Cortex.

Calvin WH, Sypert GW (1976) Fast and slow pyramidal tract neurons: an intracellular analysis of their contrasting repetitive firing properties in the cat. J Neurophysiol 39:420-434

Cardinal RN, Parkinson JA, Hall J, Everitt BJ (2002) Emotion and motivation: the role of the amygdala, ventral striatum, and prefrontal cortex. Neuroscience & Biobehavioral Reviews 26:321-352

Carlsson K, Wallén P, Brodin L (1989) Three-dimensional imaging of neurons by confocal fluorescence microscopy. J Microsc 155:15-26

Carr DB, Sesack SR (2000) Projections from the Rat Prefrontal Cortex to the Ventral Tegmental Area: Target Specificity in the Synaptic Associations with Mesoaccumbens and Mesocortical Neurons. J. Neurosci. 20:3864-3873

Carrington W, Fogarty K, Lifshitz L, Tuft R (1999) High resolution 3-D imaging of living cells by image restoration. In Imaging Living Cells Springer-Verlag Telos.

Cauli B, Porter JT, Tsuzuki K, Lambolez B, Rossier J, Quenet B, Audinat E (2000) Classification of fusiform neocortical interneurons based on unsupervised clustering. Proceedings of the National Academy of Sciences of the United States of America 97:6144-6149

Cavada C, Goldman-Rakic PS (1989) Posterior parietal cortex in rhesus monkey: I. Parcellation of areas based on distinctive limbic and sensory corticocortical connections. The Journal of Comparative Neurology 287:393-421

Cepeda C, Levine MS (1998) Dopamine and N-Methyl-D- Aspartate Receptor Interactions in the Neostriatum. Dev Neurosci 20:1-18

Chagnac-Amitai Y, Luhmann HJ, Prince DA (1990) Burst generating and regular spiking layer 5 pyramidal neurons of rat neocortex have different morphological features. The Journal of Comparative Neurology 296:598-613

Chance FS, Abbott L, Reyes AD (2002) Gain Modulation from Background Synaptic Input. Neuron 35:773-782

Chang J, Chen L, Luo F, Shi L, Woodward DJ (2002) Neuronal responses in the frontal cortico-basal ganglia system during delayed matching-to-sample task: ensemble recording in freely moving rats. Exp Brain Res 142:67-80

Chavis DA, Pandya DN (1976) Further observations on corticofrontal connections in the rhesus monkey. Brain Research 117:369-386

Chen C, Abrams S, Pinhas A, Brumberg JC (2009) Morphological heterogeneity of layer VI neurons in mouse barrel cortex. J. Comp. Neurol. 512:726-746

Chen G, Greengard P, Yan Z (2004) Potentiation of NMDA receptor currents by dopamine D1 receptors in prefrontal cortex. Proc Natl Acad Sci U S A 101:2596-2600

Cohen AR, Roysam B, Turner JN (1994) Automated tracing and volume measurements of neurons from 3-D confocal fluorescence microscopy data. J Microsc 173:103-114

Collins TJ (2007) ImageJ for microscopy. Biotechniques 43:25-30

Compte A (2006) Computational and in vitro studies of persistent activity: edging towards cellular and synaptic mechanisms of working memory. Neuroscience 139:135-151

Compte A, Brunel N, Goldman-Rakic P, Wang X (2000) Synaptic mechanisms and network dynamics underlying spatial working memory in a cortical network model. Cereb.Cortex 10:910-923

Compte A, Constantinidis C, Tegner J, Raghavachari S, Chafee M, Goldman-Rakic P, Wang X (2003) Temporally irregular mnemonic persistent activity in prefrontal neurons of monkeys during a delayed response task. J.Neurophysiol. 90:3441-3454

Condé F, Audinat E, Maire-Lepoivre E, Crépel F (1990) Afferent connections of the medial frontal cortex of the rat. A study using retrograde transport of fluorescent dyes. I. Thalamic afferents. Brain Res. Bull 24:341-354

Condé F, Maire-lepoivre E, Audinat E, Crépel F (1995) Afferent connections of the medial frontal cortex of the rat. II. Cortical and subcortical afferents. The Journal of Comparative Neurology 352:567-593

Connors BW, Gutnick MJ, Prince DA (1982) Electrophysiological properties of neocortical neurons in vitro. J. Neurophysiol 48:1302-1320

Connors BW, Gutnick MJ (1990) Intrinsic firing patterns of diverse neocortical neurons. Trends in Neurosciences 13:99-104

Crook SM, Ermentrout GB, Bower JM (1998) Spike frequency adaptation affects the synchronization properties of networks of cortical oscillations. Neural Comput 10:837-854

Cudmore RH, Turrigiano GG (2004) Long-Term Potentiation of Intrinsic Excitability

in LV Visual Cortical Neurons. J Neurophysiol 92:341-348

Cullheim S, Kellerth JO (1978) A morphological study of the axons and recurrent axon collaterals of cat alpha-motoneurones supplying different hind-limb muscles. J Physiol 281:285-299

Damasio A (1994) Descartes' error; emotion, reason, and the human brain. New York: Avon Books.

Damasio AR, Everitt BJ, Bishop D (1996) The Somatic Marker Hypothesis and the Possible Functions of the Prefrontal Cortex [and Discussion]. Philosophical Transactions of the Royal Society of London. Series B: Biological Sciences 351:1413-1420

Damasio H, Grabowski T, Frank R, Galaburda A, Damasio A (1994) The return of Phineas Gage: clues about the brain from the skull of a famous patient. Science 264:1102-1105

Davie JT, Kole MHP, Letzkus JJ, Rancz EA, Spruston N, Stuart GJ, Häusser M (2006) Dendritic patch-clamp recording. Nat. Protocols 1:1235-1247

Degenetais E, Thierry A, Glowinski J, Gioanni Y (2002) Electrophysiological Properties of Pyramidal Neurons in the Rat Prefrontal Cortex: An In Vivo Intracellular Recording Study. Cereb. Cortex 12:1-16

Destexhe A, Rudolph M, Pare D (2003) The high-conductance state of neocortical neurons in vivo. Nat.Rev.Neurosci. 4:739-751

Ding C, He X (2004) K-means clustering via principal component analysis In Proceedings of the twenty-first international conference on Machine learning Banff, Alberta, Canada: ACM, p. 29. Available at: http://portal.acm.org/citation.cfm?id=1015330.1015408 [Accessed January 14, 2010].

Divac I, Kosmal A, Björklund A, Lindvall O (1978) Subcortical projections to the prefrontal cortex in the rat as revealed by the horseradish peroxidase technique. Neuroscience 3:785-796

Dong Y, White F (2003) Dopamine D1-class receptors selectively modulate a slowly inactivating potassium current in rat medial prefrontal cortex pyramidal neurons. J.Neurosci. 23:2686-2695

Dong Y, Cooper D, Nasif F, Hu XT, White FJ (2004) Dopamine Modulates Inwardly Rectifying Potassium Currents in Medial Prefrontal Cortex Pyramidal Neurons. J.Neurosci. 24:3077-3085

Douglas RJ, Martin KAC (2004) Neuronal circuits of the neocortex. Annu. Rev. Neurosci 27:419-451

Dragoi G, Buzsaki G (2006) Temporal encoding of place sequences by hippocampal cell assemblies. Neuron 50:145-157

Dreher J, Guigon E, Burnod Y (2002) A Model of Prefrontal Cortex Dopaminergic Modulation during the Delayed Alternation Task. Journal of Cognitive Neuroscience 14:853-865

Dumitriu D, Cossart R, Huang J, Yuste R (2007) Correlation Between Axonal Morphologies and Synaptic Input Kinetics of Interneurons from Mouse Visual Cortex. Cereb. Cortex 17:81-91

Duncan J (2001) An adaptive coding model of neural function in prefrontal cortex. Nat Rev Neurosci 2:820-829

Durstewitz D (2003) Self-organizing neural integrator predicts interval times through climbing activity. J.Neurosci. 23:5342-5353

Durstewitz D, Seamans J (2002) The computational role of dopamine D1 receptors in working memory. Neural Networks 15:561-572

Durstewitz D, Seamans J (2006) Beyond bistability: Biophysics and temporal dynamics of working memory. Neuroscience 139:119-133

Durstewitz D, Seamans J, Sejnowski T (2000a) Dopamine-mediated stabilization of delay-period activity in a network model of prefrontal cortex. J Neurophysiol 83:1733-1750

Durstewitz D, Seamans J, Sejnowski T (2000b) Neurocomputational models of working memory. Nat Neurosci 3 Suppl:1184-91.:1184-1191

Durstewitz D, Gabriel T (2007) Dynamical basis of irregular spiking in NMDA-driven prefrontal cortex neurons. Cereb Cortex 17:894-908

Durstewitz D, Seamans JK (2002) The computational role of dopamine D1 receptors in working memory. Neural Networks 15:561-572

Durstewitz D, Seamans JK (2008) The Dual-State Theory of Prefrontal Cortex Dopamine Function with Relevance to Catechol-O-Methyltransferase Genotypes and Schizophrenia. Biological Psychiatry 64:739-749

Egger MD, Petran M (1967) New Reflected-Light Microscope for Viewing Unstained Brain and Ganglion Cells. Science 157:305-307

Elston GN (2003a) Cortex, cognition and the cell: new insights into the pyramidal neuron and prefrontal function. Cereb. Cortex 13:1124-1138

Elston GN (2003b) Cortex, Cognition and the Cell: New Insights into the Pyramidal Neuron and Prefrontal Function. Cereb. Cortex 13:1124-1138

Elston GN (2003c) Cortex, Cognition and the Cell: New Insights into the Pyramidal Neuron and Prefrontal Function. Cereb. Cortex 13:1124-1138

Evers JF, Schmitt S, Sibila M, Duch C (2005) Progress in Functional Neuroanatomy: Precise Automatic Geometric Reconstruction of Neuronal Morphology From Confocal Image Stacks. J Neurophysiol 93:2331-2342

Fellous J-, Rudolph M, Destexhe A, Sejnowski TJ (2003) Synaptic background noise controls the input/output characteristics of single cells in an in vitro model of in vivo activity. Neuroscience 122:811-829

Floresco S, Phillips A (2001) Delay-dependent modulation of memory retrieval by infusion of a dopamine D1 agonist into the rat medial prefrontal cortex. Behav.Neurosci. 115:934-939

Fuhrmann G, Markram H, Tsodyks M (2002) Spike Frequency Adaptation and Neocortical Rhythms. J Neurophysiol 88:761-770

Funahashi S, Bruce C, Goldman-Rakic P (1989) Mnemonic coding of visual space in the monkey's dorsolateral prefrontal cortex. J Neurophysiol 61:331-349

Fuster JM (1973) Unit activity in prefrontal cortex during delayed-response performance: neuronal correlates of transient memory. J. Neurophysiol 36:61-78

Fuster J (2001) The prefrontal cortex - An update: time is of the essence. Neuron 30:319-333

Fuster J (2008) The Prefrontal Cortex, Fourth Edition 4th ed. Academic Press.

Gao W, Krimer L, Goldman-Rakic P (2001) Presynaptic regulation of recurrent excitation by D1 receptors in prefrontal circuits. Proc.Natl.Acad Sci U.S.A 98:295-300

Gao W, Goldman-Rakic PS (2003) Selective modulation of excitatory and inhibitory microcircuits by dopamine. Proceedings of the National Academy of Sciences of the United States of America 100:2836-2841

Gao W, Zheng Z (2004) Target-specific differences in somatodendritic morphology of layer V pyramidal neurons in rat motor cortex. The Journal of Comparative Neurology 476:174-185

Gao W, Goldman-Rakic P (2003) Selective modulation of excitatory and inhibitory microcircuits by dopamine. Proceedings of the National Academy of Sciences of the United States of America 100:2836

Gao W, Wang Y, Goldman-Rakic P (2003) Dopamine modulation of perisomatic and peridendritic inhibition in prefrontal cortex. Journal of Neuroscience 23:1622

Garrido-Sanabria E, Perez M, Banuelos C, Reyna T, Hernandez S, Castaneda M, Colom L (2007) Electrophysiological and morphological heterogeneity of slow firing neurons in medial septal/diagonal band complex as revealed by cluster analysis. Neuroscience 146:931-945

Gaspar P, Bloch B, Le Moine C (1995) D1 and D2 receptor gene expression in the rat

frontal cortex: cellular localization in different classes of efferent neurons. Eur. J. Neurosci 7:1050-1063

Gaykema RPA, Weeghel RV, Hersh LB, Luiten PGM (1991) Prefrontal cortical projections to the cholinergic neurons in the basal forebrain. The Journal of Comparative Neurology 303:563-583

Ghashghaei HT, Barbas H (2001) Neural interaction between the basal forebrain and functionally distinct prefrontal cortices in the rhesus monkey. Neuroscience 103:593-614

Gilbert C, Wiesel T (1989) Columnar specificity of intrinsic horizontal and corticocortical connections in cat visual cortex. J. Neurosci. 9:2432-2442

Goldman-Rakic PS (1988) Topography of Cognition: Parallel Distributed Networks in Primate Association Cortex. Annu. Rev. Neurosci. 11:137-156

Goldman-Rakic PS, Leranth C, Williams SM, Mons N, Geffard M (1989) Dopamine synaptic complex with pyramidal neurons in primate cerebral cortex. Proceedings of the National Academy of Sciences of the United States of America 86:9015-9019

Goldman-Rakic P (1995) Cellular basis of working memory. Neuron 14:477-485

Goldman-Rakic P, Muly E, Williams G (2000) D(1) receptors in prefrontal cells and circuits. Brain Res.Brain Res.Rev. 31:295-301

Goldman-Rakic PS, Porrino LJ (1985) The primate mediodorsal (MD) nucleus and its projection to the frontal lobe. The Journal of Comparative Neurology 242:535-560

Gorelova N, Seamans J, Yang C (2002) Mechanisms of dopamine activation of fast-spiking interneurons that exert inhibition in rat prefrontal cortex. J.Neurophysiol. 88:3150-3166

Gorelova NA, Yang CR (2000) Dopamine D1/D5 Receptor Activation Modulates a Persistent Sodium Current in Rat Prefrontal Cortical Neurons In Vitro. J Neurophysiol 84:75-87

Granon S, Passetti F, Thomas KL, Dalley JW, Everitt BJ, Robbins TW (2000) Enhanced and impaired attentional performance after infusion of D1 dopaminergic receptor agents into rat prefrontal cortex. J. Neurosci 20:1208-1215

Groenewegen HJ, Berendse HW (1994) The specificity of the 'nonspecific' midline and intralaminar thalamic nuclei. Trends in Neurosciences 17:52-57

Groenewegen H, Witter M (2004) Thalamus In G. Paxinos, ed. The Rat Nervous System San Diego: Elsevier Academic Press, p. 407-453.

Groh A, Meyer HS, Schmidt EF, Heintz N, Sakmann B, Krieger P (2009) Cell-Type Specific Properties of Pyramidal Neurons in Neocortex Underlying a Layout that Is Modifiable Depending on the Cortical Area. Cereb. Cortex:bhp152

Gulledge AT, Jaffe DB (1998) Dopamine Decreases the Excitability of Layer V Pyramidal Cells in the Rat Prefrontal Cortex. J. Neurosci. 18:9139-9151

Gulledge A, Jaffe D (2001) Multiple effects of dopamine on layer V pyramidal cell excitability in rat prefrontal cortex. Journal of Neurophysiology 86:586

Halbhuber K, König K (2003) Modern laser scanning microscopy in biology, biotechnology and medicine. Annals of Anatomy - Anatomischer Anzeiger 185:1-20

Hallman LE, Schofield BR, Lin C (1988) Dendritic morphology and axon collaterals of corticotectal, corticopontine, and callosal neurons in layer V of primary visual cortex of the hooded rat. The Journal of Comparative Neurology 272:149-160

Hamill O, Marty A, Neher E, Sakmann B, Sigworth F (1981) Improved patch-clamp techniques for high-resolution current recording from cells and cell-free membrane patches. Pflügers Archiv, European Journal of Physiology 391:85-100

Harlow JM (1999) Passage of an Iron Rod Through the Head. J Neuropsychiatry Clin Neurosci 11:281-283

Hastie T, Tibshirani R, Friedman J (2009) The Elements of Statistical Learning: Data Mining, Inference, and Prediction, Second Edition 2nd ed. Springer.

Hattox AM, Nelson SB (2007) Layer V Neurons in Mouse Cortex Projecting to Different Targets Have Distinct Physiological Properties. J Neurophysiol 98:3330-3340

Häusser M, Spruston N, Stuart GJ (2000) Diversity and Dynamics of Dendritic Signaling. Science 290:739-744

Hefti BJ, Smith PH (2000) Anatomy, Physiology, and Synaptic Responses of Rat Layer V Auditory Cortical Cells and Effects of Intracellular GABAA Blockade. J Neurophysiol 83:2626-2638

Helmstaedter M, Sakmann B, Feldmeyer D (2009a) L2/3 Interneuron Groups Defined by Multiparameter Analysis of Axonal Projection, Dendritic Geometry, and Electrical Excitability. Cereb. Cortex 19:951-962

Helmstaedter M, Sakmann B, Feldmeyer D (2009b) The Relation between Dendritic Geometry, Electrical Excitability, and Axonal Projections of L2/3 Interneurons in Rat Barrel Cortex. Cereb. Cortex 19:938-950

Helmstaedter M, Sakmann B, Feldmeyer D (2009c) Neuronal Correlates of Local, Lateral, and Translaminar Inhibition with Reference to Cortical Columns. Cereb. Cortex 19:926-937

Herrling PL, Hull CD (1980) Iontophoretically applied dopamine depolarizes and hyperpolarizes the membrane of cat caudate neurons. Brain Res 192:441-462

Hibbs AR (2004) Confocal Microscopy for Biologists 1st ed. Springer.

Higgs MH, Slee SJ, Spain WJ (2006) Diversity of Gain Modulation by Noise in Neocortical Neurons: Regulation by the Slow Afterhyperpolarization Conductance. J. Neurosci. 26:8787-8799

Hille B (1976) Gating in Sodium Channels of Nerve. Annual Review of Physiology 38:139-152

Hopfield J (1995) Pattern recognition computation using action potential timing for stimulus representation. Nature 376:33-36

Hounsgaard J, Hultborn H, Jespersen B, Kiehn O (1988) Bistability of alpha-motoneurones in the decerebrate cat and in the acute spinal cat after intravenous 5-hydroxytryptophan. The Journal of Physiology 405:345 -367

Hsu KS (1996) Characterization of dopamine receptors mediating inhibition of excitatory synaptic transmission in the rat hippocampal slice. J Neurophysiol 76:1887-1895

http://microcircuit.epfl.ch/ (2010) Neocortical Microcircuit Database. Available at: http://microcircuit.epfl.ch/ [Accessed January 26, 2010].

Ikegaya Y, Aaron G, Cossart R, Aronov D, Lampl I, Ferster D, Yuste R (2004) Synfire chains and cortical songs: temporal modules of cortical activity. Science 304:559-564

Isseroff A, Schwartz M, Dekker J, Goldman-Rakic P (1984) Columnar organization of callosal and associational projections from rat frontal cortex. Brain Research 293:213-223

Izhikevich EM (2007) Dynamical systems in neuroscience. MIT Press.

Jain AK, Murty MN, Flynn PJ (1999) Data clustering: a review. ACM Comput. Surv. 31:264-323

Jain AK, Dubes RC (1988) Algorithms for clustering data. Englewood Cliffs, NJ: Prentice-Hall, Inc. Available at: http://portal.acm.org/citation.cfm?id=42779&dl= [Accessed January 13, 2010].

Janowitz MK, van Rossum MCW (2006) Excitability changes that complement Hebbian learning. Network 17:31-41

Jelinek HF, Fernandez E (1998) Neurons and fractals: how reliable and useful are calculations of fractal dimensions? Journal of Neuroscience Methods 81:9-18

Jodoj E, Chiang C, Aston-Jones G (1998) Potent excitatory influence of prefrontal cortex activity on noradrenergic locus coeruleus neurons. Neuroscience 83:63-79

Jolliffe I (2004) Principal component analysis 2nd ed. New York: Springer.

Jones EG, Powell TP (1970) An anatomical study of converging sensory pathways

within the cerebral cortex of the monkey. Brain 93:793-820

Jones M, Wilson M (2005) Theta rhythms coordinate hippocampal-prefrontal interactions in a spatial memory task. PLoS.Biol. 3:e402

Jung M, Qin Y, McNaughton B, Barnes C (1998) Firing characteristics of deep layer neurons in prefrontal cortex in rats performing spatial working memory tasks. Cereb. Cortex 8:437-450

Kasper EM, Larkman AU, Lübke J, Blakemore C (1994) Pyramidal neurons in layer 5 of the rat visual cortex. I. Correlation among cell morphology, intrinsic electrophysiological properties, and axon targets. The Journal of Comparative Neurology 339:459-474

Kawaguchi Y (1993) Groupings of nonpyramidal and pyramidal cells with specific physiological and morphological characteristics in rat frontal cortex. J Neurophysiol 69:416-431

Kievit J, Kuypers HG (1975) Subcortical afferents to the frontal lobe in the rhesus monkey studied by means of retrograde horseradish peroxidase transport. Brain Res 85:261-266

King MA, Louis PM, Hunter BE, Walker DW (1989) Biocytin: a versatile anterograde neuroanatomical tract-tracing alternative. Brain Res 497:361-367

Koch C, Rapp M, Segev I (1996) A Brief History of Time (Constants). Cereb. Cortex 6:93-101

Kolb B (1984) Functions of the frontal cortex of the rat: A comparative review. Brain Research Reviews 8:65-98

Kolb B, Nonneman AJ, Singh R (1974) Double dissociation of spatial impairments and perseveration following selective prefrontal lesions in rats. Journal of Comparative and Physiological Psychology 87:772-780

Komura Y, Tamura R, Uwano T, Nishijo H, Kaga K, Ono T (2001) Retrospective and prospective coding for predicted reward in the sensory thalamus. Nature 412:546-549

Kozloski J, Hamzei-Sichani F, Yuste R (2001) Stereotyped Position of Local Synaptic Targets in Neocortex. Science 293:868-872

Krettek JE, Price JL (1974) A direct input from the amygdala to the thalamus and the cerebral cortex. Brain Res 67:169-174

Krimer LS, Zaitsev AV, Czanner G, Kröner S, González-Burgos G, Povysheva NV, Iyengar S, Barrionuevo G, Lewis DA (2005) Cluster analysis-based physiological classification and morphological properties of inhibitory neurons in layers 2-3 of monkey dorsolateral prefrontal cortex. J. Neurophysiol 94:3009-3022

Kritzer MF, Goldman-Rakic PS (1995) Intrinsic circuit organization of the major

layers and sublayers of the dorsolateral prefrontal cortex in the rhesus monkey. The Journal of Comparative Neurology 359:131-143

Kriventseva EV, Biswas M, Apweiler R (2001) Clustering and analysis of protein families. Current Opinion in Structural Biology 11:334-339

Kroner S, Krimer L, Lewis D, Barrionuevo G (2007) Dopamine increases inhibition in the monkey dorsolateral prefrontal cortex through cell type-specific modulation of interneurons. Cerebral Cortex 17:1020

Kyle R, Bartsch U, Willshaw D, Durstewitz D (2009) Dopamine D1/D2 modulation of synaptic plasticity in the prefrontal cortex In BMC Neuroscience Berlin: Biomed Central, p. P193. Available at: http://www.biomedcentral.com/bmcneurosci/10?issue=S1.

La Camera G, Giugliano M, Senn W, Fusi S (2008) The response of cortical neurons to in vivo-like input current: theory and experiment. Biological Cybernetics 99:279-301

Lapish CC, Kroener S, Durstewitz D, Lavin A, Seamans JK (2007) The ability of the mesocortical dopamine system to operate in distinct temporal modes. Psychopharmacology (Berl.) 191:609-625

Larkman A, Mason A (1990) Correlations between morphology and electrophysiology of pyramidal neurons in slices of rat visual cortex. I. Establishment of cell classes. J. Neurosci. 10:1407-1414

Larkum ME, Zhu JJ, Sakmann B (1999) A new cellular mechanism for coupling inputs arriving at different cortical layers. Nature 398:338-341

Larkum ME, Zhu JJ, Sakmann B (2001) Dendritic mechanisms underlying the coupling of the dendritic with the axonal action potential initiation zone of adult rat layer 5 pyramidal neurons. The Journal of Physiology 533:447-466

Larkum ME, Senn W, Luscher H (2004) Top-down Dendritic Input Increases the Gain of Layer 5 Pyramidal Neurons. Cereb. Cortex 14:1059-1070

Larkum ME, Zhu JJ, Sakmann B (1999) A new cellular mechanism for coupling inputs arriving at different cortical layers. Nature 398:338-341

Lee H, Simpson G, Logothetis N, Rainer G (2005) Phase locking of single neuron activity to theta oscillations during working memory in monkey extrastriate visual cortex. Neuron 45:147-156

Lemon N, Turner RW (2000) Conditional spike backpropagation generates burst discharge in a sensory neuron. J. Neurophysiol 84:1519-1530

Leon M, Shadlen M (2003) Representation of time by neurons in the posterior parietal cortex of the macaque. Neuron 38:317-327

Levitt JB, Lewis DA, Yoshioka T, Lund JS (1993) Topography of pyramidal neuron

intrinsic connections in macaque monkey prefrontal cortex (areas 9 and 46). The Journal of Comparative Neurology 338:360-376

Lewis DA, Melchitzky DS, Burgos G (2002) Specificity in the functional architecture of primate prefrontal cortex. J. Neurocytol 31:265-276

Llinas R (1988) The intrinsic electrophysiological properties of mammalian neurons: insights into central nervous system function. Science 242:1654-1664

London M, Häusser M (2005) Dendritic Computation. Annu. Rev. Neurosci. 28:503-532

London M, Larkum ME, Häusser M (2008) Predicting the synaptic information efficacy in cortical layer 5 pyramidal neurons using a minimal integrate-and-fire model. Biol Cybern 99:393-401

Losavio BE, Liang Y, Santamaria-Pang A, Kakadiaris IA, Colbert CM, Saggau P (2008) Live Neuron Morphology Automatically Reconstructed From Multiphoton and Confocal Imaging Data. J Neurophysiol 100:2422-2429

Lu M, Preston JB, Strick PL (1994) Interconnections between the prefrontal cortex and the premotor areas in the frontal lobe. The Journal of Comparative Neurology 341:375-392

Lynch G, Schubert P (1980) The Use of in Vitro Brain Slices for Multidisciplinary Studies of Synaptic Function. Annu. Rev. Neurosci. 3:1-22

Machens CK, Romo R, Brody CD (2005) Flexible Control of Mutual Inhibition: A Neural Model of Two-Interval Discrimination. Science 307:1121-1124

Mainen Z, Sejnowski T (1995) Reliability of spike timing in neocortical neurons. Science 268:1503-1506

Mainen ZF, Kepecs A (2009) Neural representation of behavioral outcomes in the orbitofrontal cortex. Current Opinion in Neurobiology 19:84-91

Mainen ZF, Sejnowski TJ (1996) Influence of dendritic structure on firing pattern in model neocortical neurons. Nature 382:363-366

Major G, Tank D (2004) Persistent neural activity: prevalence and mechanisms. Curr.Opin.Neurobiol. 14:675-684

von der Malsburg C (1981) The Correlation Theory of Brain Function. Technical Report - MPI for Biophysical Chemistry 81 Available at: http://cogprints.org/1380/01/vdM_correlation.pdf.

Markram H, Lübke J, Frotscher M, Roth A, Sakmann B (1997) Physiology and anatomy of synaptic connections between thick tufted pyramidal neurones in the developing rat neocortex. J. Physiol. (Lond.) 500 (Pt 2):409-440

Markram H, Toledo-Rodriguez M, Wang Y, Gupta A, Silberberg G, Wu C (2004) Interneurons of the neocortical inhibitory system. Nat. Rev. Neurosci 5:793-807

Marty A, Neher E (1995) Tight-Seal Whole-Cell Recording In Single-Channel Recording , p. 31-52. Available at: http://dx.doi.org/10.1007/978-1-4419-1229-9_2 [Accessed January 11, 2010].

Mason A, Larkman A (1990) Correlations between morphology and electrophysiology of pyramidal neurons in slices of rat visual cortex. II. Electrophysiology. J. Neurosci. 10:1415-1428

Maurice N, Tkatch T, Meisler M, Sprunger LK, Surmeier DJ (2001) D1/D5 Dopamine Receptor Activation Differentially Modulates Rapidly Inactivating and Persistent Sodium Currents in Prefrontal Cortex Pyramidal Neurons. J. Neurosci. 21:2268-2277

McCormick DA, Connors BW, Lighthall JW, Prince DA (1985) Comparative electrophysiology of pyramidal and sparsely spiny stellate neurons of the neocortex. J Neurophysiol 54:782-806

Mel BW (1994) Information Processing in Dendritic Trees. Neural Computation 6:1031-1085

Middleton FA, Strick PL (2000) Basal ganglia and cerebellar loops: motor and cognitive circuits. Brain Research Reviews 31:236-250

Miller DJ, Wang Y, Kesidis G (2008) Emergent unsupervised clustering paradigms with potential application to bioinformatics. Front. Biosci 13:677-690

Miller E, Cohen J (2001) An integrative theory of prefrontal cortex function. Annu Rev Neurosci 24:167-202

Miller E, Freedman D, Wallis J (2002) The prefrontal cortex: categories, concepts and cognition. Philos Trans R Soc Lond B Biol Sci 357:1123-1136

Molnár Z, Cheung AF (2006) Towards the classification of subpopulations of layer V pyramidal projection neurons. Neuroscience Research 55:105-115

Molyneaux BJ, Arlotta P, Menezes JRL, Macklis JD (2007) Neuronal subtype specification in the cerebral cortex. Nat Rev Neurosci 8:427-437

Mongillo G, Barak O, Tsodyks M (2008) Synaptic Theory of Working Memory. Science 319:1543-1546

Morishima M, Kawaguchi Y (2006) Recurrent Connection Patterns of Corticostriatal Pyramidal Cells in Frontal Cortex. J. Neurosci. 26:4394-4405

Moyer JR, Brown TH (1998) Methods for whole-cell recording from visually preselected neurons of perirhinal cortex in brain slices from young and aging rats. Journal of Neuroscience Methods 86:35-54

Neher E, Sakmann B (1976) Single-channel currents recorded from membrane of denervated frog muscle fibres. Nature 260:799-802

Neve K, Seamans J, Trantham-Davidson H (2004) Dopamine receptor signaling. J.Recept.Signal.Transduct.Res. 24:165-205

Neve KA, Neve RL (1997) The dopamine receptors. Humana Press.

Niki H (1974a) Prefrontal unit activity during delayed alternation in the monkey. I. Relation to direction of response. Brain Res. 68:185-196

Niki H (1974b) Differential activity of prefrontal units during right and left delayed response trials. Brain Res. 70:346-349

Nowak LG, Azouz R, Sanchez-Vives MV, Gray CM, McCormick DA (2003) Electrophysiological Classes of Cat Primary Visual Cortical Neurons In Vivo as Revealed by Quantitative Analyses. J Neurophysiol 89:1541-1566

Ongur D, Price J (2000) The Organization of Networks within the Orbital and Medial Prefrontal Cortex of Rats, Monkeys and Humans. Cereb. Cortex 10:206-219

Otmakhova NA, Lisman JE (1999) Dopamine Selectively Inhibits the Direct Cortical Pathway to the CA1 Hippocampal Region. J. Neurosci. 19:1437-1445

Otsuka T, Kawaguchi Y (2008) Firing-Pattern-Dependent Specificity of Cortical Excitatory Feed-Forward Subnetworks. J. Neurosci. 28:11186-11195

Otte S, Hasenstaub A, Callaway EM (2010) Cell Type-Specific Control of Neuronal Responsiveness by Gamma-Band Oscillatory Inhibition. J. Neurosci. 30:2150-2159

Otto T, Eichenbaum H (1992) Complementary Roles of the Orbital Prefrontal Cortex and the Perirhinal-Entorhinal Cortices in an Odor-Guided Delayed-Nonmatching-to-Sample Task. Behavioral Neuroscience 106:762-775

Paxinos G, Watson C (2007) The rat brain in stereotaxic coordinates. Academic Press.

de la Pena E, Geijo-Barrientos E (1996) Laminar Localization, Morphology, and Physiological Properties of Pyramidal Neurons that Have the Low-Threshold Calcium Current in the Guinea-Pig Medial Frontal Cortex. J. Neurosci. 16:5301-5311

Penit-Soria J, Audinat E, Crepel F (1987) Excitation of rat prefrontal cortical neurons by dopamine: an in vitro electrophysiological study. Brain Research 425:263-274

Pesaran B, Pezaris J, Sahani M, Mitra P, Andersen R (2002) Temporal structure in neuronal activity during working memory in macaque parietal cortex. Nat Neurosci 5:805-811

Petrides M, Pandya D (2002a) Association pathways of the prefrontal cortex and functional observations In D. T. Stuss & R. T. Knight, eds. Principles of frontal lobe function New York: Oxford University Press, p. 31-50.

Petrides M, Pandya DN (2002b) Comparative cytoarchitectonic analysis of the human and the macaque ventrolateral prefrontal cortex and corticocortical connection patterns in the monkey. European Journal of Neuroscience 16:291-310

Prescott SA, Sejnowski TJ (2008) Spike-Rate Coding and Spike-Time Coding Are Affected Oppositely by Different Adaptation Mechanisms. J. Neurosci. 28:13649-13661

Preuss TM (1995) Do Rats Have Prefrontal Cortex? The Rose-Woolsey-Akert Program Reconsidered. Journal of Cognitive Neuroscience 7:1-24

Pucak ML, Levitt JB, Lund JS, Lewis DA (1996) Patterns of intrinsic and associational circuitry in monkey prefrontal cortex. J. Comp. Neurol 376:614-630

Quintana J, Fuster JM (1999) From Perception to Action: Temporal Integrative Functions of Prefrontal and Parietal Neurons. Cereb. Cortex 9:213-221

Raghavachari S, Lisman J, Tully M, Madsen J, Bromfield E, Kahana M (2005) Theta oscillations in human cortex during a working memory task: Evidence for local generators. J.Neurophysiol. Available at: http://view.ncbi.nlm.nih.gov/pubmed/16207788.

Rall W (1959) Branching dendritic trees and motoneuron membrane resistivity. Experimental Neurology 1:491-527

Rall W, Segev I, Rinzel J, Shepherd GM (1995) The theoretical foundation of dendritic function: selected papers of Wilfrid Rall with commentaries. MIT Press.

Ratiu P, Talos I (2004) The Tale of Phineas Gage, Digitally Remastered. N Engl J Med 351:e21

Ray JP, Price JL (1992) The organization of the thalamocortical connections of the mediodorsal thalamic nucleus in the rat, related to the ventral forebrain-prefrontal cortex topography. The Journal of Comparative Neurology 323:167-197

Ray JP, Price JL (1993) The organization of projections from the mediodorsal nucleus of the thalamus to orbital and medial prefrontal cortex in macaque monkeys. The Journal of Comparative Neurology 337:1-31

Reep RL, Corwin JV (1999) Topographic organization of the striatal and thalamic connections of rat medial agranular cortex. Brain Research 841:43-52

Reutimann J, Yakovlev V, Fusi S, Senn W (2004) Climbing neuronal activity as an event-based cortical representation of time. J Neurosci. 24:3295-3303

Reyes A, Sakmann B (1999) Developmental switch in the short-term modification of unitary EPSPs evoked in layer 2/3 and layer 5 pyramidal neurons of rat neocortex. J. Neurosci 19:3827-3835

Reyes A (2001) INFLUENCE OF DENDRITIC CONDUCTANCES ON THE

INPUT-OUTPUT PROPERTIES OF NEURONS. Annu. Rev. Neurosci. 24:653-675

Rhodes PA, Gray CM (1994) Simulations of Intrinsically Bursting Neocortical Pyramidal Neurons. Neural Computation 6:1086-1110

Riehle A, Grun S, Diesmann M, Aertsen A (1997) Spike synchronization and rate modulation differentially involved in motor cortical function. Science 278:1950-1953

Rodriguez A, Ehlenberger D, Kelliher K, Einstein M, Henderson SC, Morrison JH, Hof PR, Wearne SL (2003) Automated reconstruction of three-dimensional neuronal morphology from laser scanning microscopy images. Methods 30:94-105

Rodriguez A, Ehlenberger DB, Dickstein DL, Hof PR, Wearne SL (2008) Automated Three-Dimensional Detection and Shape Classification of Dendritic Spines from Fluorescence Microscopy Images. PLoS ONE 3

Rohlf FJ, Fisher DR (1968) Tests for Hierarchical Structure in Random Data Sets. Systematic Zoology 17:407-412

Rolls ET (2000) The Orbitofrontal Cortex and Reward. Cereb. Cortex 10:284-294

Rolls ET (2005) Emotion explained. Oxford University Press.

Rose JE, Woolsey CN (1948) The orbitofrontal cortex and its connections with the mediodorsal nucleus in rabbit, sheep and cat. Res Publ Assoc Res Nerv Ment Dis 27 (1 vol.):210-232

Rosenkranz JA, Johnston D (2006) Dopaminergic Regulation of Neuronal Excitability through Modulation of Ih in Layer V Entorhinal Cortex. J. Neurosci. 26:3229-3244

Sakmann B, Stuart G (1995) Patch-Pipette Recordings from the Soma, Dendrites, and Axon of Neurons in Brain Slices In Single-Channel Recording , p. 199-211. Available at: http://dx.doi.org/10.1007/978-1-4419-1229-9_8 [Accessed January 11, 2010].

Sanchez-Vives MV, Nowak LG, McCormick DA (2000) Membrane Mechanisms Underlying Contrast Adaptation in Cat Area 17 In Vivo. J. Neurosci. 20:4267-4285

Santana N, Mengod G, Artigas F (2009) Quantitative Analysis of the Expression of Dopamine D1 and D2 Receptors in Pyramidal and GABAergic Neurons of the Rat Prefrontal Cortex. Cereb. Cortex 19:849-860

Sawaguchi T, Goldman-Rakic PS (1991) D1 dopamine receptors in prefrontal cortex: involvement in working memory. Science 251:947-950

Sawaguchi T, Matsumura M, Kubota K (1990a) Catecholaminergic effects on neuronal activity related to a delayed response task in monkey prefrontal cortex. J. Neurophysiol 63:1385-1400

Sawaguchi T, Matsumura M, Kubota K (1990b) Effects of dopamine antagonists on neuronal activity related to a delayed response task in monkey prefrontal cortex. J.

Neurophysiol 63:1401-1412

Seamans J, Durstewitz D, Christie B, Stevens C, Sejnowski T (2001a) Dopamine D1/D5 receptor modulation of excitatory synaptic inputs to layer V prefrontal cortex neurons. Proc Nat Acad Sci USA 98:301-306

Seamans J, Gorelova N, Durstewitz D, Yang C (2001b) Bidirectional dopamine modulation of GABAergic inhibition in prefrontal cortical pyramidal neurons. J Neurosci. 21:3628-3638

Seamans J, Nogueira L, Lavin A (2003) Synaptic basis of persistent activity in prefrontal cortex in vivo and in organotypic cultures. Cereb.Cortex 13:1242-1250

Seamans J, Lapish C, Durstewitz D (2008) Comparing the prefrontal cortex of rats and primates: Insights from electrophysiology. Neurotoxicity Research 14:249-262

Seamans JK, Yang CR (2004) The principal features and mechanisms of dopamine modulation in the prefrontal cortex. Progress in Neurobiology 74:1-58

Séguéla P, Watkins KC, Descarries L (1988) Ultrastructural features of dopamine axon terminals in the anteromedial and the suprarhinal cortex of adult rat. Brain Res 442:11-22

Sesack SR, Snyder CL, Lewis DA (1995) Axon terminals immunolabeled for dopamine or tyrosine hydroxylase synapse on GABA-immunoreactive dendrites in rat and monkey cortex. The Journal of Comparative Neurology 363:264-280

Shadlen M, Newsome W (1994) Noise, neural codes and cortical organization. Curr.Opin.Neurobiol. 4:569-579

Shadlen M, Newsome W (1998) The variable discharge of cortical neurons: implications for connectivity, computation, and information coding. J.Neurosci. 18:3870-3896

Sholl DA (1953) Dendritic organization in the neurons of the visual and motor cortices of the cat. J Anat. 87:387–4061

Shu Y, Hasenstaub A, McCormick D (2003) Turning on and off recurrent balanced cortical activity. Nature 423:288-293

Siapas A, Lubenov E, Wilson M (2005) Prefrontal phase locking to hippocampal theta oscillations. Neuron 46:141-151

Silver RA (2010) Neuronal arithmetic. Nat Rev Neurosci 11:474-489

Smith OA, DeVito JL (1984) Central Neural Integration for the Control of Autonomic Responses Associated with Emotion. Annu. Rev. Neurosci. 7:43-65

Smith TG, Lange GD, Marks WB (1996) Fractal methods and results in cellular morphology - dimensions, lacunarity and multifractals. Journal of Neuroscience

Methods 69:123-136

Snow P, Rose P, Brown A (1976) Tracing axons and axon collaterals of spinal neurons using intracellular injection of horseradish peroxidase. Science 191:312-313

Softky W, Koch C (1993) The highly irregular firing of cortical cells is inconsistent with temporal integration of random EPSPs. J Neurosci. 13:334-350

Song S, Sjöström PJ, Reigl M, Nelson S, Chklovskii DB (2005) Highly Nonrandom Features of Synaptic Connectivity in Local Cortical Circuits. PLoS Biol 3:e68

Spruston N, Jaffe DB, Williams SH, Johnston D (1993) Voltage- and space-clamp errors associated with the measurement of electrotonically remote synaptic events. J Neurophysiol 70:781-802

Steriade M (2004) Neocortical cell classes are flexible entities. Nat Rev Neurosci 5:121-134

Strogatz S (2001) Nonlinear Dynamics and Chaos. Boulder, CO: Westview Press.

Stuart G, Spruston N, Häusser M (2000) Dendrites 1st ed. Oxford University Press, USA.

Thierry A, Pirot S, Gioanni Y, Glowinski J (1998) Dopamine function in the prefrontal cortex. Advances in pharmacology (San Diego, Calif.) 42:717

Thomson AM, Bannister AP (1998) Postsynaptic pyramidal target selection by descending layer III pyramidal axons: dual intracellular recordings and biocytin filling in slices of rat neocortex. Neuroscience 84:669-683

Thomson AM (2007) Functional maps of neocortical local circuitry. Front Neurosci. 1:19-42

Thurley K, Senn W, Lüscher H (2008) Dopamine Increases the Gain of the Input-Output Response of Rat Prefrontal Pyramidal Neurons. Journal of Neurophysiology 99:2985-2997

Trantham-Davidson H, Neely L, Lavin A, Seamans J (2004) Mechanisms underlying differential D1 versus D2 dopamine receptor regulation of inhibition in prefrontal cortex. J.Neurosci. 24:10652-10659

Tremblay L, Schultz W (1999) Relative reward preference in primate orbitofrontal cortex. Nature 398:704-708

Tsiola A, Hamzei-Sichani F, Peterlin Z, Yuste R (2003) Quantitative morphologic classification of layer 5 neurons from mouse primary visual cortex. The Journal of Comparative Neurology 461:415-428

Uylings HB, van Eden CG (1990) Qualitative and quantitative comparison of the prefrontal cortex in rat and in primates, including humans. Prog. Brain Res 85:31-62

Uylings HBM, Groenewegen HJ, Kolb B (2003) Do rats have a prefrontal cortex? Behavioural Brain Research 146:3-17

vanVreeswijk C, Sompolinsky H (1996) Chaos in neuronal networks with balanced excitatory and inhibitory activity. Science 274:1724-1726

Vempala S, Wang G (2005) On the Benefit of Spectral Projection for Document Clustering In 3rd Workshop on Clustering High Dimensional Data and its Applications Newport Beach, CA.

Verney C, Alvarez C, Geffard M, Berger B (1990) Ultrastructural Double-Labelling Study of Dopamine Terminals and GABA-Containing Neurons in Rat Anteromedial Cerebral Cortex. European Journal of Neuroscience 2:960-972

Vertes RP (2002) Analysis of projections from the medial prefrontal cortex to the thalamus in the rat, with emphasis on nucleus reuniens. The Journal of Comparative Neurology 442:163-187

Vincent S, Khan Y, Benes F (1993) Cellular distribution of dopamine D1 and D2 receptors in rat medial prefrontal cortex. J. Neurosci. 13:2551-2564

Vincent SL, Khan Y, Benes FM (1995) Cellular colocalization of dopamine D1 and D2 receptors in rat medial prefrontal cortex. Synapse 19:112-120

Walker AE (1940) A cytoarchitectural study of the prefrontal area of the macaque monkey. The Journal of Comparative Neurology 73:59-86

Wallén P, Carlsson K, Liljeborg A, Grillner S (1988) Three-dimensional reconstruction of neurons in the lamprey spinal cord in whole-mount, using a confocal laser scanning microscope. J. Neurosci. Methods 24:91-100

Wallis JD (2007) Orbitofrontal Cortex and Its Contribution to Decision-Making. Annu. Rev. Neurosci. 30:31-56

Wang X (1999) Synaptic basis of cortical persistent activity: the importance of NMDA receptors to working memory. J Neurosci. 19:9587-9603

Wang X (1998) Calcium Coding and Adaptive Temporal Computation in Cortical Pyramidal Neurons. J Neurophysiol 79:1549-1566

Wang X, Liu Y, Sanchez-Vives MV, McCormick DA (2003) Adaptation and Temporal Decorrelation by Single Neurons in the Primary Visual Cortex. J Neurophysiol 89:3279-3293

Wang Y, Goldman-Rakic PS (2004) D2 receptor regulation of synaptic burst firing in prefrontal cortical pyramidal neurons. Proceedings of the National Academy of Sciences of the United States of America 101:5093-5098

Wang Y, Markram H, Goodman PH, Berger TK, Ma J, Goldman-Rakic PS (2006)

Heterogeneity in the pyramidal network of the medial prefrontal cortex. Nat Neurosci 9:534-542

Ward J (1963) Hierarchical Grouping to Optimize an Objective Function. Journal of the American Statistical Association 58:244, 236

Watanabe M, Kodama T, Hikosaka K (1997) Increase of extracellular dopamine in primate prefrontal cortex during a working memory task. J.Neurophysiol. 78:2795-2798

Wearne S, Rodriguez A, Ehlenberger D, Rocher A, Henderson S, Hof P (2005) New techniques for imaging, digitization and analysis of three-dimensional neural morphology on multiple scales. Neuroscience 136:661-680

White JA, Sekar NS, Kay AR (1995) Errors in persistent inward currents generated by space-clamp errors: a modeling study. J. Neurophysiol 73:2369-2377

Williams G, Goldman-Rakic P (1995) Modulation of memory fields by dopamine D1 receptors in prefrontal cortex. Nature 376:572-575

Williams SR, Stuart GJ (1999) Mechanisms and consequences of action potential burst firing in rat neocortical pyramidal neurons. J. Physiol. (Lond.) 521 Pt 2:467-482

Williams S, Goldman-Rakic P (1998) Widespread origin of the primate mesofrontal dopamine system. Cereb. Cortex 8:321-345

Williams SR, Stuart GJ (1999) Mechanisms and consequences of action potential burst firing in rat neocortical pyramidal neurons. The Journal of Physiology 521:467-482

Wilt BA, Burns LD, Wei Ho ET, Ghosh KK, Mukamel EA, Schnitzer MJ (2009) Advances in Light Microscopy for Neuroscience. Annu. Rev. Neurosci. 32:435-506

Winocur G (1992) A comparison of normal old rats and young adult rats with lesions to the hippocampus or prefrontal cortex on a test of matching-to-sample. Neuropsychologia 30:769-781

www.olympusfluoview.com Olympus FluoView Resource Center: Theory of Confocal Microscopy. Available at: http://www.olympusfluoview.com/theory/index.html [Accessed January 1, 2010].

Xu J, Kang J (2005) The mechanisms and functions of activity-dependent long-term potentiation of intrinsic excitability. Rev Neurosci 16:311-323

Yamamoto C, McIlwain H (1966) Electrical activities in thin sections from the mammalian brain maintained in chemically-defined media in vitro. Journal of neurochemistry 13:1333

Yang C, Seamans J (1996) Dopamine D1 receptor actions in layers V-VI rat prefrontal cortex neurons in vitro: modulation of dendritic-somatic signal integration. J. Neurosci. 16:1922-1935

Yang C, Seamans J, Gorelova N (1996) Electrophysiological and morphological properties of layers V-VI principal pyramidal cells in rat prefrontal cortex in vitro. J. Neurosci. 16:1904-1921

Yoshimura Y, Dantzker JLM, Callaway EM (2005) Excitatory cortical neurons form fine-scale functional networks. Nature 433:868-873

Young C, Yang C (2004) Dopamine D1/D5 receptor modulates state-dependent switching of soma-dendritic Ca2+ potentials via differential protein kinase A and C activation in rat prefrontal cortical neurons. J.Neurosci. 24:8-23

Zahrt J, Taylor JR, Mathew RG, Arnsten AF (1997) Supranormal stimulation of D1 dopamine receptors in the rodent prefrontal cortex impairs spatial working memory performance. J. Neurosci 17:8528-8535

Zhang W, Linden DJ (2003) The other side of the engram: experience-driven changes in neuronal intrinsic excitability. Nat Rev Neurosci 4:885-900

Zhao Y, Karypis G (2005) Data clustering in life sciences. Molecular Biotechnology 31:55-80

Zheng P, Zhang X, Bunney B, Shi W (1999) Opposite modulation of cortical N-methyl-D-aspartate receptor-mediated responses by low and high concentrations of dopamine. Neuroscience 91:527-535

Zhou F, Hablitz J (1999) Dopamine modulation of membrane and synaptic properties of interneurons in rat cerebral cortex. Journal of Neurophysiology 81:967

Zilles K (1985) The cortex of the rat: a stereotaxic atlas. Springer-Verlag Berlin.